Dielectric Resonator Antennas: From Multifunction Microwave Devices to Optical Nano-antennas

by

Longfang Zou

Bachelor of Engineering,
The University of Electronic Science and Technology of China, China, 1999

Master of Engineering,
Southwest Jiaotong University, China, 2005

Master of Engineering,
The University of Adelaide, Australia, 2008

Thesis submitted for the degree of

Doctor of Philosophy

in

School of Electrical and Electronic Engineering
The University of Adelaide, Australia

March 2013

ADELAIDE
UNIVERSITY
AUSTRALIA

Contents

Abstract

Since a cylindrical dielectric resonator antenna (DRA) was firstly proposed by Long et al. in the 1980s, extensive research has been carried out on analyzing DRA shapes, characterizing the resonant modes, improving their radiation characteristics with various excitation schemes. Compared with conventional conductor-based antennas, DRAs have attractive features such as small size, high radiation efficiency and versatility in their shape and feeding mechanism.

Importantly, various orthogonal modes with diverse radiation characteristics can be excited within a single DRA element. These modes can be utilized for various requirements, which makes the DRA a suitable potential candidate for multifunction applications. Based on this principle, this thesis presents different multifunction designs: Firstly a cross-shaped DRA with separately fed broadside circularly polarized (CP) and omnidirectional linearly polarized (LP) radiation patterns and, secondly, a multifunction annular cylindrical DRA realizing simultaneously omnidirectional horizontally and vertically polarized radiation patterns with low cross-coupling. The evolution, design process and experimental validation of these two antennas are described in details in the thesis.

The second part of the thesis dramatically scales down DRA to shorter wavelengths. Inspired by the fact that DRA still exhibits high radiation efficiency (>90%) in the millimetre wave range, while the efficiency of conventional metallic antenna degrades rapidly with frequencies, this thesis proposes the concept of nanometer-scale DRA operated in their fundamental mode as optical antennas. To validate the concept, optical DRA reflectarrays have been designed and fabricated. Although the zeroth-order spatial harmonic reflection is observed in the measurement due to the imperfect nanofabrication, the power ratio of deflected beam to the specular component of reflection amounts to 4.42, demonstrating the expected operation of the reflectarray. The results strongly support the concept of optical DRA and proposes design methods and strategies for their realization. This proof of concept is an essential step for future research on nano-DRA as building block of emerging nano-structured optical components.

Statement of Originality

This work contains no material that has been accepted for the award of any other degree or diploma in any university or other tertiary institution and, to the best of my knowledge and belief, contains no material previously published or written by another person, except where due reference has been made in the text.

I give consent to this copy of the thesis, when deposited in the University Library, being available for loan, photocopying, and dissemination through the library digital thesis collection, subject to the provisions of the Copyright Act 1968.

I also give permission for the digital version of my thesis to be made available on the web, via the University's digital research repository, the Library catalogue, the Australasian Digital Thesis Program (ADTP) and also through web search engines, unless permission has been granted by the University to restrict access for a period of time.

Signed

Date

Acknowledgments

I would like to express my special appreciation and thanks to my principle supervisor, Prof. Christophe Fumeaux, who has been a tremendous mentor for me. I would like to thank him for his thoughtful guidance, constructive suggestions and prompt responses. His advice on both research as well as on my career have been invaluable. I am indebted to my co-supervisor, Dr Withawat Withayachumnankul for his inspiring guidance in the field of metamaterial and nanoantenna and for generously sharing his knowledge and experience. I also wish to express my appreciation to co-supervisor, Prof. Derek Abbott, for his valuable suggestions and constructive advice. My sincere thanks goes to Associate Prof Cheng-Chew Lim for his long term help, encouragement and advice. His professionalism and kindness have been always appreciated.

This thesis would not have been possible without the guidance, cooperation, and assistance of several individuals and research groups. A special mention of thanks to Dr Thomas Kaufmann, Dr Zhonghao Hu, Mr Ali H. Karami, Mr Shifu Zhao, Mr Weixun Wu, Ms Tiaoming Niu, Mr Benjamin S.-Y. Ung, Dr Hungyen Lin and Mr Henry Ho for their fruitful discussions, assistance and critical comments to my research. I am grateful to Mr Pavel Simcik, Mr Brandon Pullen and Mr Ian Linke who fabricated my microwave antenna designs. I express my heart-felt gratitude to Mr Charan Manish Shah, Dr Madhu Bhaskaran, Dr Sharath Sriram, and Prof Arnan Mitchell from the Functional Materials and Microsystems Research Group, RMIT University for fabricating optical dielectric resonator nano-antenna reflectarray and expanding my knowledge of nanofabrication. Their scientific inputs, personal help and friendly nature have made the cooperation more effective.

I must thank the office & support staff of the School of Electrical and Electronic Engineering, Mr Stephen Guest, Mrs Ivana Rebellato, Ms Rose-Marie Descalzi, Ms Deborah Koch, Ms Jodie Schluter, Mr Danny Di Giacomo, Mr David Bowler, Mr Mark Innes, Mr Ryan King and Mr Anthony Schueller, for their kind support throughout my PhD. They always ready to give their timely help whenever required.

Last but not least, I owe my deepest gratitude to my parents and parents-in-law, for educating me with aspects from arts, engineering and technology, and for unconditional support and encouragement to pursue my interests. I also thank my sisters for giving

me moral encouragement all the time. Words are not enough to praise my wife Fang Duan, whose love, support, encouragement and inspiration have guided me through the most challenging times. I must mention my daughter Emily Zou for refreshing my days with her beautiful smile, which has made this long journey possible, endurable, and enjoyable.

Conventions

Typesetting

This thesis is typeset using the LaTeX2e software. WinEdt build 5.5 was used as an effective interface to LaTeX.

Referencing

Referencing and citation style in this thesis are based on the Institute of Electrical and Electronics Engineers (IEEE) Transaction style.

Units

The units used in this thesis are based on the International System of Units (SI units).

Prefixes

In this thesis, the commonly used numerical prefixes to the SI units are ”p” (pico, 10^{-12}), ”n” (nano, 10^{-9}), ”μ” (micro, 10^{-6}), ”m”,(milli,10^{-3}), ”k”(kilo, 10^{3}), ”M”(mega, 10^{6}), ”G”(giga, 10^{9}), and ”T”(tera, 10^{12}).

Spelling

The Australian English spelling is adopted in this thesis.

Abbreviations

AR	Axial Ratio
BAN	Body-Area Network
CP	Circularly Polarized
CPW	Coplanar Waveguide
DR	Dielectric Resonator
DRA	Dielectric Resonator Antenna
DWM	Dielectric Waveguide Model
EBG	Electromagnetic Band Gap
ECC	Envelope Correlation Coefficient
EM	Electromagnetic
FEM	Finite-Element Method
HD	High Definition
HEM	Hybrid Electric and Magnetic
HFSS	High Frequency Structural Simulator (a commercial simulation software)
HMSIW	Half-mode Substrate Integrated Waveguide
HP	Horizontally Polarized
LHCP	Left-Hand Circularly Polarized
LP	Linearly Polarized
MEG	Mean Effective Gain
MIMO	Multiple-Input Multiple-Output
MMW	Millimeter Wave

MNG-TL	Mu-Negative Transmission Line
PCB	Printed Circuit Board
PEC	Perfect Electric Conductor
PIFA	Planar Inverted-F Antenna
RHCP	Right-Hand Circularly Polarized
SIW	Substrate Integrated Waveguide
SPP	Surface Plasmon Polariton
TE	Transverse Electric
TM	Transverse Magnetic
VP	Vertically Polarized
WPAN	Wireless Personal Area Network
XPR	Cross-polarization Power Ratio

Author Publications

Journal

[1] L. Zou and C. Fumeaux, "A cross-shaped dielectric resonator antenna for multi-function and polarization diversity applications," *IEEE Antennas Wireless Propag. Lett.*, vol. 10, pp. 742-745, Jul. 2011.

[2] L. Zou, D. Abbott, and C. Fumeaux, "Omnidirectional cylindrical dielectric resonator antenna with dual polarization," *IEEE Antennas Wireless Propag. Lett.*, vol. 11, pp. 515-518, 2012.

[3] L. Zou, W. Withayachumnankul, C. Shah, A. Mitchell, M. Bhaskaran, S. Sriram, and C. Fumeaux, "Dielectric resonator nanoantennas at visible frequencies," *Opt. Express*, vol. 21, no. 1, pp. 1344-1352, Jan. 2013.

Conference

[1] L. Zou and C. Fumeaux, "High-permittivity cross-shaped dielectric resonator antenna for circular polarization," in *Int. Conf. Electromagn. Adv. App (ICEAA).*, Sep. 2010, pp. 1-4.

[2] L. Zou and C. Fumeaux, "Cross-shaped dielectric resonator antenna for circular polarization with symmetric radiation patterns," in *Twelfth Australian Symposium on Antennas*, Feb. 2011.

[3] L. Zou and C. Fumeaux, "Horizontally polarized omnidirectional dielectric resonator antenna," in *Asia-Pacific Microwave Conference (APMC), 2011*, Dec. 2011, pp. 849-852.

[4] L. Zou and C. Fumeaux, "Mutual coupling reduction in a multi-mode multi-function dielectric resonator antenna," in *International Symposium on Antennas and Propagation (APS)*, Jul. 2012. pp. 1-2.

[5] L. Zou, W. Withayachumnankul, C. Shah, A. Mitchell, M. Bhaskaran, S. Sriram, and C. Fumeaux, "Optical reflectarray based on dielectric resonator antennas," in *Australian Nanotechnology Network (ANN) 2012 Early Career Symposium*, Dec. 2012.

[6] L. Zou, W. Withayachumnankul, C. Shah, A. Mitchell, M. Bhaskaran, S. Sriram, and C. Fumeaux, "Optical dielectric resonator antenna reflectarray," in *Thirteenth Australian Symposium on Antennas*, Feb. 2013.

List of Figures

List of Tables

Chapter 1

Introduction

THIS chapter gives a brief introduction on dielectric resonator antennas (DRAs) and highlights their attractive features. The motivation of the research is presented, followed by objectives of the thesis. The original contributions are also presented. The structure of the thesis is sketched in a diagram and the content of each chapter is overviewed at the end of this chapter.

1.1 Introduction and motivation

In 1939, Richtmyer first demonstrated that dielectric objects can resonate in various modes [1]. He appropriately named these structures dielectric resonators (DRs) since they can act similarly as metallic cavity resonators. At the early stage, research on DR was influenced by the hypothesis that DRs were strictly energy storage devices. The theoretical studies of DRs [2–4] in the 1960s led to impressive progress in a multitude of applications including oscillators, amplifiers and filters. Compared to other types of resonators, DRs offer advantages of compact size, lower cost, lower weight, material availability, and ease of manufacturing.

Richtmyer also mentioned that if a DR is placed in free space, it must radiate due to the boundary conditions at the interface between dielectric and air [1]. This provided the fundamental theory of the later invented dielectric resonator antenna (DRA). Long et al. firstly proposed the concept of using DR as a radiator in 1983 [5]. In that seminal paper, a cylindrical DR was demonstrated to provide efficient radiation in the direction normal to its ground plane. Since then, extensive research has been carried out on analyzing DRA shapes, resonant modes, radiation characteristics and excitation schemes [6,7]. The results of these investigations have highlighted the attractive features of DRAs:

- The DRA size is proportional to $\lambda_0/\sqrt{\varepsilon_r}$, with λ_0 and ε_r being the free-space wavelength and relative dielectric permittivity, respectively. Compared with the conventional counterparts such as microstrip antennas, DRAs provide therefore a natural reduction in size. Furthermore, ε_r can be selected from 4 to 100, allowing the flexibility in controlling antenna size and bandwidth.

- The shape of a DRA can be tailored to fit specific requirements. For example, a trapezoidal DRA has been demonstrated with an impedance bandwidth of 55% and broadside radiation patterns with low cross-polarization [8].

- Apart from serving as an antenna, a DRA can also serve as other functions, such as packing cover and decoration. A rectangular hollow DR was designed as an antenna and a package cover [9]; a glass swan and an apple, both made of K-glass, act as both antennas and artworks [10].

- DRAs can be excited by most of the feeding schemes, such as probes, microstrip, slots, waveguides, substrate integrated waveguide (SIW), and half-mode substrate integrated waveguide (HMSIW).

- The 3-D structure of the DRA offers an additional freedom in exciting various modes in one antenna volume. Each mode can be employed for a different application, which makes the DRA a successful candidate for multifunction, diversity, and multiple-input multiple-output (MIMO) communication systems. Furthermore, the orthogonal field distribution of DR modes can be exploited to achieve a low inter-mode coupling design.

- DRAs have the capacity of providing efficient radiation in the millimeter wave (MMW) frequency region due to the absence of the inherent conductor losses. This has been proved experimentally through comparison of a DRA with a conventional microstrip antenna at 35 GHz [11]: The DRA exhibits a high radiation efficiency (>90%) with negligible dissipation loss, whilst the performance of conventional metallic antennas rapidly degrades with a radiation efficiency of around 80%.

1.1.1 Motivation - Multifunction and diversity DRA

Mobile wireless communication devices are becoming smaller and increasingly multifunctional. Considering space limitation, port-to-port isolation or mutual effects of other elements, the conventional solution of using two or more antennas to realize multifunction or diversity schemes might be not feasible. One of the alternative solutions is using a single antenna structure with several functions with low mutual power coupling between different ports, for example multi-ports printed diversity antenna [12,13] or planar inverted-F antenna (PIFA) [14,15]. These antennas have advantages of compact size, low fabrication cost and low profile, but they usually suffer from their complicated structure, narrow bandwidth or relatively low gain.

Since the 3-D structure of DRAs allows exciting various modes in one antenna volume, it is feasible to design multifunction or diversity DRA using a single DR, which will reduce overall system size and cost. The desired requirements can be achieved by properly choosing the shape and modes of the DR. Several high performance multifunction DRAs have been studied and reported in the last decade. A cylindrical DR was used as

filter and antenna [16]; ultrawideband operation was achieved by exciting the fundamental and higher-order modes in a hybrid DRA [17]; a cylindrical DRA was utilized as direction finder [18]; a dual-band antenna with two different radiation patterns in two separate bands was achieved by using a cylindrical DR [19]. In these multifunction DRAs, the various modes are resonant at different frequencies. It appears however attractive to tailor the resonance frequencies of modes to achieve overlapping frequency ranges for the different ports, and thus realize a diversity DRA.

1.1.2 Motivation - Optical DRA

The current research on DRAs mainly focuses on microwave and MMW range. As an alternative choice of conventional metallic antennas, DRAs exhibit high radiation efficiency while the efficiency of metallic antennas significantly decrease with the increase of the frequency in MMW range. Inspired by this fact, another aim of this thesis is to extend the concept of DRA from radio-frequencies towards realization of optical antennas in the infrared and visible part of spectrum. Most current realisations of optical antennas are based on resonant metallic nanostructures. The radiation efficiency of metallic optical antennas is adversely affected by the instrinsic loss in Drude metals at optical frequencies. Considering that low-loss high-permittivity dielectric materials are available at optical frequencies, it is feasible to extend the use of DRAs to optical frequencies, as a pathway towards increasing the efficiency of resonant optical antennas.

1.2 Objectives of the thesis

In first part of this thesis, the focus is on the investigation of exciting multi-modes in a single DR to realize multifunction and diversity DRAs. In order to comprehend the field distribution and the radiation characteristics of resonant modes, the thesis starts with the analytical and numerical examination of the two canonical DR shapes, rectangle and cylinder. The description of the resonant frequency, Q-factor and field distribution of fundamental modes in DRs and corresponding excitation methods provide a in-depth understanding of the radiation properties of the canonical DRAs, which will help to develop non-canonical shaped devices with enhanced performance in terms of bandwidth, gain and polarization. Most importantly, this discussion provides the basis for the multifunction and diversity DRA design principle, by demonstrating how to

control resonance frequencies of various modes by properly choosing the DR geometry and feeding method.

The design processes for two multifunction and diversity DRAs are then explained in detail with the goal of allowing the reader to understand how to excite various modes, adjust resonance frequencies, integrate multi-function into one antenna volume, reduce mutual coupling between the mode and increase bandwidth. In this way, the design principles and performance enhancement strategies can easily be adapted and implemented to similar applications at other specified frequencies.

The second part of this thesis extends the concept of DRAs from microwave towards the infrared and visible part of spectrum. The geometry of DRAs can be scaled with respect to the wavelength for operation at microwave frequencies by assuming that metal is a nearly perfect electric conductor (PEC). However, the penetration of electromagnetic (EM) fields into the metal ground plane can no longer be neglected and collective electron resonances must be considered as the operation frequency approaches infrared and visible frequencies. Thus, the study of the metal properties across the EM spectrum is a fundamental investigation for bringing the concept of DRA toward the visible range.

Towards understanding the scaling behavior of DRAs, and using a scalable DRA geometry, two well-known metal models, the surface impedance model and Drude model, are numerically evaluated in terms of accuracy and computational cost. The simulated field distributions of the scalable DRA model confirms the feasibility of exciting the fundamental DR mode at optical frequencies. Results from this fundamental research pave the way for extending the DRA concept from microwave to optical frequencies. The scalable DRA model can be adapted or extended to different DRA geometries or even DRA arrays at different frequencies across the spectrum.

The proposed concept of optical DRA is implemented and experimentally validated for the first time in the literature through a realization of optical nano-DRA reflectarrays. The reflectarray configuration eliminates the need for integrated feeding components and thus is suitable for the studying of fundamental optical DRA properties. The designed reflectarrays exhibit the capacity of deflecting a laser beam to a predefined deflection angle relative to specular reflection. Both simulation and measurement results indicate that less than 20% of the power loss can be attributed to the dissipation in the DRs. These results strongly support the concept of optical DRA with enhanced radiation efficiency. The proposed optical design, choice of materials, nanofabrication

techniques and measurement process are of great importance and of strategic relevance for the future of optical DRA research.

1.3 Statement of original contributions

This thesis involves several original contributions in the two fields of exciting multi-modes in a single DR volume and extending DRA research from microwave and MMW frequencies to visible spectrum, as declared in this section.

- A circularly polarized (CP) DRA with a wideband of 13% is achieved using a cross-shaped DR composed of high-dielectric thin plates. The CP operation is realized by exciting two orthogonal fundamental TE_{111} modes in the two cross arms with 90° phase difference. The size and dielectric volume of the antenna is reduced by using thin plates of high permittivity material to build the DR. The proposed design was presented at the *International Conference on Electromagnetics in Advanced Applications (ICEAA), 2010* and the main results are published in the proceedings under the title "High-permittivity cross-shaped dielectric resonator antenna for circular polarization" [20].

- An evolution of the design introduced a physical separation between the exciting microstrip lines and the feeding network, to reduce the impact of the asymmetric feed on the radiation pattern. The evolutional design was presented at the *Twelfth Australian Symposium on Antennas, 2011* under the title "Cross-shaped dielectric resonator antenna for circular polarization with symmetric radiation patterns" [21]. The physical separation is widely employed in this thesis to design high performance DRA.

- The concept of exciting multi-modes in a single DR is demonstrated by a cross-shaped multifunction and diversity DRA with separately fed broadside CP and omnidirectional linearly polarized (LP) radiation patterns. These distinct radiation patterns are achieved in overlapping frequency bands by exciting the TE_{111} and Quasi-TM_{111} modes in a single DR volume. The experimental results show a good agreement with simulation and demonstrate a broadside CP operation over a bandwidth of 6.8%, which overlaps with the omnidirectional LP impedance bandwidth of 38.5%. The proposed antenna could be used not only as multifunction but also as polarization diversity antenna due to the overlapping dual-feed

CP and LP operation. The multifunction and diversity DRA is published in *IEEE Antennas Wireless Propagation Letter* under the title "A cross-shaped dielectric resonator antenna for multifunction and polarization diversity applications" [22].

- The effect of the feeding geometry on the mutual coupling between the modes is further investigated. It is observed that an asymmetric feeding degrades the orthogonality of the modes and thus increases the inter-port coupling coefficient. The asymmetric field distribution can be corrected by using either an asymmetric DR structure or a symmetrized feeding method. Using either of these two methods, the simulated coupling coefficient is reduced to less than -15 dB. The results were presented at the *International Symposium on Antennas and Propagation (APS), 2012* and is published in the proceedings under the title "Mutual coupling reduction in a multi-mode multi-function dielectric resonator antenna" [23].

- The concept of using the $TE_{01\delta}$ mode as a radiating mode in a cylindrical DR is experimentally validated. The mode is traditionally exploited in filtering applications because of its intrinsically high Q-factor. Therefore, an air gap is introduced in the design and a dual point feeding network is optimized to achieve a wider impedance bandwidth with radially symmetric radiation patterns. The experimental results demonstrate omnidirectional operation with horizontal polarization over a bandwidth of 5.6% around the centre frequency of 3.9 GHz. The proposed design was presented at the *Asia-Pacific Microwave Conference (APMC), 2011* and is published in the proceedings under the title "Horizontally polarized omnidirectional dielectric resonator antenna" [24].

- A dual-mode DRA with a magnetic-dipole-like and electric-monopole-like radiation patterns is designed simultaneously by exciting the $TE_{01\delta}$ and $TM_{01\delta}$ modes in a single annular cylindrical DR. The impedance bandwidth of the $TE_{01\delta}$ is further increased to 7.4% by using four sets of double microstrip feeding arcs, which are also demonstrated to suppress the influence of higher-order modes. The overlapping operating band for the two functions makes the proposed antenna suitable for being used in diversity or MIMO communication systems, when omnidirectional characteristics are required. The proposed antenna has the advantage of combining compact size and wide bandwidth. The dual polarized DRA is published in *IEEE Antennas Wireless Propagation Letter* under the title "Omnidirectional cylindrical dielectric resonator antenna with dual polarization" [25].

- The DRAs exhibit high radiation efficiency in the millimeter wave frequency range due to the absence of intrinsic conductor loss of DRs. Based on this fact, the optical DRA concept is proposed as a prominent extension to the current DRA research. One of the critical issues is that the properties of a metallic ground plane are largely different from a perfect electric conductor (PEC) at optical frequencies. As a result, the antenna scaling property is not valid and the classical skin-effect model becomes unsuitable towards the optical frequencies. Through a scaling behavior study of DRAs at frequency ranges from microwave to visible spectrum, it has been shown that the surface impedance model has acceptable accuracy with low computational costs below the near-infrared spectrum. In contrast, the Drude model provides a more accurate description of the field penetration and dispersive properties of metal at optical frequencies. However, the large negative permittivity of silver described by Drude model leads to a fine mesh requirement and hence increases the computational cost in mesh-based EM simulations. This limits the Drude model application to near-infrared and visible frequencies. The transition and overlap of these two models validate this practical method of characterizing metal properties from microwave to optical frequencies. These findings are in preparation for submission to the *IEEE Antennas Wireless Propagation Letter*.

- Considering the lack of true nanoscale light source and effective optical waveguide, the concept of optical DRA is indirectly validated by a reflectarray structure. The reflectarray configuration eliminates the need for integrated feeding components and thus is suitable for studying the fundamental optical DRA properties. The proposed optical DRA reflectarray provides a platform for indirectly evaluating the function of optical DRs through observation of a predefined far-field beam angular deflection. The deflection angle for the reflected beam is manipulated by using a periodic arrangement of cylindrical DRs sub-arrays, with various diameters appropriately selected around the dimension of the resonant fundamental $HEM_{11\delta}$ mode. Although the zeroth-order spatial harmonic specular reflection is observed in the measurement due to the fabrication imperfection, the power ratio of the deflected beam to the spatial reflection amounts to 4.42, demonstrating the expected operation of the reflectarray. The measured deflected beam angle is in nearly perfect agreement with the prediction from simulation and array theory calculation. A uniform DRA array has been fabricated as a platform to study the

efficiency of DRAs at optical frequencies. Both the simulation and measurement results indicate that less than 20% of the power loss can be attributed to the dissipation in the DRs. These results strongly support the concept of optical DRA, as emerging opportunity for realising nanophotonic applications. The optical DRA reflectarray is published in *Optical Express* under the title "Dielectric resonator nanoantennas at visible frequencies" [26]. The paper has attracted considerable attention and is one of the top download papers in Jan. 2013. The research of optical DRA reflectarray is also presented at the *Australian Nanotechnology Network (ANN) 2012 Early Career Symposium* [27] and *Thirteenth Australian Symposium on Antennas, 2013* [28].

- Since the DRs are sub-wavelength in nature, one might think that the observed deflection could be attributed to an equivalent averaged refractive index of the dielectric structures. To demonstrate that this is not the case, an equivalent refractive index reflector is simulated to verify the necessity of a resonance mechanism to explain the observed beam shaping. The simulated scattered field of a grating reflector designed with the same dielectric volume does not exhibit the same capacity of beam shaping due to the lack of resonance mechanism. The comparison between DRA reflectarray and dielectric grating reflector further confirms the resonant behavior of nanometer-scale cylindrical resonators. The comparison result has been submitted to the *International Symposium on Antennas and Propagation (APS), 2013* and is currently under review.

1.4 Overview of the thesis

The next eight chapters of this thesis are outlined as described below, and a tree diagram of the thesis structure is also provided in Fig. 1.1.

Chapter 2 reviews the characteristics of two canonical DRA geometries, the cylindrical and rectangular DRA, as the geometries of the antennas proposed in this thesis are based on these two canonical shapes. In each geometry, the near fields and the radiation characteristics of the fundamental modes are described. The closed-form expressions for the resonance frequencies and Q-factors of each fundamental mode are explicitly given. Subsequently, the corresponding feeding methods of each mode are also discussed. Selected examples, taken from the literature, are utilized to illustrate strategies of how to enhance antenna performance.

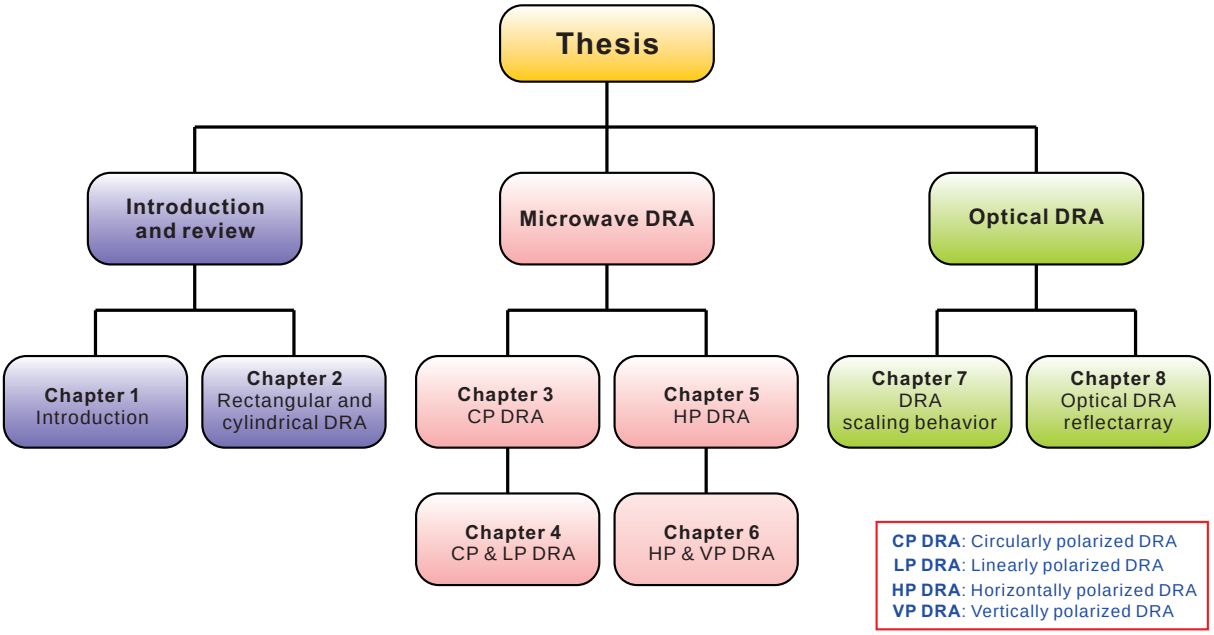

Figure 1.1. The tree diagram of the thesis.

Chapter 3 proposes a wideband cross-shaped CP DRA. In order to obtain a compact design, the DR is composed of two same size notched rectangular thin slices with a high-permittivity of $\varepsilon_r = 50$. As first step, the effective permittivity of the thin high-permittivity DRA has been numerically investigated. Regarding the feeding of the two crossed arms of the DR, the TE_{111} modes are excited by two orthogonal microstrip lines with 90° phase difference to generate circular polarization. The combination of high-permittivity material for the DRA and of a quadrature feed results in a compact design with a wide CP bandwidth. This chapter also shows a method of reducing the impact of the feeding network on the radiation pattern. The simple antenna configuration and feeding mechanism make this design easily scalable to other frequency bands or extendable to have multifunction designs.

Chapter 4 extends the CP DRA to a multifunction and diversity DRA. The proposed design features separately fed broadside CP and omnidirectional LP radiation patterns. The CP and LP radiation patterns are achieved by exciting the TE_{111} and Quasi-TM_{111} mode, respectively. The chapter also shows a method to adjust resonant frequency and enlarge bandwidth by optimizing the feeding network. Additionally to that, methods of reducing mutual coupling between modes are investigated. Antenna diversity performance is examined in terms of envelope correlation coefficient (ECC) and mean effective gain (MEG). The calculation method of ECC and MEG are also presented in this chapter.

In Chapter 5, inspired by the fact that the magnetic field distribution of the $TE_{01\delta}$ mode of a cylindrical DR is equivalent to a magnetic dipole located at the centre of cylinder, we propose to use the $TE_{01\delta}$ mode to radiate horizontally polarized (HP) omnidirectional patterns. However, the main disadvantage of this resonant mode, is its high Q-factor that results in a narrow bandwidth. Two techniques have been proposed to enhance this bandwidth. Firstly, an air gap is introduced between the cylindrical DR and the ground plane. Secondly, a balanced coupling method is realized, by placing two arc-shaped microstrip lines on each side of the DR. An impedance bandwidth of 5.6% has been demonstrated in both simulation and measurement by optimizing the air gap and arc-shaped microstrip lines.

Chapter 6 presents a diversity annular cylindrical DRA realizing simultaneously omnidirectional HP and vertically polarized (VP) radiation patterns with low cross-coupling. The HP radiation pattern is achieved based on the design principle introduced in Chapter 5. In order to further increase the bandwidth of the $TE_{01\delta}$ mode, two groups of four radially arranged microstrip feeding lines with two different lengths are utilized. On the other hand, the VP radiation pattern is obtained by exciting the $TM_{01\delta}$ mode in the same cylindrical DR. To achieve multifunction and diversity operation, the impedance bandwidth of the $TM_{01\delta}$ mode is increased to overlap with the operating band of the $TE_{01\delta}$ mode. Both simulated and measured results demonstrate good diversity antenna performance.

Chapter 7 proposes the optical DRA concept as an important extension to the current DRA research. The idea is inspired by the fact that DRAs demonstrate high radiation efficiency at MMW frequency due to the absence of intrinsic conductor loss, while the efficiency of conventional resonant metallic antennas decreases significantly with increasing frequency in this spectral range. A scalable DRA model is utilized to study the fundamental scaling behavior of DRA in frequency ranges from microwaves to the visible spectrum. The scaling behavior investigation is facilitated by a practical method of combining the modified relaxation-effect model and Drude model to characterize metal property from microwave to optical frequencies. The simulated field distributions confirm the excitation of the fundamental mode in nano-DRAs at optical frequencies.

In Chapter 8, a fabricated optical nano-DRA reflectarray provides a platform for indirectly evaluating the function of optical DRAs through observation of a predefined

far-field beam angular deflection. The angular deflection for the reflected beam is manipulated by using a periodic arrangement of cylindrical DRs sub-arrays, with varying diameters appropriately selected around the dimension of the resonant fundamental $HEM_{11\delta}$ mode. The resonance mechanism of the DRA in the reflectarray is confirmed through a comparison with a corresponding non-resonant dielectric grating. Furthermore, the simulation and measurement results of a uniform array reveal that only 20% of the lost power can be attributed to dissipation in the DRs. The results strongly support the concept of optical DRA as alternative to resonant plasmonic optical nano-antennas. The detailed design, nanofabrication and measurement process are presented in this chapter.

Chapter 9 summarizes the results of this thesis and recommends possible directions for future work.

Chapter 2

Rectangular and cylindrical dielectric resonator antenna

IN the last three decades, various dielectric resonator antenna (DRA) geometries have been proposed to satisfy the diverse performance requirements. Generally, these advanced geometries are evolutionary from canonical DRA geometries, including hemisphere, rectangle and cylinder. Thus, the analytical and numerical examination of these three canonical dielectric resonators (DRs) is essential to provide an insight on the properties of modes, resonant frequency and Q-factor. This chapter reviews resonant frequency, Q-factor and field distribution for the fundamental modes of rectangular and cylindrical DRs since the geometries of the proposed DRAs in this thesis are based on these two geometries. The typical feeding mechanisms of each modes are illustrated with corresponding field distribution in the DRs. This chapter provides the fundamentals of this thesis and is required for better understanding of the following chapters.

2.1 Introduction

One of the attractive features of dielectric resonator antennas (DRAs) is that dielectric resonator (DR) shapes can be tailored to fit specific requirements. Based on three canonical geometries, hemisphere, cylinder and rectangle, a great variety of derived geometries have been proposed towards satisfying specifications such as required resonance frequencies, radiation characteristics and desired impedance bandwidth. For example, a two-element half-hemispherical DRA configuration was employed to design a broadband monopole-type radiator [29]; a cross-shaped DRA was utilized to generate circular polarized radiation patterns [30]; an inverted trapezoidal DRA exhibited a wide impedance bandwidth of 55% ($|S_{11}|$ < -10 dB) by combining the resonances of the first two lower-order modes [8]; an ultra wideband DRA was achieved by using a annual DR combined with a quarter-wave monopole [31]; an inverted truncated annular conical DRA was designed for potential use in body-area network (BAN) applications [32]. It is important to fully understand the fundamental DRA modes in canonical geometries before considering how these derived geometries can contribute to better antenna performance. Therefore, this chapter will focus on the canonical geometries.

Although the resonant frequency, radiation Q-factor and radiation patterns of the hemispherical DRA can be predicted from exact analytical solutions, the practical applications of hemispherical DRAs have been so far limited due to difficulties in fabrication and limited number of degrees of freedom in choosing the design parameters. For a given material, both the resonator frequency and radiation Q-factor are determined by the hemisphere radius [33]. Design flexibility can be gained by using a nonhomogeneous hemispherical DR. For example, in [34], a hollow hemispherical DRA with relative permittivity of 8.9 exhibits a wider bandwidth of 24% compared to the corresponding solid hemispherical DRA bandwidth of 13%. The two-layer hemispherical DRA excited by an annular slot has been theoretically and experimentally in [33]. A hollow hemispherical DR, made of transparent glass with relative permittivity of 6.85, acts as both antenna and light cover with LEDs integrated in the central hollow region [35]. The experiment demonstrated that the number of LEDs and the LEDs' ON/OFF status do not affect the DRA performance. In the same paper, a dual-band hollow hemispherical DRA is also realized by exciting the fundamental TE_{111} and higher-order TE_{112} modes.

In contrast, in addition of their simple fabrication, rectangular and cylindrical DRAs offer three and two degrees of freedom, respectively. Desired radiation Q-factors can be obtained by varying the DRA's dimensions, which provides the designer with more options for particular applications [36]. The geometries of the antennas proposed in this thesis are based on rectangle and cylinder shapes and thus the analysis of hemispherical DRA will be omitted.

DRAs can be excited by different feeding mechanisms. The excitation method and location of the feeding point can affect significantly the DRA performance in terms of resonant frequency, impedance bandwidth, radiation efficiency, radiation patterns, gain and polarization. To achieve the maximum coupling, the point where the excitation electric currents are applied should be located in an area of strong fields with appropriate orientation. It is therefore necessary to understand the field distribution inside the DR and determine the most advantageous location of the feeding point to excite a desired mode. In this chapter, the field distribution, resonant frequency and radiation Q-factor of fundamental modes are firstly reviewed, followed by the description of corresponding feeding mechanisms.

2.2 Modes of DR

The electric and magnetic wall boundary conditions are usually employed in analyzing an isolated DR. An electric wall is a surface on which the tangential electric field $\vec{E}$ must be zero [37], i.e.,

$$\hat{n} \times \vec{E} = 0 \,, \tag{2.1}$$

where $\hat{n}$ denotes the vector normal to the surfaces of the resonator. At microwave frequencies, good conductors such as copper, provide a surface with a very small skin depth (the depth to which most of the microwave power penetrates). The boundary of these good conductors can be then approximately regarded as electric wall. In addition to the electric wall boundary condition of Eq. (2.1), Maxwell equations show that the normal component of $\vec{H}$ is zero on an electric wall, i.e.

$$\hat{n} \cdot \vec{H} = 0 \,. \tag{2.2}$$

The dual relationship for the magnetic field $\vec{H}$ at a magnetic wall satisfy the condition of

$$\hat{n} \times \vec{H} = 0 \,. \tag{2.3}$$

The tangential magnetic field vanishes along a magnetic wall. The dual boundary condition

$$\hat{n} \cdot \vec{E} = 0 \tag{2.4}$$

holds on a magnetic wall [37]. Although magnetic wall boundary does not really exist in practice, it is a useful and convenient theoretical concept. For example, it is feasible to simulate only one half of a geometry by placing magnetic wall at the appropriate symmetry plane.

Van Bladel [3, 4] has broadly categorized modes of an arbitrarily shaped DR of very high permittivity into confined and nonconfined type. The confined modes of DR approximately satisfy magnetic wall boundary conditions (Eq. (2.3) and (2.4)) and they can only be supported by dielectric bodies of revolution such as spherical and cylindrical DR [3]. For example, the $TM_{01\delta}$ mode of a cylindrical DR is a confined mode. Compared to confined modes, nonconfined modes only satisfy the second magnetic wall boundary condition (Eq. (2.4)) and they are supported by any arbitrary DR shapes. The lowest order nonconfined and confined modes radiate like magnetic and electric dipoles, respectively.

2.3 Rectangular dielectric resonator antenna

Besides the advantage of having more design freedom than hemispherical and cylindrical DRAs, rectangular DRAs exhibit mode degeneracy, which can be controlled and mitigated by properly selecting the dimensions of the resonators. In contrast, mode degeneracy always exists in hemispherical and cylindrical DRAs due to the existence of certain symmetries [38]. Although mode degeneracy may be necessary for dual or circular polarizations designs, it generally results in increased cross polarization in linear polarization designs, which can cause a decrease in the co-polarized gain.

A rectangular DR supports only nonconfined modes since it is not a body of revolution. According to electromagnetic fields theory, the modes of a rectangular DR can be of the TE, TM or hybrid type. However, existence of the lower-order TM modes, predicted by Okaya and Barash's theory [2], has not been experimentally observed. Therefore, only the fundamental TE modes of a rectangular DR will be discussed.

2.3.1 Resonant frequency of the fundamental TE_{111} mode

A rectangular DR is characterized by dielectric permittivity ε_r, height H, width W and length L, as shown in Fig. 2.1. The DR is placed on a ground plane, which is nearly equivalent to an electric symmetry plane. According to the image theory [39], the ground plane is removed by a virtual image source on the other side of the ground plane in the analysis. Thus, the DR height of $b/2$ is utilized in the model.

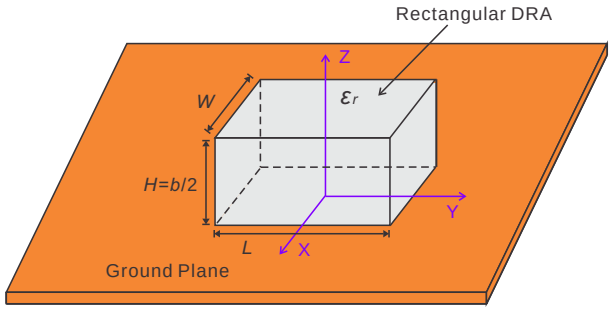

Figure 2.1. Geometry of rectangular DR on a ground plane.

Referring to the rectangular DR and coordinate system shown in Fig. 2.1, the fundamental TE modes are TE^x_{111}, TE^y_{111} and TE^z_{111}, which would radiate like short magnetic dipoles in the X, Y and Z axis directions of the Cartesian coordinate system, respectively. The analysis of these modes is similar and hence TE^x_{111} is discussed only.

The electric vector potential of a TE^x_{111} is given by the equation [40]

$$\vec{F} = \psi \, \hat{e}_x \, , \tag{2.5}$$

where the scalar wave function ψ is given by

$$\psi = C \, \cos(k_x x) \, \cos(k_y y) \, \cos(k_z z) \, , \tag{2.6}$$

when the origin of the coordinate system is located in the centre of the DR, on the ground plane. It is noted that the cosine functions evidence that these modes are symmetric around X, Y and Z axis directions. Then, the field components inside the resonator can be derived from Eq. (2.6) as [41],

$$E_x = 0 \tag{2.7}$$

$$E_y = A \, k_z \, \cos(k_x x) \, \cos(k_y y) \, \sin(k_z z) \tag{2.8}$$

$$E_z = -A \, k_y \, \cos(k_x x) \, \sin(k_y y) \, \cos(k_z z) \tag{2.9}$$

$$H_x = A \, \frac{k_y^2 + k_z^2}{j\omega\mu} \, \cos(k_x x) \, \cos(k_y y) \, \cos(k_z z) \tag{2.10}$$

$$H_y = A \, \frac{k_x k_y}{j\omega\mu} \, \sin(k_x x) \, \sin(k_y y) \, \cos(k_z z) \tag{2.11}$$

$$H_z = A \, \frac{k_x k_z}{j\omega\mu} \, \sin(k_x x) \, \cos(k_y y) \, \sin(k_z z) \tag{2.12}$$

where A is an arbitrary constant, k_x, k_y and k_z are the wavenumbers along the x, y and z directions, respectively, ω is the angular frequency and μ is the permeability. Enforcing the magnetic wall boundary condition Eq. (2.4) at the surfaces of the resonator $y = \pm L/2$ and $z = \pm b/2$, the wavenumbers k_y and k_z are obtained

$$k_y = m \, \pi / L \, , \tag{2.13}$$

$$k_z = n \, \pi / b \, , \tag{2.14}$$

where m, n are positive integers.

The wavenumber k_x is given by using Marcatili's approximation [42], as explained in the following. Assuming

1. the tangential components of the field at $x = \pm W/2$ are matched with an external field;

2. the external field decays exponentially as it propagates normally from these surfaces,

the E and H field of the external field are give by

$$E_y = B \, k_{z0} \, \cos(k_{y0} y) \, \sin(k_{z0} z) \, e^{-\beta x} \tag{2.15}$$

$$E_z = -B \, k_{y0} \, \sin(k_{y0} y) \, \cos(k_{z0} z) \, e^{-\beta x} \tag{2.16}$$

$$H_y = B \, \frac{k_{y0}\beta}{j\omega\mu} \, \sin(k_{y0} y) \, \cos(k_{z0} z) \, e^{-\beta x} \tag{2.17}$$

$$H_z = B \, \frac{k_{z0}\beta}{j\omega\mu} \, \cos(k_{y0} y) \, \sin(k_{z0} z) \, e^{-\beta x} \tag{2.18}$$

where B is a constant and $\beta = \sqrt{(k_{y0}^2 + k_{z0}^2 - k_0^2)}$. The free-space wavenumber $k_0 = 2\pi f_0/c$ corresponds to the resonant frequency f_0 and speed of light in vacuum c. Through a mode matching procedure, the transcendental equation is given by

$$k_x \tan\left(\frac{k_x W}{2}\right) = \sqrt{(\varepsilon_r - 1)k_0^2 - k_x^2}\,, \tag{2.19}$$

where ε_r is the relative dielectric permittivity. Substituting Eq. (2.13), (2.14) and introducing the separation equation

$$k_x^2 + k_y^2 + k_z^2 = \varepsilon_r\, k_0^2\,, \tag{2.20}$$

into Eq. (2.19), the equation can be written as

$$\sqrt{\varepsilon_r\, k_0^2 - \left(\frac{\pi}{L}\right)^2 - \left(\frac{\pi}{b}\right)^2}\, \tan\left(\frac{W}{2}\sqrt{\varepsilon_r\, k_0^2 - \left(\frac{\pi}{L}\right)^2 - \left(\frac{\pi}{b}\right)^2}\right) = \sqrt{\left(\frac{\pi}{L}\right)^2 + \left(\frac{\pi}{b}\right)^2 - k_0^2}\,. \tag{2.21}$$

Defining $C = L/b$ and $D = W/b$, the Eq. (2.21) can be rearranged as,

$$\sqrt{L^2\,\varepsilon_r\, k_0^2 - \pi^2 - \pi^2\, C^2}\, \tan\left(\frac{D}{2\,C}\sqrt{L^2\,\varepsilon_r\, k_0^2 - \pi^2 - \pi^2\, C^2}\right) = \sqrt{\pi^2 + \pi^2\, C^2 - L^2\, k_0^2}\,. \tag{2.22}$$

Defining the normalized resonant frequency F as

$$F = \frac{2\,\pi\, L\, f_0\, \sqrt{\varepsilon_r}}{c}\,, \tag{2.23}$$

Eq. (2.23) can be rearranged in the more convenient form:

$$\sqrt{F^2 - \pi^2 - \pi^2\, C^2}\, \tan\left(\frac{D}{2\,C}\sqrt{F^2 - \pi^2 - \pi^2\, C^2}\right) = \sqrt{\pi^2 + \pi^2\, C^2 - \frac{F^2}{\varepsilon_r}}. \tag{2.24}$$

If $L > W > b$, the last term (F^2/ε_r) on the right hand side of Eq. (2.24) does not have too much effect on the normalized resonant frequency F, as shown in Fig. 2.2. Eq. (2.24) can be rewritten as

$$\sqrt{F^2 - \pi^2 - \pi^2\, C^2}\, \tan\left(\frac{D}{2\,C}\sqrt{F^2 - \pi^2 - \pi^2\, C^2}\right) = \sqrt{\pi^2 + \pi^2\, C^2}. \tag{2.25}$$

The normalized resonant frequency F of the TE^x_{111} mode of a rectangular DR can be estimated by solving the prior equation. Figure. 2.2 illustrates the normalized resonant

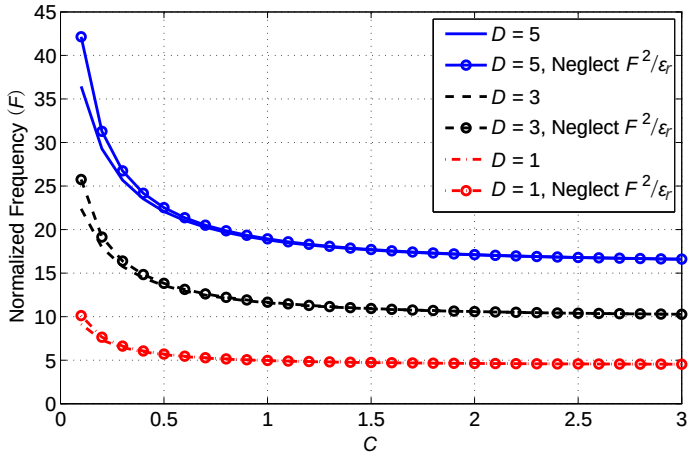

Figure 2.2. Normalized resonant frequency of the TE^{x}_{111} mode of a rectangular DR (ε_r=10) with different aspect ratio $C = L/b$ and $D = W/b$.

frequency of a rectangular DR with different aspect ratio of $C = L/b$ and $D = W/b$. For given rectangular DR dimensions and dielectric permittivity, the normalized resonant frequency can be found from this plot and Eq. (2.23). And vice versa, the dielectric permittivity and dimensions can be chosen from Fig. 2.2 for a desired resonant frequency.

2.3.2 Radiation Q-factor of the fundamental TE_{111} mode

The radiation Q-factor of the rectangular DRA is determined using [40]

$$Q = \frac{2\,\omega_0\,W_{\text{in}}}{P_{\text{rad}}}\,, \tag{2.26}$$

where $\omega_0 = 2\pi f_0$, W_{in} is the stored energy and P_{rad} is the radiated power. For a DR with high dielectric permittivity and low loss tangent δ, the stored electric energy is expressed as [40]

$$W_{\text{in}} = A\frac{\varepsilon_0\varepsilon_r LWb}{32}\left(1+\frac{\sin(k_x W)}{k_x W}\right)(k_y^2+k_z^2)\,, \tag{2.27}$$

where A is a constant related to the maximum amplitude of the fields. Since the TE_{111} mode of a rectangular DRA radiates like a magnetic dipole, the radiated power can be calculate by the following standard relation

$$P_{\text{rad}} = 10k_0^4|p_m|^2\,, \tag{2.28}$$

where p_m is the magnetic dipole moment of the DRA [40]

$$p_m = A\frac{-j\omega_0 8\varepsilon_0(\varepsilon_r-1)}{k_x k_y k_z}\sin(k_x W/2)\hat{x}\,. \tag{2.29}$$

Substituting Eqs. (2.27) and (2.28) into Eq. (2.26), the radiation Q-factor can be computed in relation to the dielectric permittivity and DR dimensions. It can be shown that the Q-factor is approximately proportional to $\varepsilon_r^{3/2}$. This agrees with physical intuition, which suggests that with the increase of dielectric permittivity, a larger part of the energy associated to the E field will be confined into the DR and the radiated power becomes small. Thus, the radiation Q-factor increases. Since the Q-factor is inversely proportional to bandwidth, the bandwidth of the DRA will decrease.

2.3.3 Methods for excitation of the fundamental TE_{111} mode

The performance of DRA is mainly determined by the excited mode, coupling between DR and feeding network, and impedance matching. It is obvious that a suitable coupling scheme between the transmission line and the radiating structure is one of the crucial parts in antenna design. The generic design principle for DRAs is based on field distributions of the modes and coupling coefficient k, which is determined by using Lorentz Reciprocity Theorem and coupling theory [43]. For an electric current source $\vec{J}_E$ and magnetic current source $\vec{M}_H$

$$k \propto \int (\vec{E} \cdot \vec{J}_E) dV \,, \tag{2.30}$$

$$k \propto \int (\vec{H} \cdot \vec{M}_H) dV \,, \tag{2.31}$$

where $\vec{E}$ and $\vec{H}$ are the normalized electric and magnetic field intensity of the considered mode. The equations indicate that in order to achieve efficient coupling between an electric (magnetic) source and the DR, the source should be placed in the vicinity of the strongest electric (magnetic) field for the desired mode of the DR.

Figure 2.3(a) sketches the E-field distribution of TE_{111} mode inside a rectangular DR. The pure TE_{111} mode radiates a broadside linear polarized radiation pattern, as shown in Fig. 2.3(b). Bearing the field distribution in mind, exciting structures for TE_{111} mode are illustrated in the following sections.

The coaxial probe

Using a coaxial probe is one of the simplest methods to exit TE_{111} mode of a rectangular DRA. As shown in Fig. 2.4, a probe, located adjacent to the outside boundary of a rectangular DR or slightly inset into it, is connected to a SMA coaxial connector

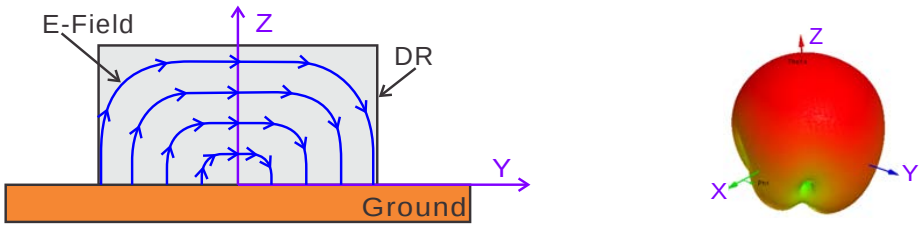

(a) E-Field distribution of TE_{111} mode (b) Radiation pattern of TE_{111} mode

Figure 2.3. Near and far field of TE_{111} mode.

through the ground plane. In some designs, a flat metallic strip on the side wall of the DR is used instead of a probe [44]. The probe or strip can be regarded as a vertical electric current. The radius and length of the probe (or width and length of strip) can be optimized to match the input impedance of the structure to the impedance of the feeding line. Normally, the length of probe (or strip) is less than the height of the DRA to avoid unwanted parasitic radiation from the probe (or strip). The main advantage of coaxial probe excitation is that it allows direct coupling into a 50 Ω feeding system without a bulk feeding network.

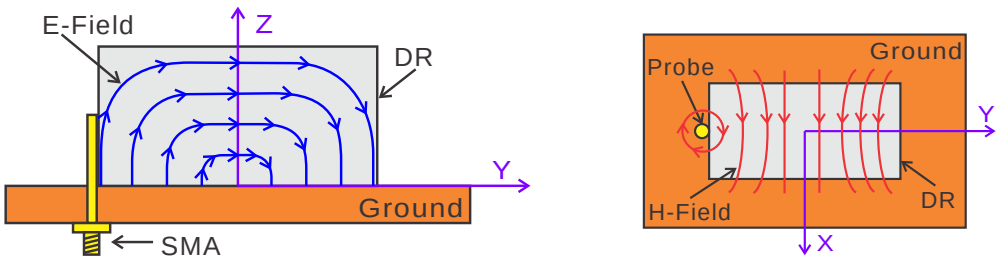

(a) E-Field distribution (Side view) (b) H-Field distribution (Top view)

Figure 2.4. Probe coupling to a rectangular DR.

The microstrip line

In most designs, it is advantageous to introduce a substrate to support the feeding network, which offers a higher flexibility for impedance matching than coaxial probe excitation and can be easily integrated with microwave circuits. As shown in Fig. 2.5 (a) and (b), an open microstrip line can feed the DR equivalently to a electric monopole. The open end of the strip can be located either at the side or underneath the DR. The size and shape of the open end have been tailored as a patch to match the feeding

network and achieve wide bandwidth, using for example a trapezoidal patch, elliptical patch or T-shaped patch [45–48]. Combined with these various patches, various DR geometries have been proposed to achieve desired performance, for example, H-shaped, cross-T-shaped, U-shaped and L-shaped DRs [45–48]. A shortingcoming of these arrangements is that the radiation from the feeding microstrip line might increase cross-polarization or decrease radiation pattern symmetry.

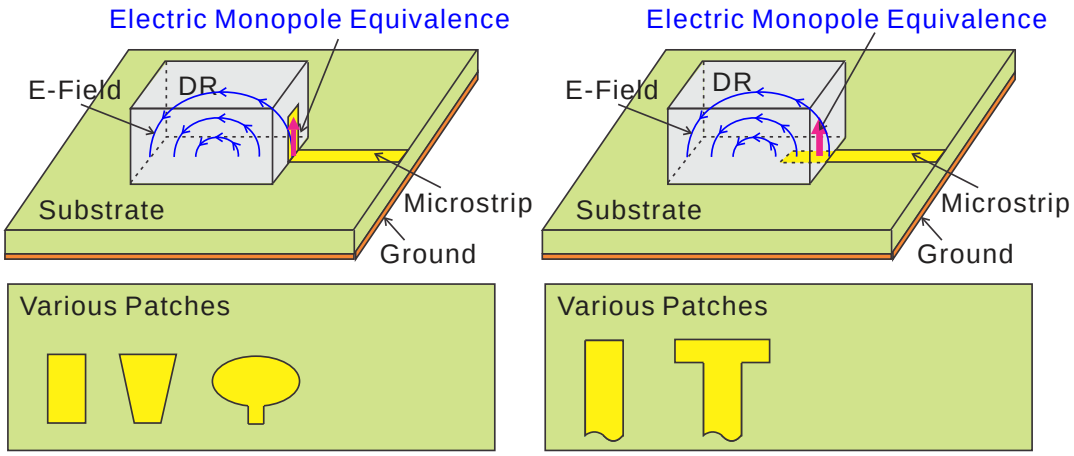

(a) Parasitic patch feeding (b) Microstrip feeding (underneath DR)

Figure 2.5. Microstrip line coupling to a rectangular DR.

The slot aperture

The slot aperture corresponds to a horizontal magnetic dipole, as shown in Fig. 2.6. The slot aperture coupling can be conveniently integrated on a substrate. The slot length should be large enough to achieve sufficient coupling between the DR and the feeding line. However, a large aperture might also resonate within the operation band, which usually results in a significant radiated back lobe. Therefore, the slot size design is a tradeoff between proper coupling to the DR and avoidance of excessive back radiation. As a rule of thumb [49,50], a good starting values of slot length l_s and slot width w_s are

$$l_s = \frac{0.4\lambda_0}{\sqrt{\varepsilon_e}} \tag{2.32}$$

$$w_s = 0.2 l_s \tag{2.33}$$

where λ_0 is the free-space wavelength, $\varepsilon_e = (\varepsilon_r + \varepsilon_s)/2$, ε_r and ε_s are the relative dielectric permittivity of the DRA and substrate, respectively. Depending on the specific

applications, the slot shape and dimensions can be tailored to improve performance and meet specific requirements. For example, a H-shaped slot is utilized to suppress the slot mode around the DR resonance in [51]; in the same design, the slot is further rotated 90 degrees (referred as I-shaped slot) to improve coupling from a rectangular waveguide to the DR; in [52], wideband DRAs are realized by using two parallel bowtie-slots; a circular polarization (CP) operation is achieved by using two cross slots with different length in [53]; the CP bandwidth is increased to 4.7% by optimizing the slot lengths and the distance of each slot to the open-end of the feeding microstrip line [54]. In most case, the slot is excited by an open-end microstrip line, and a stub is utilized to achieve better impedance matching. The usual starting point for optimization of the stub length is about $\lambda_s/4$, where $\lambda_s = \lambda_0/\sqrt{\varepsilon_s}$ is the guided wavelength of the microstrip line. The stub length might need to be optimized according to the location, size, shape of slot and feeding network.

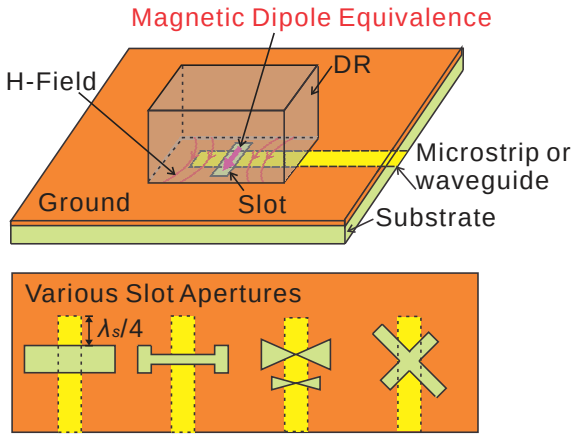

Figure 2.6. Slot aperture coupling to a rectangular DR.

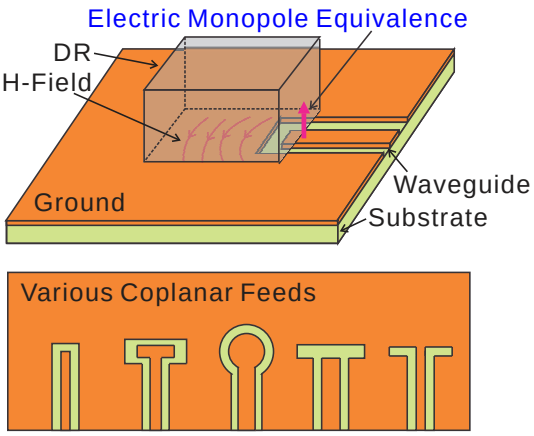

Figure 2.7. Coplanar waveguide coupling to a rectangular DR.

Coplanar waveguide

The feeding of DRs through a shorted coplanar waveguide (CPW) can provide an electric monopole equivalence, which is in principle similar to a coaxial probe, as shown in Fig. 2.7. A CPW is a planar transmission line patterned on the ground plane. It consists of a centre strip separated from the ground planes located on the same side of substrate by two slots [55]. Compared to coaxial probe feeding, the CPW-based feeding has advantages of manufacture simplicity and easy integration on the substrate without the requirement of drilling hole in the substrate. Furthermore, the equivalent electric monopole created by a shortened CPW can be placed underneath the DR without

drilling hole into the DR, which reduces not only the fabrication complexity but also the interference with the field distribution of the excited modes. Figure 2.7 illustrates some CPW examples, including an open-circuit line [56, 57], coplanar loops [58, 59] and stub-loaded lines [60–62]. The coplanar feed should be large enough to ensure the effective coupling, but small enough to reduce the back lobe of radiation pattern.

Substrate integrated waveguide and half-mode substrate integrated waveguide

The feeding loss of the conventional metal-based excitation methods becomes considerable in the millimeter wave frequency range due to the increasing inherent conductor losses. On the contrary, the low loss rectangular waveguide excitation method is bulky, expensive and not suitable for low profile and monolithic microwave integrated circuit fabrication techniques. Recently, the concept of substrate-integrated waveguide (SIW) has been proposed for designing high-performance and low-cost microwave and millimeter-wave components and antennas [63, 64]. Antennas [65, 66], antenna arrays [67], filter [68] and frequency-selective surface [69] based on SIW have been realized using standard PCB processes.

The SIW is a waveguide-like structure fabricated in planar form by using periodic metallic via holes to create side confinement, as shown in Fig. 2.8(a). The SIW works usually in the fundamental rectangular waveguide mode and the field distribution is sketched in Fig. 2.8(b). Along the propagation direction, the maximum value of the field is located at the vertical centre plane, which can be then considered as equivalent to a magnetic wall. Based on this property, the half-mode SIW (HMSIW) has been proposed halving the SIW and exploiting the open side aperture as equivalent magnetic wall in [70]. As shown in Fig 2.9(a) and (b), the HMSIW has a similar field distribution as a half SIW, while the size has been reduced by almost half.

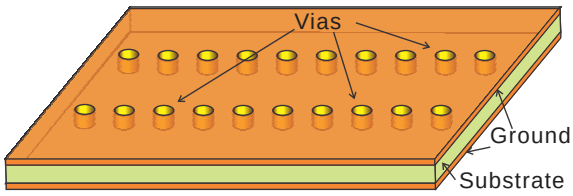

(a) The structure of SIW.

NOTE:
This figure/table/image has been removed to comply with copyright regulations.
It is included in the print copy of the thesis held by the University of Adelaide Library.

(b) Field distribution of SIW fundamental mode (from [70]).

Figure 2.8. SIW structure and field distribution.

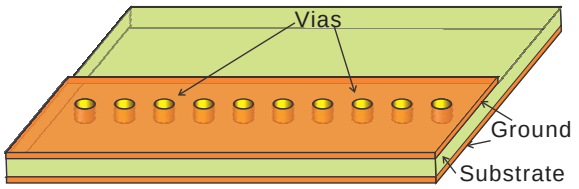

(a) The structure of HMSIW.

NOTE:
This figure/table/image has been removed to comply with copyright regulations.
It is included in the print copy of the thesis held by the University of Adelaide Library.

(b) Field distribution of HMSIW fundamental mode (from [70]).

Figure 2.9. HMSIW structure and field distribution.

Considering that previous research has demonstrated the high radiation efficiency of DRA in the millimeter-wave frequency range [11], the combination of a DRA and SIW can be a successful candidate for millimeter-wave antenna. For example, a 37 GHz high efficiency rectangular DRA fed by SIW structure has been proposed in [71]. Two prototypes, shown in Fig. 2.10, illustrate that the fundamental TE_{111} mode can be excited by using two different slot orientations. The DR and SIW are fabricated from Rogers® RT/6010 and RT/5870 substrates with relative dielectric permittivity of 10.2 and 2.33, respectively. A broadside gain of 5.51 dB and maximum -19 dB cross polarized radiation are achieved in the measurement. The simulated radiation efficiency is more than 95%. The design is further extended to 4 elements DRA array with radiated gain of 11.7 dB over a operating impedance bandwidth of 4.7% [72].

NOTE:
These figures/tables/images have been removed to comply with copyright regulations.
They are included in the print copy of the thesis held by the University of Adelaide Library.

(a) Transverse slot

(b) Longitudinal slot

Figure 2.10. SIW fed rectangular DRA. (adapted from [71])

2.4 Cylindrical dielectric resonator antenna

The cylindrical DR offers three fundamental modes, denoted as $HEM_{11\delta}$, $TM_{01\delta}$ and $TE_{01\delta}$. These modes can be excited within a single cylindrical DRA element, which

makes it a suitable potential candidate for multiband, multifunction or diversity applications [19, 25, 73]. In some cases, the cylindrical DR is modified to an annular shape to increase the number of degrees of freedom and achieve enhanced performance, for example, increasing bandwidth, improving coupling or shifting resonant frequency.

2.4.1 Field distribution, resonant frequency and Q-factor of fundamental modes

The field distributions of the $HEM_{11\delta}$, $TM_{01\delta}$ and $TE_{01\delta}$ modes of a cylindrical DR are sketched in Fig. 2.11 (adapted from [7]). The $HEM_{11\delta}$ and $TE_{01\delta}$ modes have been widely used to radiate broadside and omnidirectional radiation patterns, as shown in Fig. 2.12(a) and (b), respectively. The $TE_{01\delta}$ mode has traditionally been used in filters or oscillators in circuit applications due to its intrinsically high Q-factor. The concept of using $TE_{01\delta}$ mode as a radiating-mode is validated through demonstration of a horizontally polarized DRA in Chapter 5. This $TE_{01\delta}$ mode radiates like a vertical magnetic dipole over a ground plane, as shown in Fig. 2.12(c).

(a) $HEM_{11\delta}$ mode (b) $TM_{01\delta}$ mode (c) $TE_{01\delta}$ mode

Figure 2.11. Field distribution of three fundamental modes in a cylindrical DR. (adapted from [7])

Unlike in the case of the rectangular DR, there is no exact solution for the resonant modes of the cylindrical DR. The approximate approaches of deriving the field for a cylindrical DR are omitted here and the interested reader is referred to the literature, e.g. [7, 38], for detailed expressions. The equations of the resonant frequency and Q-factor of the $HEM_{11\delta}$, $TM_{01\delta}$ and $TE_{01\delta}$ modes are based on extensive numerical

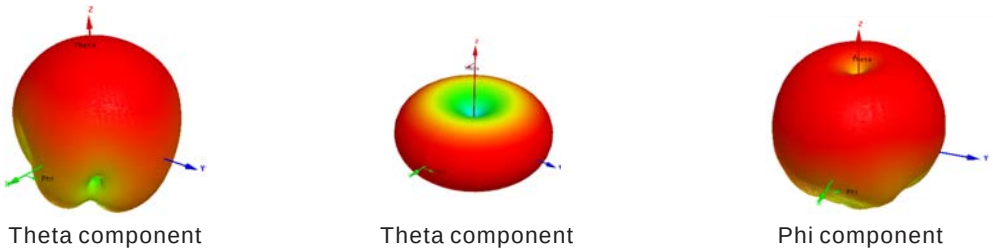

(a) $HEM_{11\delta}$ mode (b) $TM_{01\delta}$ mode (c) $TE_{01\delta}$ mode

Figure 2.12. Radiation patterns of three fundamental modes of a cylindrical DR.

simulations and the closed-form expressions describing the dependence for different geometrical parameters are approximated subsequently by curve fittings. Different literature sources [7,36,38] provide different formulas to calculate the resonant frequency and Q-factor, but generally these formulas give similar results with good approximation. The equations from [36] are given below, where $k_0 = 2\pi f_0/c$ denotes the free space wavenumber corresponding to the resonant frequency f_0 and c is the velocity of light in free space. Here, x is equal to a/h, where a and h are cylindrical DR radius and height, respectively. The modes are as follows:

- The $HEM_{11\delta}$ mode

$$k_0 a = \frac{6.324}{\sqrt{\varepsilon_r + 2}} \left\{ 0.27 + 0.36\frac{x}{2} - 0.02\left(\frac{x}{2}\right)^2 \right\} \tag{2.34}$$

$$Q = 0.01007\varepsilon_r^{1.3} x \left\{ 1 + 100e^{-2.05(x/2 - x^2/80)} \right\} \tag{2.35}$$

- The $TM_{01\delta}$ mode

$$k_0 a = \frac{\sqrt{3.83^2 + (\pi x/2)^2}}{\sqrt{\varepsilon_r + 2}} \tag{2.36}$$

$$Q = 0.008721\varepsilon_r^{0.888413} e^{0.0397475\varepsilon_r} \left\{ 1 - (0.3 - 0.2x)\left(\frac{38 - \varepsilon_r}{28}\right) \right\} \left\{ 9.498186x + 2058.33x^{4.322261} e^{-3.50099x} \right\} \tag{2.37}$$

- The $TE_{01\delta}$ mode

$$k_0 a = \frac{2.327}{\sqrt{\varepsilon_r + 1}} (1 + 0.2123x - 0.00898x^2) \tag{2.38}$$

$$Q = 0.078192\varepsilon_r^{1.27} \left(1 + \frac{17.31}{x} - \frac{21.57}{x^2} + \frac{10.86}{x^3} - \frac{1.98}{x^4} \right) \tag{2.39}$$

Fig 2.13 shows the calculated k_0a and radiation Q-factor of the $HEM_{11\delta}$, $TM_{01\delta}$ and $TE_{01\delta}$ modes obtained using these equations. In all these graphs, the relative permittivity of the cylindrical DR is chosen as $\varepsilon_r = 10$, as this will be used in the future design. For a given dielectric permittivity, the resonant frequency and Q-factor can be selected by choosing the radius and height.

Figure 2.13(a) indicates that the k_0a (and thus the resonant frequencies) of the $HEM_{11\delta}$, $TM_{01\delta}$ and $TE_{01\delta}$ modes can be very close. On the other hand, due to the orthogonal field distribution of these modes, the mutual coupling between pure modes is theoretically zero. These two characteristics for those modes offers the possibility of designing a single DR operating independently in multiple modes without interferences. By varying a and h, the resonant frequencies of these modes can be made very close. For example, in [19], the $HEM_{11\delta}$ and $TM_{01\delta}$ modes are excited to achieve a circular polarized radiation pattern for GPS-L band (1.575 GHz) applications and omnidirectional radiation pattern for WLAN applications (2.45 GHz), respectively. Other choices of parameters can be chosen to even have the bandwidth of different modes overlapping, e.g. for the design a multiband or diversity antennas. In Chapter 6, a diversity annular cylindrical DRA realizing simultaneously omnidirectional horizontally and vertically polarized radiation is proposed by using the $TE_{01\delta}$ and $TM_{01\delta}$ modes, respectively.

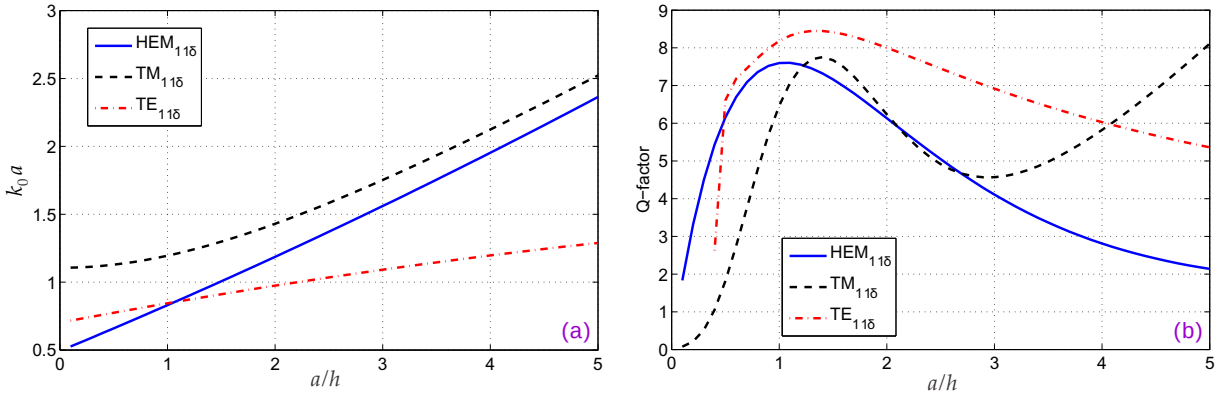

Figure 2.13. (a) k_0a and (b) Q-factor of the $HEM_{11\delta}$, $TM_{01\delta}$ and $TE_{01\delta}$ modes of a cylindrical DR with ε_r=10.

2.4.2 $HEM_{11\delta}$ and $TM_{01\delta}$ mode excitation methods

The $HEM_{11\delta}$ and $TM_{01\delta}$ modes in a cylindrical DRA can be excited by coaxial probe, microstrip line, slot aperture, coplanar waveguide, SIW and HMSIW. The placement of feeding point determines the excited mode, i.e. placing it at the edge a cylindrical DR,

couples to the $HEM_{11\delta}$ while in the centre, it excites the $TM_{01\delta}$ mode. As most of feeding structures mentioned in the previous section for the case of the rectangular DR can be applied similarly for the cylindrical DR, only the fundamental feeding structures are shown as illustration in this section.

The coaxial probe

The coaxial probe provides a simple way to couple energy to a cylindrical DR without using a bulky feeding network. To achieve maximum coupling, the probe should be located at the place with the maximum electric field intensity. According to the field distribution in Fig. 2.11.(a) and (b), the maximum electric field intensity of the $HEM_{11\delta}$ and $TM_{01\delta}$ mode are located at the periphery and centre of the cylindrical DR, respectively. Therefore, to excite either mode, the probe should be correspondingly placed at the periphery or centre, as shown in Fig. 2.14. The impedance can be matched by optimizing the height and the radius of the probe. To excite the $TM_{01\delta}$ mode, the centre of the cylinder has to be removed to hold the probe, which increases the manufacture difficulty. This can be avoided by using slot aperture or coplanar waveguide, as shown in the following sections.

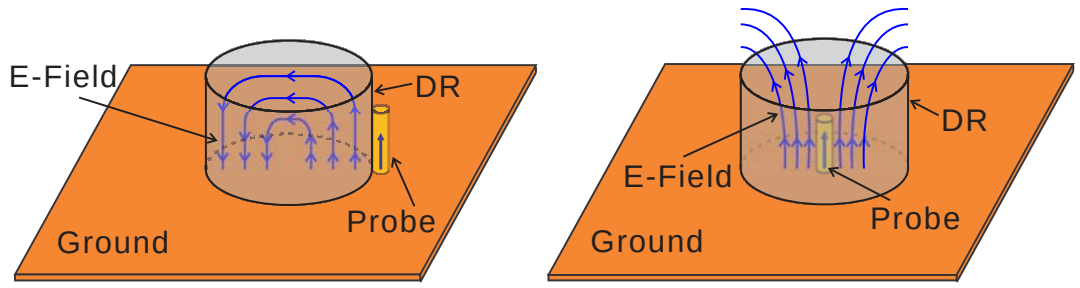

(a) $HEM_{11\delta}$ mode excitation (b) $TM_{01\delta}$ mode excitation

Figure 2.14. Probe coupling to a cylindrical DR.

The microstrip line

The microstrip line is usually employed to excite the $HEM_{11\delta}$ mode. The feeding point can be located underneath the DR or can be connected to a strip on the periphery of the DR, as shown in Fig. 5.1. The maximum coupling is achieved by optimizing the shape and length of the microstrip stub or by adding a parasitic patch [74].

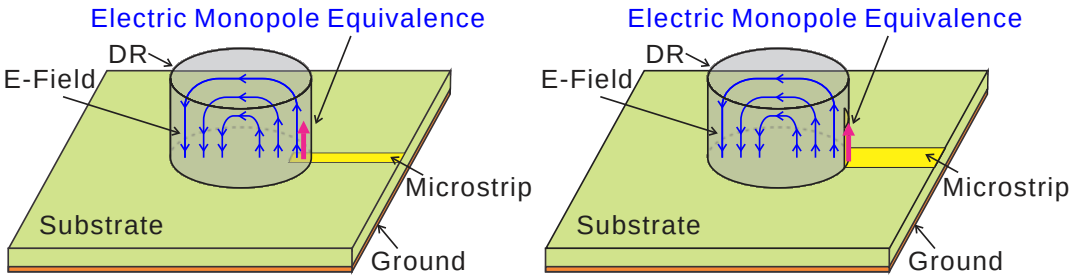

(a) Microstrip feeding (underneath DR) (b) Parasitic patch feeding

Figure 2.15. Microstrip line coupling to a cylinder DR.

The slot aperture

A slot aperture is equivalent to a horizontal magnetic dipole magnetic current. It should be placed at the position of the maximum magnetic field intensity. Thus, the slot is located at the centre of the cylinder to excite the $HEM_{11\delta}$ mode and near the periphery for the $TM_{01\delta}$ mode, as shown in Fig. 2.16. The shape and number of the slots can be optimized to improve the DRA performance and bandwidth. For example, 33% impedance bandwidth is achieved by using double bowtie apertures in [52].

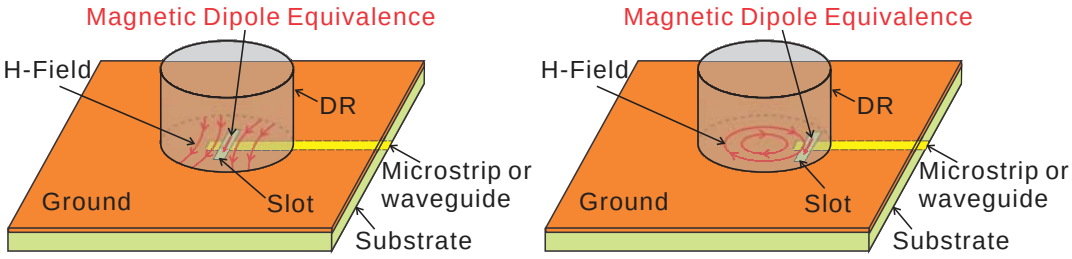

(a) $HEM_{11\delta}$ mode excitation (b) $TM_{01\delta}$ mode excitation

Figure 2.16. Slot coupling to a cylinder DR.

Coplanar waveguide

The coplanar waveguide provides an alternative method to excite the $HEM_{11\delta}$ or $TM_{01\delta}$ modes with the advantage of being nonobtrusive. As shown in Fig. 2.17, the excitation can be achieved by placing the coplanar loop at the edge ($HEM_{11\delta}$ mode) or in the centre ($TM_{01\delta}$ mode) of the cylinder since the coupling behavior of the coplanar waveguide is similar to that of the coaxial probe [58].

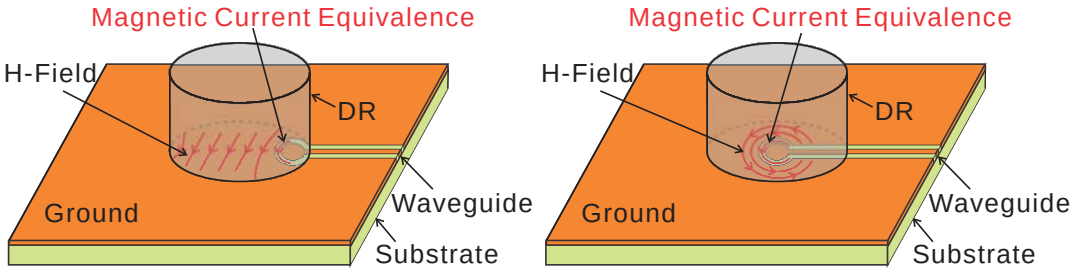

(a) $HEM_{11\delta}$ mode excitation (b) $TM_{01\delta}$ mode excitation

Figure 2.17. Coplanar waveguide coupling to a cylinder DR.

SIW and HMSIW

As mentioned previously, SIW and HMSIW provide a compact and efficient feeding scheme for DRAs operating at millimeter wave frequencies. In [75], 60 GHz linearly polarized (LP) and circularly polarized (CP) HMSIW-fed DRAs are demonstrated by applying a transverse rectangular slot and a pair of cross slots to feed a cylindrical DR, respectively. The sketches of the proposed antenna configuration are shown in Fig. 2.18. A cylindrical DR is mounted on the a HMSIW structure formed by the top layer, ground layer and periodic via arrays. The energy is coupled from the waveguide to the DR thorough a slot aperture. The $HEM_{11\delta}$ mode is excited by the slot aperture which is equivalent to horizontal magnetic dipole. The LP HMSIW-fed DRA exhibits a bandwidth of 24.2% for ($|S_{11}|$ < -10 dB), as experimentally demonstrated. The gain is higher than 5.5 dB and the radiation efficiency is in a range between 80% and 92% over the whole operation band. The CP HMSIW-fed DRA achieves 3-dB axial ratio bandwidth of 4.0%. These results indicate that the HMSIW can be an efficient feed for DRAs operating at around 60 GHz, and more generally in the millimetre-wave range.

NOTE:
These figures/tables/images have been removed
to comply with copyright regulations.
They are included in the print copy of the thesis
held by the University of Adelaide Library.

(a) HMSIW feeding side (b) LP DRA (b) CP DRA

Figure 2.18. Sketches of the LP and CP HMSIW-fed DRA. (adapted from [75])

2.4.3 $TE_{01\delta}$ mode excitation method

The $TE_{01\delta}$ mode is usually utilized in filters and oscillators design [16,76,77] due to its intrinsically high quality (Q) factor. The $TE_{01\delta}$ mode can be excited by most available transmission line types [39], such as coaxial probe, microstrip line, waveguide, and image guide. In order to achieve the maximum power coupling between resonator and transmission line, the impedance of the resonator and feeding must be matched at the resonance frequency.

The magnetic field distribution of $TE_{01\delta}$ mode is equivalent to a magnetic dipole along the axis of the cylinder at the centre of DR, as shown in Fig. 2.11(c). Inspired by this fact, we propose to use the $TE_{01\delta}$ mode to radiate horizontally polarized omnidirectional patterns in Chapter 5. An airgap between the cylindrical DR and substrate is introduced to lower the Q-factor and thus increase the impedance bandwidth. Due to the symmetrical field distribution of the $TE_{01\delta}$ mode, a balanced coupling method described in [76] is utilized to obtain a symmetrical feeding, as shown in Fig. 2.19(a). The balanced coupling method is formed by placing two arc-shaped microstrip lines on each side of the DR. A bandwidth of 5.6% around the centre frequency of 3.9 GHz is achieved by further optimizing the shape of the microstrip lines [24]. To create a more uniform current loop distribution, four arc-shaped microstrip lines are utilized to design a horizontally and vertically polarized omnidirectional DRA in Chapter 6. The detailed design process will be explained in Chapter 5 and 6.

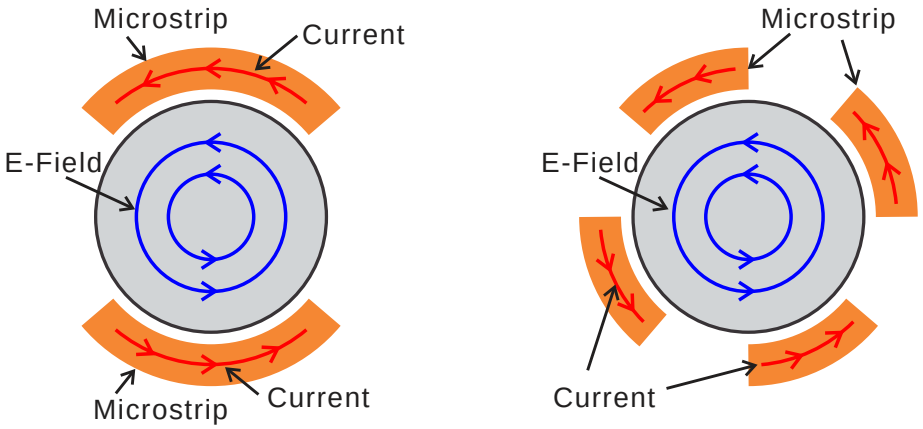

(a) Two arc-shaped microstrip lines (b) Four arc-shaped microstrip lines

Figure 2.19. A balanced coupling method to excite the $TE_{01\delta}$ mode in a cylindrical DR.

2.5 Conclusion

This chapter has reviewed two important aspects in DRA design, namely the DR geometry and the typical feeding mechanisms. The description of the resonant frequency, Q-factor and field distribution of fundamental modes in rectangular and cylindrical DRAs provides an in-depth understanding of the radiation properties of the canonical DRAs, which will in turn help to develop non-canonical shaped devices with enhanced performance. Furthermore, the possibility of designing multi-band and diversity DRA is considered through the analysis in terms of resonant frequency and field distribution for orthogonal modes.

The type and location of feeding methods not only affect the resonant mode, operational frequency and thus antenna radiation characteristics, but also have significant impact on the impedance bandwidth and radiation efficiency. Thus, the typical feeding methods, together with advanced feeding designs, have been described after the review of corresponding modes.

The chapter is a building block and fundamental study for this thesis. Based on a thorough understanding of the characteristics of the modes and feeding techniques, several high performance DRAs and an optical DRA reflectarray are presented in the following parts of the thesis.

Chapter 3

Circularly polarized dielectric resonator antenna

THIS chapter presents a wideband circularly polarized (CP) dielectric resonator antenna (DRA). A thin cross-shaped dielectric resonator (DR) of high permittivity is excited by two orthogonal microstrip lines with 90° phase difference resulting in radiation with circular polarization. The general design principles are described and finite-element simulations are employed to fine-tune the proposed antenna. The experimental results show a good agreement with simulation and demonstrate a broadside CP bandwidth of 13.2%. In conceptual evolution of the design, the symmetry of the radiation pattern and usable CP angle are improved by introducing a ground plane between antenna and feeding network.

3.1 Introduction

Circularly polarized (CP) antennas are widely used in communication systems to bypass problems of polarization mismatch and mitigate multipath interference. Recent research works on CP dielectric resonator antennas (DRAs) [30, 54, 78–81] have highlighted their potentially achievable higher gain and wider bandwidth for CP when compared with microstrip antennas. Some CP DRA designs employ canonical antenna geometries, including, rectangular [78], cylindrical [54, 79] and cross [30] shapes, combined with simple feed configurations, such as a probe [80], a slot aperture [79] or vertical strips [81]. The achieved broadside 3-dB axial ratio (AR) bandwidth of such structurally simple antennas remains normally below 7%.

The AR bandwidth can be improved by using novel dielectric resonators (DRs) geometries. In [82], a hollow rectangular DRA demonstrated a measured broadside AR bandwidth of 12.4%, which is about as 3 times higher than that of the corresponding solid CP DRA. Pan and Leung [83] proposed a trapezoidal DRA excited by a inclined slot with measured AR bandwidth of 21.5%. In [84], an AR bandwidth of 10.6% was achieved by using a rectangular stair-shaped DRA [84].

Alternatively, the AR bandwidth can be enlarged by employing a sophisticated feed network. An AR bandwidth of 14% was obtained by using a square spiral strip to excite a rectangular DRA with relative dielectric permittivity of 9.3 in [85]. To increase the AR bandwidth, a hybrid coupler is usually utilized to excite two orthogonal modes with 90° phase difference. For example, a cylindrical DRA with 20% AR bandwidth was achieved in [86] by using a hybrid coupler excitation. The hybrid coupler was printed on the top of the substrate, which increased the substrate size and introduced unwanted radiation from the hybrid coupler. A subsequent publication addressed this problem by placing the hybrid coupler in the hollow region of a hollow DRA [87]. The hollow CP DRA demonstrated an AR bandwidth as wide as 33.8%.

In addition, the AR bandwidth can also be increased by exciting both fundamental and higher order modes. In [88], the fundamental $HEM_{11\delta}$ ($0< \delta <1$) and higher order $HEM_{11\triangle}$ ($1<\triangle<2$) modes of a cylindrical DR were utilized to design a CP DRA which achieved an AR bandwidth of 24.7%. With a similar principle in [89], an AR bandwidth of 20% was obtained by merging the fundamental TE_{111} and the higher order TE_{113} modes in a rectangular DR.

In parallel to these broadside CP DRAs, an omnidirectional CP DRA with 7.3% AR bandwidth was realized by Pan et al. [90]. The omnidirectional CP radiation patterns are archived by exciting fundamental end-fire TM mode in a rectangular DR with slot diagonally across each side wall. The AR bandwidth was further increased to 25.4% by introducing a parasitic strip in each slot [91].

This chapter demonstrates a different configuration, where a wide impedance and AR bandwidth are achieved using a cross-shaped DR composed of high-dielectric thin plates. With the proposed structure, an impedance bandwidth of 21% and overlapping broadside CP bandwidth of 13% have been achieved. It is worthwhile to remark that the proposed design principle is also valid for low permittivity material. By using thin plates of high relative permittivity of 50 to build the DR, the size and dielectric volume of the antenna can be however significantly reduced. In an evolution presented at the end of this chapter, the performance of the proposed antenna is further improved by introducing a ground plane between antenna and feeding network. The proposed antenna structure provides a preliminary study for the multi-function DRA in the next chapter.

3.2 Circularly polarized DRA configuration

The cross-shaped CP DRA excited by a slot aperture was firstly proposed by Ittipiboon et al. [30]. The CP operation can be obtained by adjusting the length of two arms to resonate in phase quadrature. In their work, a CP bandwidth of 4% has been achieved by using low permittivity dielectric (ε_r = 10.8) material. In the design evolution presented in [92], four cross-shaped DRAs have been utilized to compose a 2×2 array fed by sequential rotation, which increases the CP bandwidth to 16%.

This section introduces a further development of cross-shaped DRA for circular polarization. Compared with previous cross-shaped antennas, the length of two arms of the proposed antenna is kept equal and the CP operation is achieved by a feeding scheme exciting two orthogonal fundamental TE_{111} modes in the two cross arms with 90° phase difference. The field distribution of the excited TE_{111} mode can be found in Fig. 2.4. The configuration of the CP cross-shaped DRA is sketched in Fig. 3.1. The DRA consists of a cross-shaped high-permittivity DR mounted on a FR4 substrate.

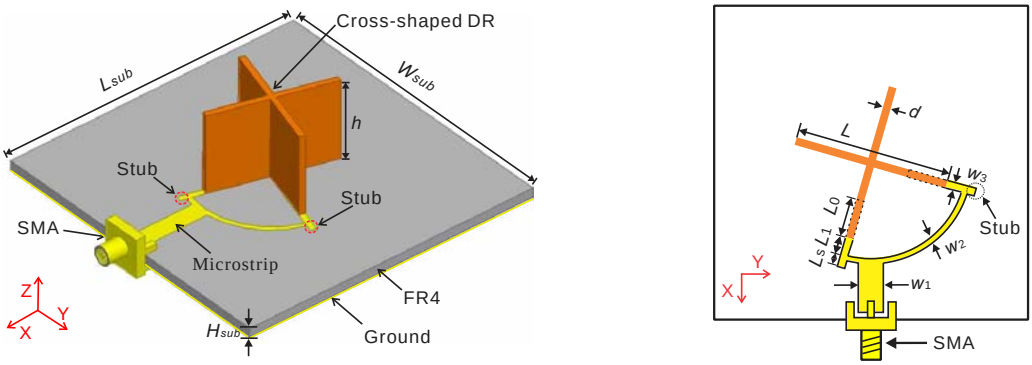

(a) 3D view.

(b) Top view.

Figure 3.1. Cross-shaped CP DRA configuration.

3.2.1 DR design

The DR design is based on a 1 mm thick dielectric plate of relative permittivity 50. The length L and height h of the two arms of the cross are first designed without considering the mutual interaction between the two arms. Given the thickness (d = 1 mm) of the plates and the selected resonance frequency (4.5 GHz), an initial length L and height h are determined using the dielectric waveguide model (DWM) [40], as described by Eq. (2.17-2.18). Figure 3.2 shows the calculated DR length and height for a TE_{111} mode resonance at 4.5 GHz as obtained using these equations. In the same Fig. 3.2, the dashed curve (related to the right-hand side y-axis) shows the surface of the 1 mm plate for the corresponding resonance. The DR length of 20 mm and height of 9.8 mm are initially selected to minimize the DR side surface area, since this choice minimize the use of the dielectric material.

Based on this initial calculated DR size, the DRA element is simulated and optimized with Ansoft® HFSS employing the finite-element method (FEM) in the frequency-domain. It is worth emphasizing that Eq. (2.17-2.18) are not valid for this very thin dielectric material. In the simulation, a height of 13 mm has to be used to achieve 4.5 GHz resonance frequency instead of the initially calculated 9.8 mm.

In order to investigate the influence of the plate thickness on the effective permittivity, rectangular DRs with the same length of 20 mm and different thickness are simulated in HFSS. The resonance at 4.5 GHz is achieved by varying the DR height, as shown in the left-hand side y-axis of Fig. 3.3. For comparison with the standard DWM model, an effective permittivity of the thin plate is determined using the Eq. (2.17-2.18) with

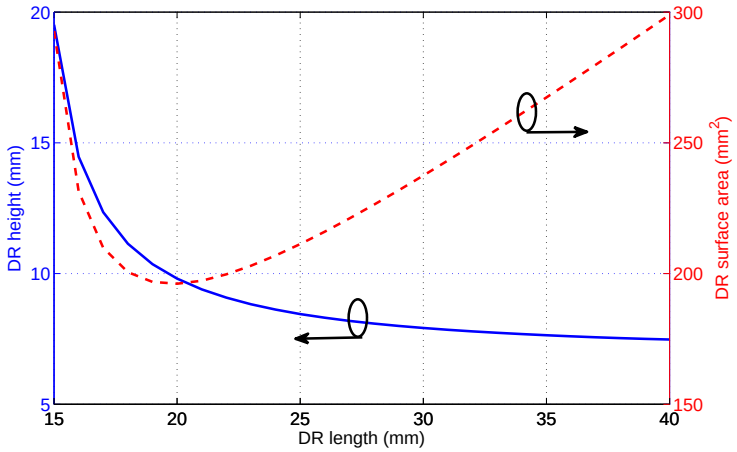

Figure 3.2. Calculated DR length and height for a resonance at 4.5 GHz. Thickness of 1 mm dielectric plate with relative permittivity 50.

the simulated thickness and height of DR, as shown in the right-hand side y-axis of Fig.3.3. The simulated and calculated results in Fig. 3.3 reveal that the effective permittivity of the 1 mm dielectric slab is about 42.6. The effective permittivity converges and become close to the real relative permittivity value when the thickness of the slab becomes thicker than 5 mm, which corresponds to $0.5\lambda_{\varepsilon_r}$. Here, λ_{ε_r} is the wavelength in the material with relative permittivity of ε_r. If the thickness of the cross plates is increased to the same value as the length, the DR shape will be transferred from a cross to a square but the effective relative permittivity will become in this case equal to 50. In other words, the effective permittivity of a solid square DR is equal to the real permittivity of the resonator material. That is the reason why the thin cross-shaped DR is selected in this design instead of a solid rectangular or cylindrical DR. The thin cross shape will lower the effective permittivity and consequently increase bandwidth. This principle has been proved by using a hollow rectangular DRA in [87].

The observed discrepancy indicates that field extends into the air outside of the resonant dielectric material when thin plates are used. To prove that, the E field distribution around the DR is plotted in a plane placed on the top of the DR, where the strongest E field amplitude occurs for the excited TE_{111} mode, as shown in Fig. 3.8. The two DRs have the same relative permittivity of 50 and arm length of 20 mm. To resonate at 4.5 GHz, the left-hand DR has arm thickness of 1 mm and height of 13 mm, while the right-hand DR has arm thickness of 4 mm and height of 3.3 mm. Figure 3.8 illustrates that the field extension outside the thin DR is more pronounced than that of the thick

DR. Although the discrepancy from the DWM model for the thin material are significant, the Eq. (2.17-2.18) still can provide a starting point for the design with numerical simulation tools.

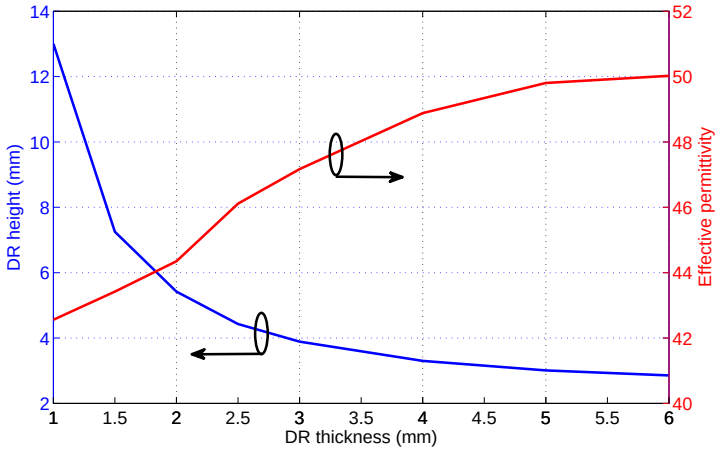

Figure 3.3. Simulated DR height and corresponding effective permittivity for a resonance at 4.5 GHz with different thickness.

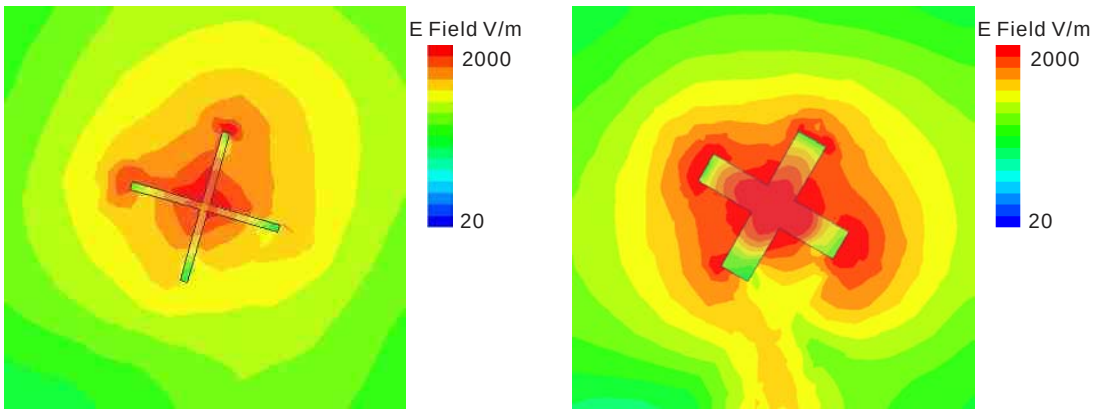

(a) Cross-shaped DR with arm thickness of 1 mm and height of 13 mm.

(b) Cross-shaped DR with arm thickness of 4 mm and height of 3.3 mm.

Figure 3.4. Simulated E filed distribution in a plane placed on the top of two DRs. The two DRs have the same relative permittivity of 50, arm length of 20 mm, and resonance frequency of 4.5 GHz.

Table 3.1. Antenna parameters of the CP DRA

Symbol	Value	Symbol	Value
L	20 mm	h	13 mm
d	1 mm	L_0	5 mm
L_1	2.8 mm	L_s	0.9 mm
w_1	3.2 mm	w_2	0.76 mm
w_3	1 mm	H_{sub}	1.6 mm
L_{sub}	70 mm	W_{sub}	70 mm

3.2.2 Feeding network design

The cross-shaped DR is excited by two orthogonal microstrip lines printed on a FR4 substrate with relative permittivity of 4.2 and thickness of 1.6 mm, as shown in Fig. 3.1. To realize an appropriate feeding network, a T-junction splitter is utilized to connect two curved 100 Ω transmission lines to the feeding 50 Ω transmission line [19]. The 50 Ω line is connected to a network analyzer Agilent N5230A through a SMA coaxial connector. By optimizing the length of the microstrip line segment underneath the two DR arms, a 100 Ω input impedance is achieved at the end of each transmission line. Furthermore, the 90 degree phase difference is obtained by adjusting the angular location of the T-junction. As a result, the effective path difference between the T-junction and the end of the two microstrip lines is a quarter wavelength at 4.5 GHz. Through the simulation process, two small stubs are added to cancel reflection and increase the impedance bandwidth, as shown in Fig. 3.1. The final antenna parameters are tabulated in the Table 3.1.

3.3 Experimental results

A prototype of the optimized device has been manufactured as shown in Fig. 3.5. The cross is composed of two notched rectangular slices of the same size cut from a high-permittivity substrate with ε_r = 50, as shown in the inset of Fig. 3.5. The depth of the notch is the half height of the DR plates to provide mechanical stability of the cross and the width of notch is 1 mm. The cross-shaped DR is glued on the fabricated FR4 substrate.

Figure 3.6 illustrates the simulated and measured reflection coefficient. The measured impedance bandwidth ($|S_{11}| <$ -10 dB) covers a frequency range from 4.25 to 5.25 GHz.

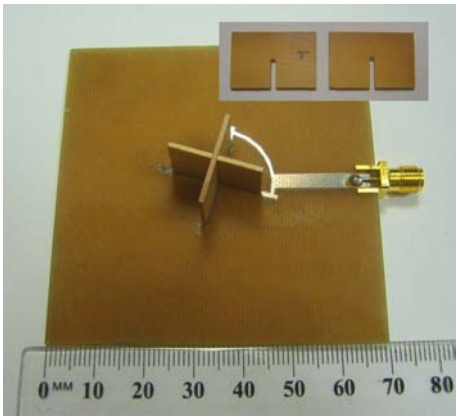

Figure 3.5. Realized prototype of cross-shaped DRA. Inset: Notched rectangular dielectric plates forming the cross-shaped DRA.

There is a 0.1 GHz offset between the initial simulation, on which the prototype is based, and measurement results performed with the prototype. This discrepancy most probably arises from fabrication imperfections, e.g. from the glue layer used to mount the DR on the FR4 substrate. To demonstrate the effect of a glue layer, several simulations have been performed for different thicknesses and dielectric properties of this glue layer. Figure 3.6 shows that the measured result can be matched to the simulated result by adding a 0.1 mm thick glue layer with relative permittivity of 2.

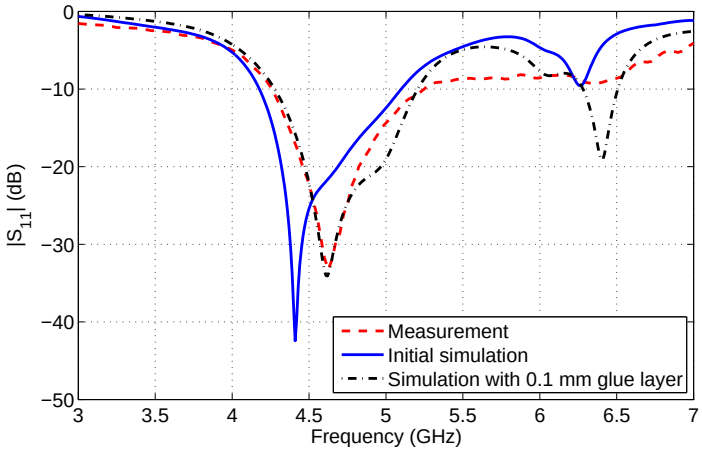

Figure 3.6. Simulated and measured reflection coefficient. The dash-dotted line shows the results obtained when a 0.1 mm thick glue layer with relative permittivity of 2 is added in the simulation to match the measured reflection coefficient.

The antenna AR is measured and calculated according to the third definition of Ludwig [93]. Figure 3.7 shows a comparison between simulated and measured AR in broadside direction ($\theta = 0°$). From the measurement, the minimum AR of 0.36 dB is

found at f = 4.78 GHz. The 3 dB AR bandwidth extends from 4.6 to 5.25 GHz, which yields an overlap with the impedance bandwidth of 13.2%. Similarly as the impedance bandwidth, the AR is also shifted by 0.07 GHz towards higher frequencies, which is also attributed to fabrication imperfection. Overall the agreement between simulation and measurement is satisfactory and the achieved usable CP bandwidth validates the design concept.

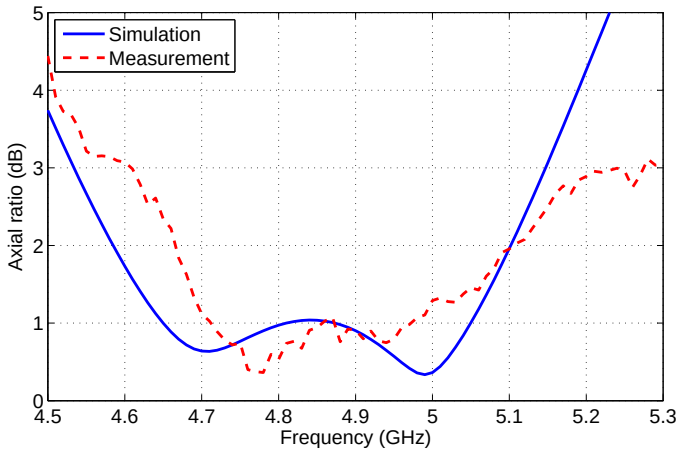

Figure 3.7. Simulated and measured axial ratio for the cross-shaped CP DRA.

The measured and simulated radiation patterns are depicted in Fig. 3.8 at frequencies 4.6, 4.78 and 5.25 GHz, respectively. Stable broadside patterns with right-hand CP (RHCP) polarization are obtained. The RHCP fields of XZ and YZ plane are at least 15 dB higher than the left-hand CP (LHCP) fields around the broadside direction. The asymmetry of the pattern is most probably due to the influence of the T-junction and the microstrip transmission line.

The gain of the prototype antenna was measured by using the gain-transfer method [94] in the anechoic chamber. The first step is to measure the power P_T received by the test antenna when illuminated by a transmitting broadband horn antenna (AEL H-1498, 2-18 GHz). In the second step, the antenna under test is replaced by a standard gain horn antenna (Narda 640) and the received power P_S is recorded. The gain of the test antenna can then be calculated by

$$G_T = G_S + 10\log_{10}\left(\frac{P_T}{P_S}\right) \tag{3.1}$$

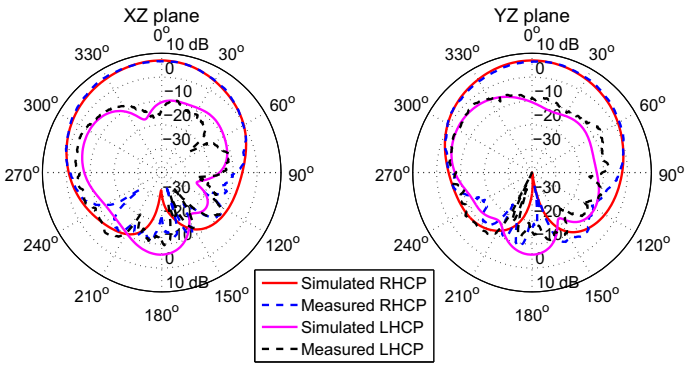

(a) Gain pattern at 4.6 GHz.

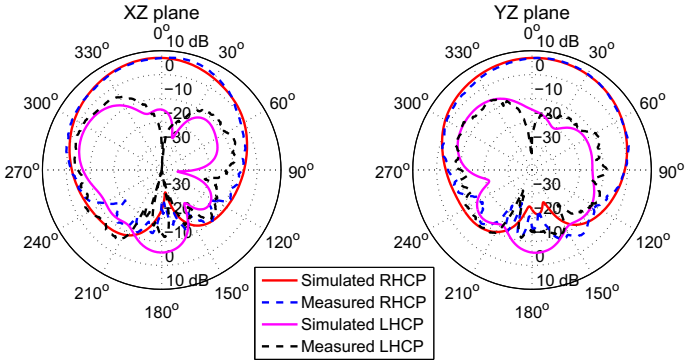

(b) Gain pattern at 4.78 GHz.

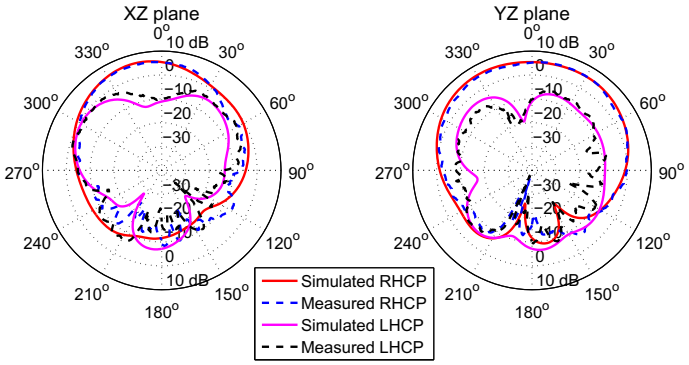

(c) Gain pattern at 5.25 GHz.

Figure 3.8. Simulated and measured radiation patterns at left, centre, and right of the CP band.

where G_T and G_S are the gain of the test and standard gain horn antenna, respectively. A comparison between the simulated and measured gain is shown in Fig. 3.9. A maximum gain of 6.17 dB is measured at 4.7 GHz. Within the usable 3 dB AR bandwidth, indicated as shaded area, the antenna gain remains above 3.5 dB.

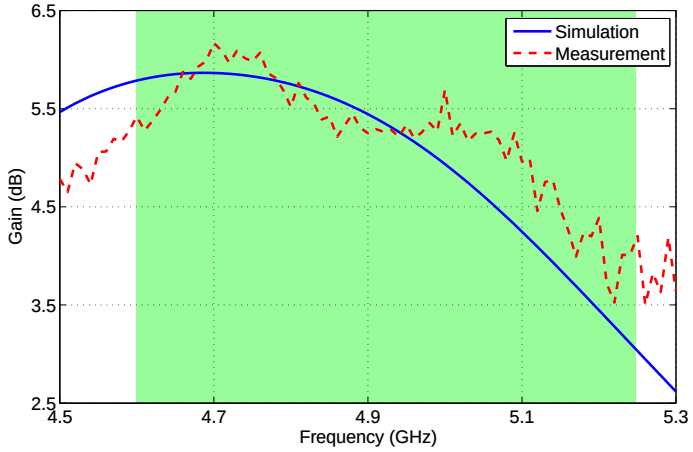

Figure 3.9. Simulated and measured RHCP gain. The shaded area is the CP bandwidth.

3.4 Radiation pattern improvement

The feeding network of the realized design introduces an asymmetry in the geometry which translates into asymmetric radiation patterns, as shown in Fig. 3.8. The asymmetry reduces the useable angle where circular polarization is maintained to less than 30° around broadside. To solve the problem, a physical separation between the antenna and the feeding network is introduced by moving the feeding network under the ground plane.

In the new improved design, the feeding network is separated into two layers, which are located one on top and one below the ground plane, as shown in Fig. 3.10. The design requires two FR4 substrates with backside metallization to hold both parts of the feeding network. Specifically, the T-junction and delay line are located on the bottom substrate to reduce their interaction with the DR, and thus their impact on the radiation pattern. Two vias with diameter of 1 mm are utilized to connect the T-junction to the feeding microstrip lines through holes in the substrates and ground plane. The improved design is simulated in HFSS and the optimized antenna parameters are tabulated in Table. 3.2.

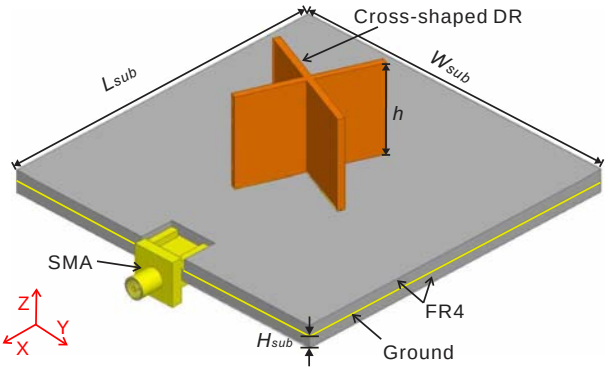

(a) 3D view.

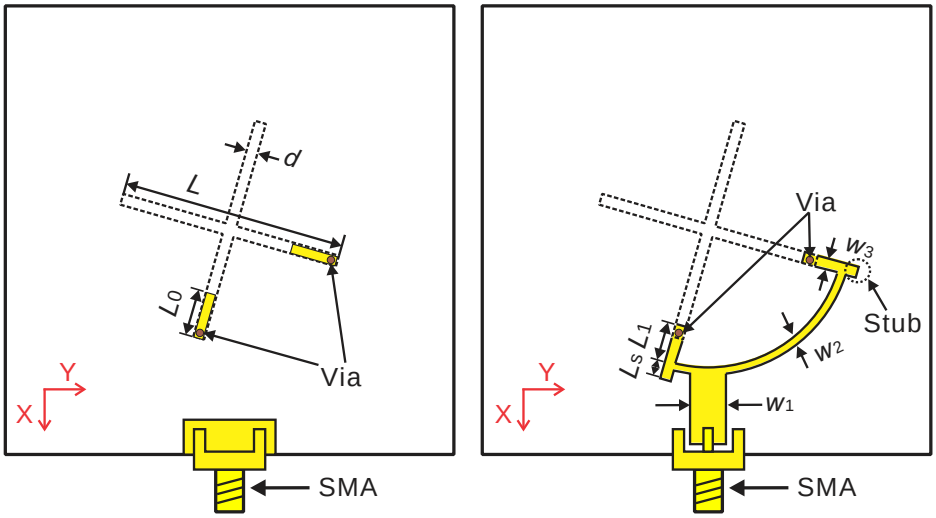

(b) Top view.

(c) Bottom view.

Figure 3.10. Sketch of the improved antenna design.

Table 3.2. Antenna parameters of the improved CP DRA

Symbol	Value	Symbol	Value
L	20 mm	h	13 mm
d	1 mm	L_0	5.2 mm
L_1	4.3 mm	L_s	0.9 mm
w_1	3.2 mm	w_2	0.76 mm
w_3	1 mm	H_{sub}	1.6 mm
L_{sub}	70 mm	W_{sub}	70 mm

The simulated impedance bandwidth (|S11| < -10 dB) covers a frequency range from 4.09 to 5.33 GHz, as shown in Fig. 3.11. Two resonant frequencies at 4.31 and 5.01 GHz result from the two arms of the cross-shaped DR. The overlap frequency of these resonance in two arms yields a CP operation from 4.41 to 4.89 GHz due to the 90 degree phase difference of these two resonances. The achieved 10% 3-dB AR bandwidth is shown in Fig. 3.12. The radiation patterns of left, centre and right AR bandwidth are illustrated in Fig. 3.13 (a), (b) and (c), respectively. Compared with Fig. 3.8, the symmetry of the radiation pattern and usable CP angle are improved. Figure 3.14 compares the usable CP angle of the initial design and improved design at the centre of the AR bandwidth in XZ and YZ plane. With the improved design, the usable CP angle is increased from 71° to 78° and from 101° to 123° in XZ and YZ plane, respectively. This performance improvement is obtained at the cost of increased fabrication complexity. This principle of separation of feeding network and antenna on both side of the ground plane has not been directly validated experimentally. It is however applied in the next chapter in the realization of a multifunction DRA.

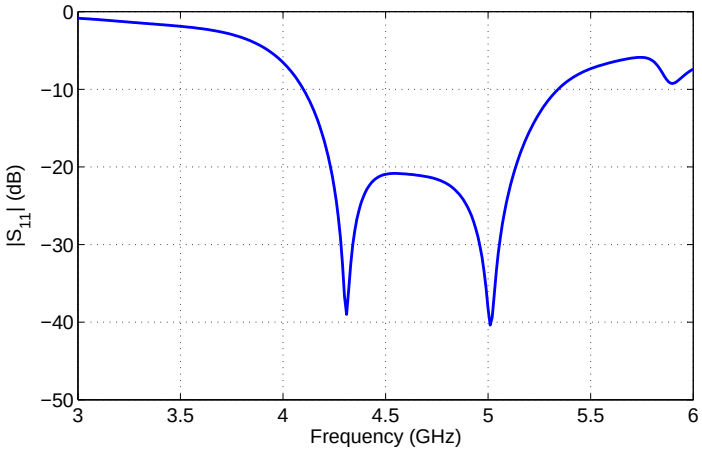

Figure 3.11. Simulated reflection coefficient of the improved design.

3.5 Conclusion

This chapter proposed a design of high-permittivity cross-shaped DRA for CP applications. In the two crossed equal-length arms of the DR, TE_{111} modes are excited by two orthogonal microstrip lines with 90° phase difference to generate circular polarization. The combination of high-permittivity material for the DRA and of a quadrature feed results in a compact design with an impedance bandwidth of 21% and a broadside CP

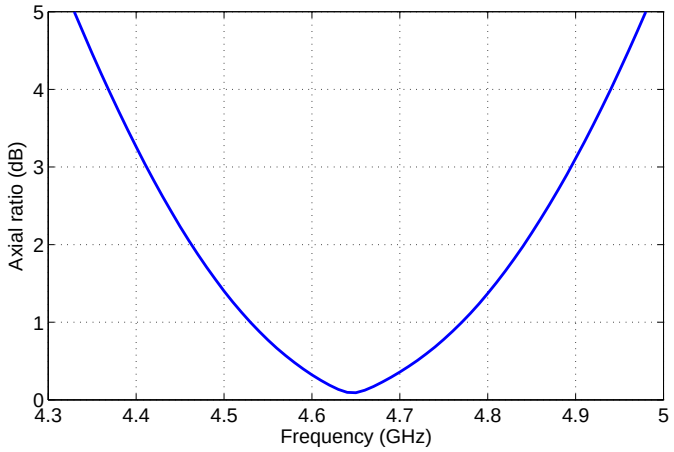

Figure 3.12. Simulated axial ratio of the improved design.

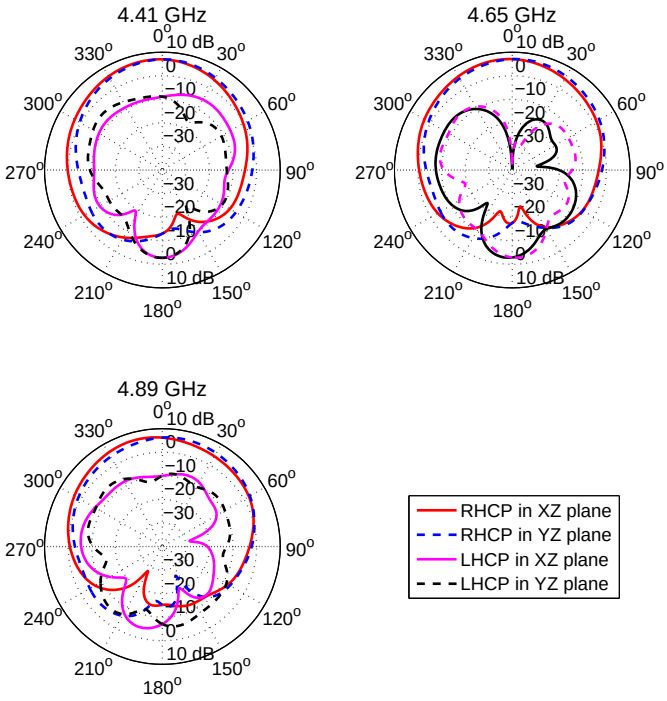

Figure 3.13. Simulated radiation pattern of the improved design.

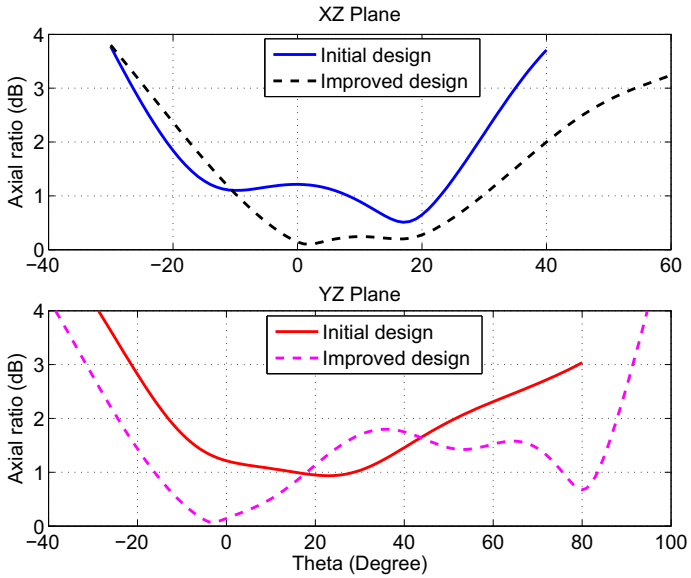

Figure 3.14. Simulated useable CP angle of the initial and improved design at the centre of the AR bandwidth.

bandwidth of 13.2%. The simple antenna configuration and feeding mechanism make this design easily scalable to other frequency bands.

The effective permittivity of the DR with relative permittivity of 50 has also been investigated in this chapter. With 1 mm thickness, the effective permittivity of the DR is around 42.6 due to the fact that field is extending into the air outside of the DR. The simulation result indicates that the effective permittivity is close to the real relative permittivity value when a DR operating at 4.5 GHz is thicker than 5 mm, which corresponds to $0.5\lambda_{\varepsilon_r}$.

An evolution of the design introducing a physical separation of exciting microstrip lines and feeding network has been demonstrated to reduce the impact of the asymmetric feed on the radiation pattern. The geometry and feeding mechanism of this antenna is extended to create a multi-function diversity DRA in the next chapter.

Chapter 4

Multifunction and diversity dielectric resonator antenna

THIS chapter extends the cross-shaped dielectric resonator antenna (DRA) to a multifunction device with separately fed broadside circularly polarized (CP) and omnidirectional linearly polarized (LP) radiation patterns. These distinct radiation patterns are achieved in overlapping frequency bands by exciting two different modes in a single dielectric resonator (DR) volume. This chapter also investigates the effect of the feeding geometry on the mutual coupling between the modes and concludes that an asymmetric feeding degrades the orthogonality of the modes and thus increases the inter-port coupling coefficient. By using a symmetric feeding, the coupling coefficient can be significantly reduced to below -30 dB in the frequency band common to both operation modes. The experimental results show a good agreement with simulation and demonstrate a broadside CP operation over a bandwidth of 6.8%, which overlaps with the omnidirectional LP impedance bandwidth of 38.5%. The proposed antenna could be used not only as multifunction but also as polarization diversity antenna due to the overlapping dual-feed CP and LP operation.

4.1 Introduction

The prevalence of wireless communication puts high demand on performance characteristics of highly integrated mobile wireless communication devices with versatile applications. Commonly, two or more antennas have to be employed in conventional multifunction or diversity schemes. It is a challenge to integrate such antennas into equipments taking into account space limitation, port-to-port isolation or mutual coupling effects with other elements.

Using a single antenna structure with low mutual power coupling between different ports is one of the solutions to enable multifunction or diversity schemes. The available literature mostly focuses on multi-ports printed diversity antenna or planar inverted-F antenna (PIFA), due to their compactness, low cost and low profile [12–15]. However, these antennas often have complicated structure, large size or relatively low gain.

In spite of the advantages of small size, high radiation efficiency and versatility in shape and feeding mechanism, the 3-D structure of dielectric resonator antennas (DRAs) offers an additional freedom in exciting various resonant modes in one antenna volume [6, 7]. These modes can be utilized for various requirements, which makes DRA a suitable potential candidate for multifunction applications. For example, a rectangular hollow dielectric resonator (DR) was designed as antenna and packaging cover [9]; ultrawideband operation was achieved by exciting the fundamental and higher-order modes in a hybrid DRA [17]; a cylindrical DRA was utilized as direction finder [18]; a cylindrical DR was used as filter and antenna [16]; a dual-band antenna with two different radiation patterns in two separate bands was achieved by using a cylindrical dielectric resonator (DR) [19].

In this chapter, we present a DRA with broadside circularly polarized (CP) and linearly polarized (LP) omnidirectional radiation patterns obtained by exciting two different modes within a cross-shaped DR. The proposed design is extended from the CP DRA in the Chapter 3, by adding a probe to produce a LP radiation pattern. The size of the DR is reduced by using thin plates of high-permittivity material, as successfully applied in a dual-mode bridge-shaped DRA [95] and for the CP DRA [20] discussed in detail in Chapter 3. In addition, a feeding with sequential rotation technique is utilized to increase the symmetry of the modes and reduce coupling between the two feeding ports. Compared with [19], the operation of two ports feeding a single antenna volume with different radiation characteristics is achieved at the same frequency, which results

in a multifunction, but also allows diversity. At the end of this chapter, the antenna diversity performance is evaluated by two commonly used criteria, envelope correlation coefficient and mean effective gain.

4.2 Multifunction DRA design

The multiple functions of the antenna are realized by introducing two ports exciting independent orthogonal modes in a cross-shaped DR volume. Circular polarization is achieved by exciting orthogonal TE_{111} modes in the two cross arms with 90° phase difference, similarly as utilized in designing a cross-shaped CP DRA in the Chapter 3. The LP omnidirectional radiation pattern is realized by exciting a monopole mode, denoted here as Quasi-TM_{111} mode in reference to the corresponding cylindrical resonator mode. The corresponding field distributions in one arm are sketched in Fig. 4.1.

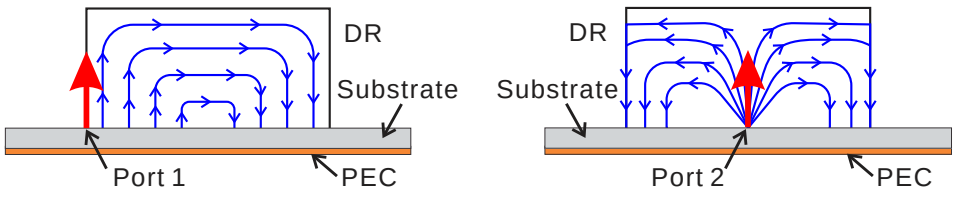

(a) TE_{111} mode (b) Quasi-TM_{111} mode

Figure 4.1. E-field distribution in one arm of the cross-shaped DR.

To excite these two modes, the design of the feeding networks is divided into three steps: (i) exciting quadrature TE_{111} modes from Port 1, (ii) exciting the Quasi-TM_{111} mode from Port 2, and (iii) integrating these two ports into a common volume. The DRA element and feeding network are simulated and optimized by using Ansoft® HFSS.

4.2.1 Antenna structure

The multifunction antenna design is based on the principle of the separation of feeding network and antenna, which are implemented on both side of the ground plane, as proposed in the Chapter 3. The antenna structure is adapted from the improved CP DRA

design in Fig. 3.10. A cross-shaped DR is mounted on a Rogers® substrate with back-side metallization, as shown in Fig. 4.2. The square substrate has a relative dielectric permittivity of 2.5, side length of 90 mm and thickness of 1.524 mm. The cross-shaped DR is composed of two notched rectangular slices cut from the same dielectric plate, as used in the previous design in Chapter 3. The thickness and relative permittivity of the dielectric plate are 1 mm and 50, respectively. In each slice, a narrow notch with a width equal to the plate width d_0 is cut, as shown in the inset of Fig. 4.2, to create a mechanically stable cross. The wider notch provides room for a central probe feed to excite Quasi-TM_{111} mode. The introduction of the notch in the DR does not influence markedly the TE_{111} mode, which has a zero E-field in the centre. The width w_0 and height h_1 of the notch are optimized for better coupling from the probe to the DR in the Section 4.2.6. The detailed design procedures of a similar DR for a 4.5 GHz CP antenna can be found in the Chapter 3. The dimensions of the resonator arms, including the notch, are listed in first three lines of Table 4.1.

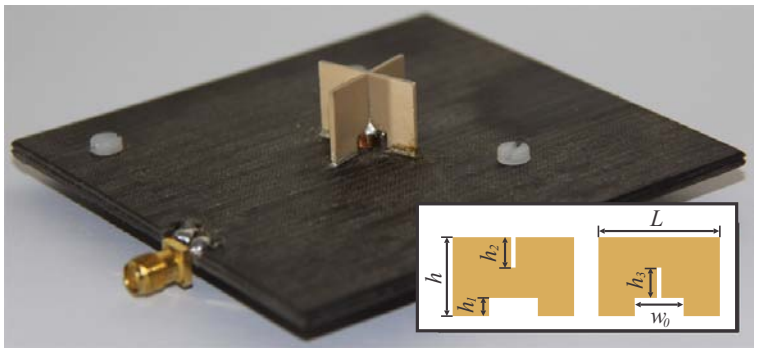

Figure 4.2. Realized prototype of the dual-port cross-shaped DRA. Inset: Notched rectangular dielectric plates forming the cross-shaped DR.

4.2.2 Excitation of the TE_{111} mode from Port 1

An initial feeding network design for the CP operation is derived from the concept proposed in the Chapter 3. For the sake of convenience, it is briefly described in this paragraph. Orthogonal TE_{111} modes are excited in quadrature in the two equal-length dielectric cross arms. This is realized through microstrip lines with a 90° delay line on one of the branches. This feeding network introduces however an asymmetry in the geometry which degrades the symmetry of the TE_{111} modes. This in turn translates into asymmetric radiation patterns and the useable angle around broadside where circular polarization is maintained is consequently reduced to less than 30°. To overcome these

negative effects, a physical separation is first introduced in the form of a ground plane between the DR and its feeding network, as shown in Fig. 4.3. On the top substrate, the last segments of the feeding microstrip lines are patterned with a width 1 mm to fit under the DR cross. Vias of diameter 1 mm are utilized to connect microstrip lines of width 1 mm on the bottom of the substrate through holes in the ground plane and substrates, as shown in Fig. 4.3(c). The metal around the via and probe holes is removed to avoid any contact between pin and ground. The diameters of the clearance around the via and probe holes are 2 and 3 mm, respectively. The T-junction and the arc-shaped microstrip feeding line are located on the bottom of the lower substrate to reduce their impact on the radiation pattern. The width w of the arc-shaped microstrip and the length L_0 of the microstrip line on top of the substrate are optimized simultaneously for best impedance matching. A simulated impedance bandwidth ($|S_{11}|$ < -10 dB) of 20% is achieved with w = 0.5 mm and L_0 = 6 mm. Given the total DR length of 20 mm, the length of the notch is selected as 8 mm to provide maximum space for the centre probe.

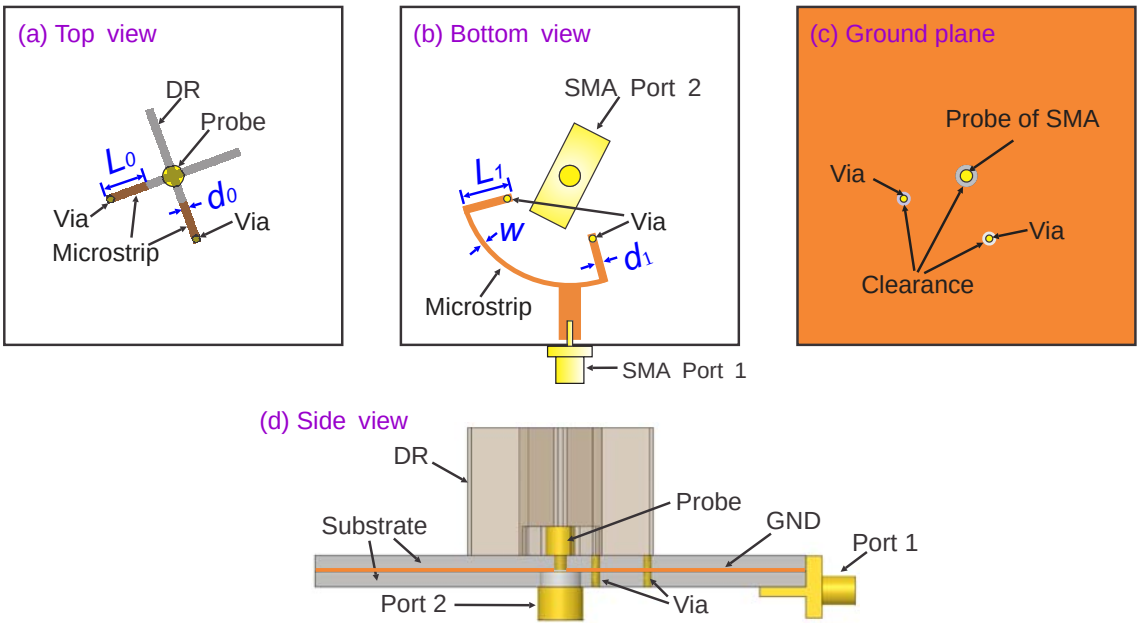

Figure 4.3. Top, bottom, ground plane, and side view of the cross-shaped DRA using one-side feeding.

4.2.3 Excitation of the Quasi-TM$_{111}$ mode from Port 2

The Quasi-TM$_{111}$ mode is excited through a widened centre probe of an SMA connector located in the centre of the cross, as shown in Fig. 4.5. As mentioned before, the

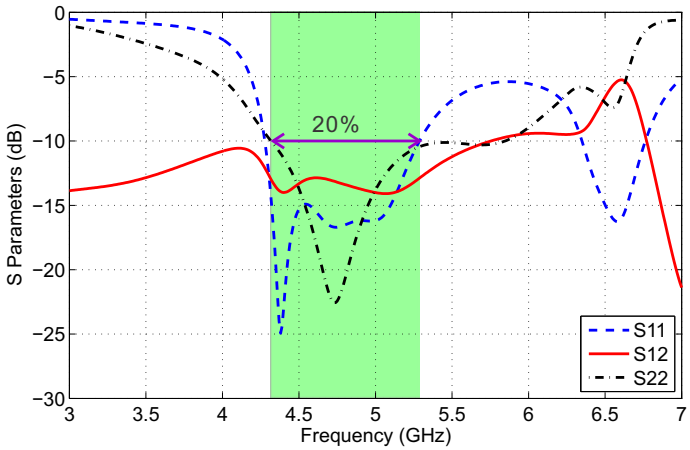

Figure 4.4. Simulated S parameters of the cross-shaped DR using one-side feeding. The shaded area shows the overlapping impedance band.

bottom of the dielectric cross is cut to provide room for this centre probe. Due to the high permittivity of the DR, the probe has to touch the DR to achieve efficient excitation of the Quasi-TM_{111} mode. Thus, the centre probe height is equal to the notch height. For the same reason, the diameter of the probe (above the substrate part) is increased to improve coupling between probe and DR in the simulation. This allows also to shorten the probe by increasing the top capacitance and increase the impedance bandwidth. The height and diameter of the central probe are further optimized for better coupling from the probe to the DR and wider impedance bandwidth of Port 2, as described later in Section 4.2.6.

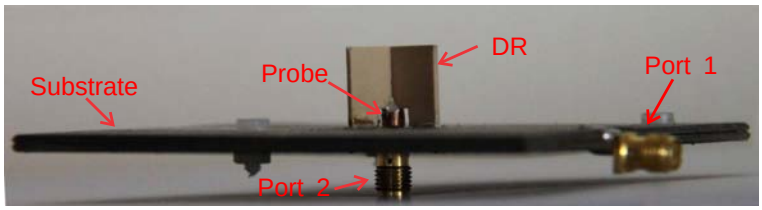

Figure 4.5. Side view of the proposed multifunction cross-shaped DRA.

4.2.4 Integrating two ports into a common volume

The coupling between pure TE_{111} and Quasi-TM_{111} modes is theoretically zero due to the orthogonal field distribution of these two modes. However, the symmetric field distribution is disturbed when a microstrip line is used to excite TE_{111} from one-side. Figure 4.6 (a) and (b) illustrate the simulated field distribution while exciting one port

and terminating the other port with a matched load. It can be observed that both TE_{111} and Quasi-TM_{111} mode are significantly disturbed due to the existence of the feeding microstrip line underneath the resonator. The asymmetric field distribution is the source of mutual coupling between the two ports. A simulated overlapping impedance bandwidth of Port 1 and 2 of 20% can be achieved, as shown in Fig. 4.4. However, the simulated coupling coefficient is higher than -15 dB in the band of operation, which is not acceptable in diversity systems.

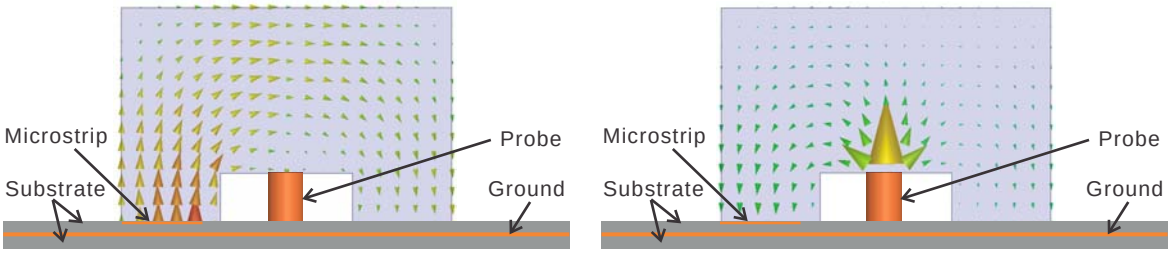

(a) TE_{111} mode excited from Port 1 (Microstrip).

(b) Quasi-TM_{111} mode excited from Port 2 (Probe).

Figure 4.6. Simulated E-field distribution of TE_{111} and Quasi-TM_{111} mode at 4.7 GHz in one rectangular arm of the cross-shaped DR using one-side feeding lines.

Mutual coupling reduction: Parallelogrammatic DR

Due to the effect of the microstrip feeding line, the magnitude of the E-field located in left side of the DR is larger than that in right side of the DR, for both modes of operation. Therefore, an asymmetric structure is introduced to compensate this imbalance by increasing the DR volume on the left side and conversely decrease it on the right side. A parallelogrammatic DR is used to validate this concept. Figure 4.7 sketches the simulated TE_{111} and Quasi-TM_{111} field distribution in one parallelogrammatic arm of the cross-shaped DR, which is shown in the insert. The parallelogrammatic DR has the same height and length of top and bottom sides as the rectangular DR. Through the optimization of the angular parameter α, the mutual coupling between the two ports is reduced to below -15 dB, which is generally accepted for practical diversity applications. This is achieved at the cost of slight decrease in the common impedance bandwidth of Port 1 and 2, as shown in Fig. 4.8.

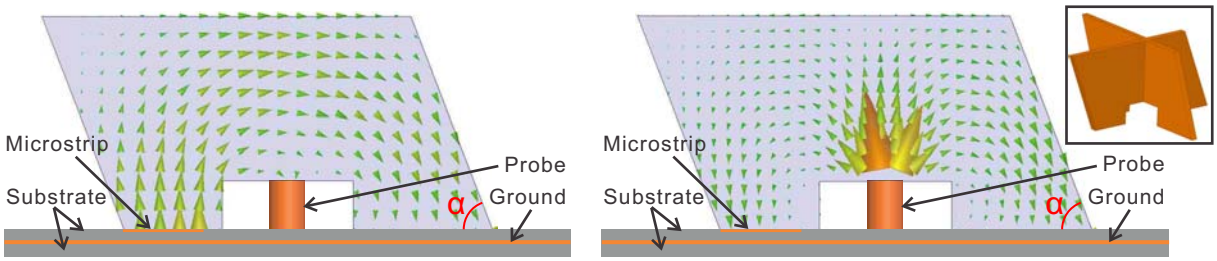

(a) TE_{111} mode excited from Port 1.

(b) Quasi-TM_{111} mode excited from Port 2.

Figure 4.7. Simulated E-field distribution of TE_{111} and Quasi-TM_{111} mode at 4.7 GHz in one parallelogrammatic arm of the cross-shaped DR using one-side feeding lines. Inset: Cross-shaped DR composed of two parallelogrammatic arms.

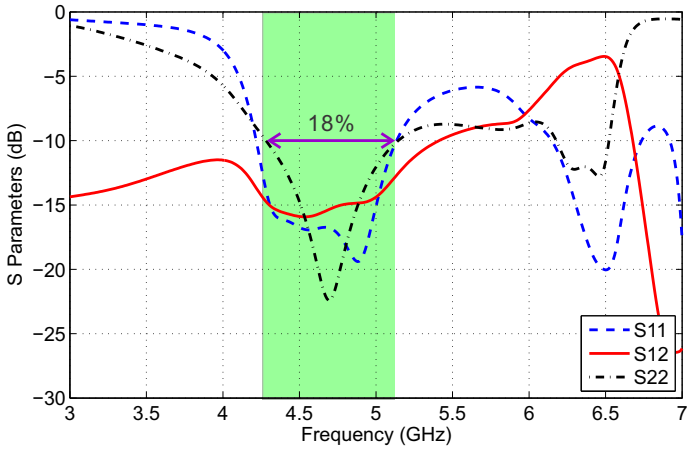

Figure 4.8. Simulated S parameters of the cross-shaped DR composed by two parallelogrammatic arms using one-side feeding. The shaded area shows the overlapping impedance band.

Mutual coupling reduction: Symmetric feeding

Since the asymmetric field distribution results from the asymmetric feeding, a symmetric feeding method is proposed next to reduce its impact on the ideal field distribution. The rectangular DR is excited by two microstrip lines located on each side and driven with 180° phase difference. With these symmetric feeding lines, both TE_{111} and Quasi-TM_{111} field are symmetrically distributed, as shown in Fig. 4.9, and the simulation result demonstrates a significant reduction of coupling. The simulated mutual coupling is reduced to less than -30 dB in the operation band, as shown in Fig. 4.10. The negative effect is the increased complexity of the feeding network and reduction of the impedance bandwidth of Port 1.

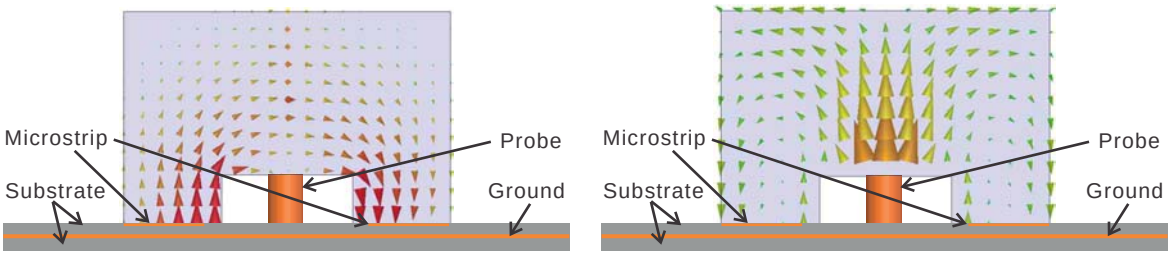

(a) TE_{111} mode excited from Port 1. (b) Quasi-TM_{111} mode excited from Port 2.

Figure 4.9. Simulated E-field distribution of TE_{111} and Quasi-TM_{111} mode at 4.7 GHz in one rectangular arm of the cross-shaped DR using two-side feeding.

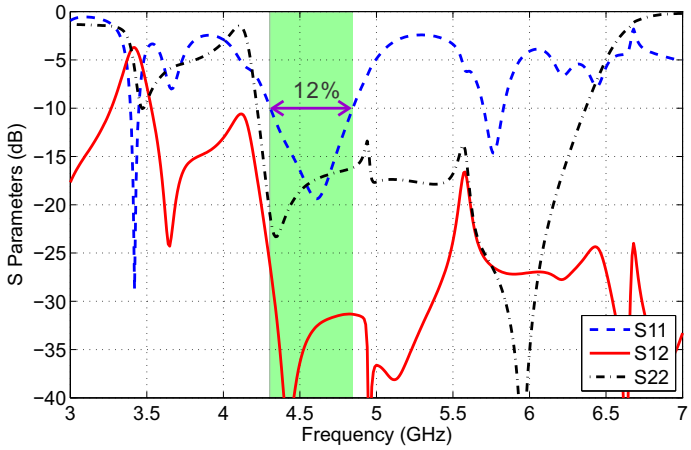

Figure 4.10. Simulated S parameters of the cross-shaped DR using two side feeding. The shaded area shows the overlapping impedance band.

4.2.5 Feeding network of Port 1 for broadside circular polarization

For the practical realization of the symmetric feeding scheme, a sequential rotation technique, which is a commonly used feeding method in array [96], is employed to connect the feeding lines on the top of substrate. The feed network is modified so that the DR is fed by four feeding points with progressive 90° phase shift. The phase distribution is achieved with properly designed delay lines, as shown in Fig. 4.11.

The feeding network is straightforwardly adapted from the one-side feeding design in Fig 4.3. The parameters of microstrip lines on the top of substrate, vias and two arc-shaped microstrip lines on the bottom of substrate in Fig. 4.11 have the same dimensions as the corresponding structures in Fig. 4.3. A bended microstrip of width 1 mm is utilized to connect the two arc-shaped microstrip lines, located on the left and right. Further, the bended microstrip line is connected to a 50 Ω transmission line from

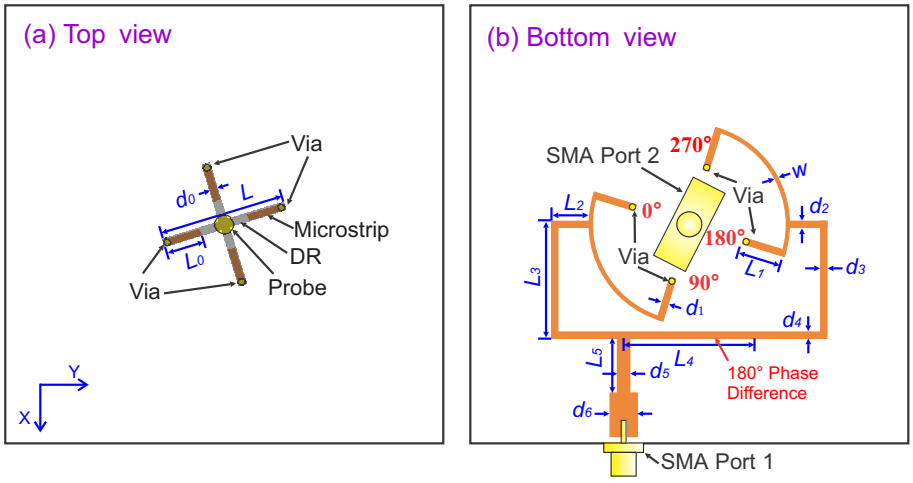

Figure 4.11. Top, side and bottom view of the feeding network for the proposed antenna.

Table 4.1. Antenna parameters of the Multifunction and diversity DRA

Symbol	Value (mm)	Symbol	Value (mm)	Symbol	Value (mm)
L	20	h	13	h_1	3
h_2	5	h_3	5	w_0	8
d_0	1	L_0	6	L_1	7
d_1	1	L_2	16	d_2	1
L_3	25	d_3	1	L_4	21
d_4	1	L_5	11.2	d_5	2
d_6	4.35	w	0.5		

the SMA connector (Port 1) through a quarter-wave transformer (with length L_5 and width d_5). The quarter-wave transformer is optimized for best impedance matching. All parameters of the feeding network are listed in Table 4.1.

4.2.6 Impedance bandwidth optimization of Port 2

The impedance bandwidth of Port 2 is enlarged by optimizing the centre probe diameter and height. The change of the probe diameter has little effect on the Port 1 and mutual coupling between these two ports, as shown in Fig. 4.12, because the TE_{111} mode has a zero E-field in the centre. The maximum bandwidth is obtained when the probe diameter is equal to 3 mm. Figure 4.13(c) shows that the bandwidth of Port 2 can be further enlarged by increasing the probe height, which is equal to the notch height

h_1. However, the influence of notch on the TE_{111} mode field distribution cannot be neglected when the notch height is equal to 4 mm. A high notch decreases the impedance of Port 1, as shown in Fig. 4.13(a).

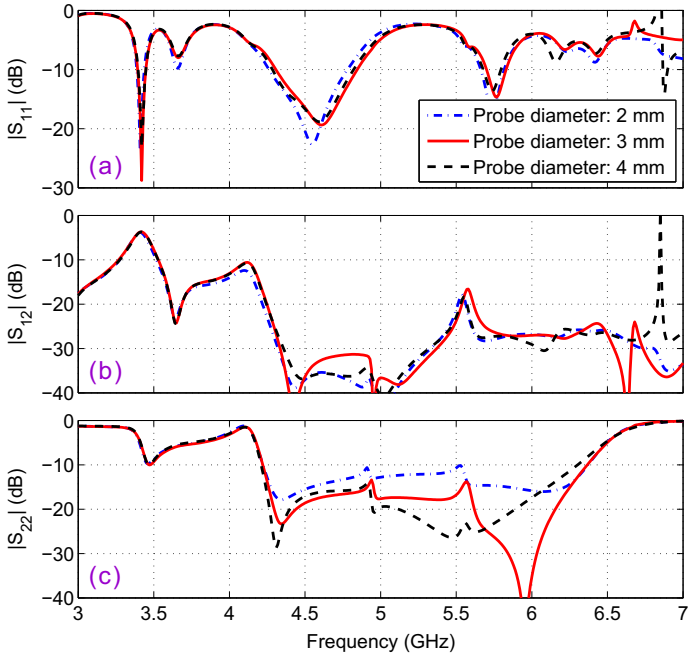

Figure 4.12. Simulated S parameters of different values of centre probe diameter.

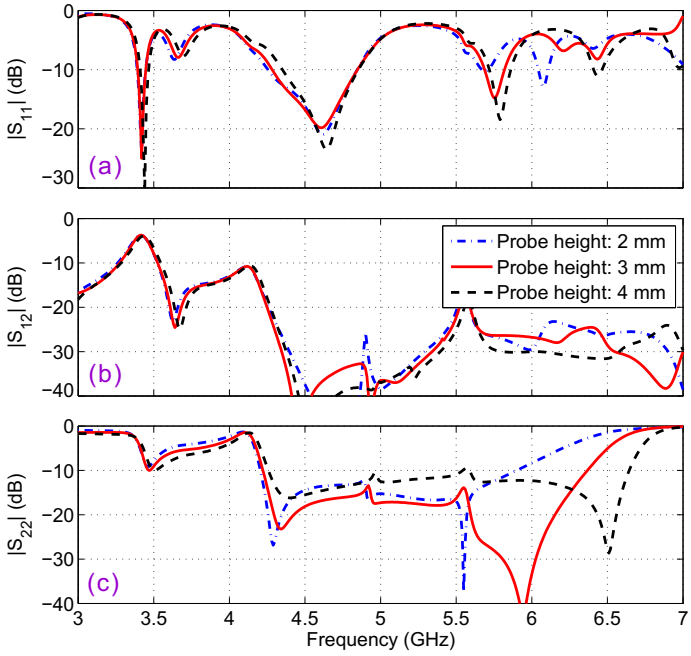

Figure 4.13. Simulated S parameters of different values of centre probe height.

With the probe diameter of 3 mm and height of 3 mm, the simulated impedance bandwidth of Port 2 is increased to 38.5%, overlapping with the impedance bandwidth of Port 1. The simulated E-field distribution at 5.5 and 6 GHz in one rectangular arm of the cross-shaped DR confirms the excitation of the Quasi-TM_{111} mode also in the higher frequency part of the impedance bandwidth, as shown in Fig. 4.14.

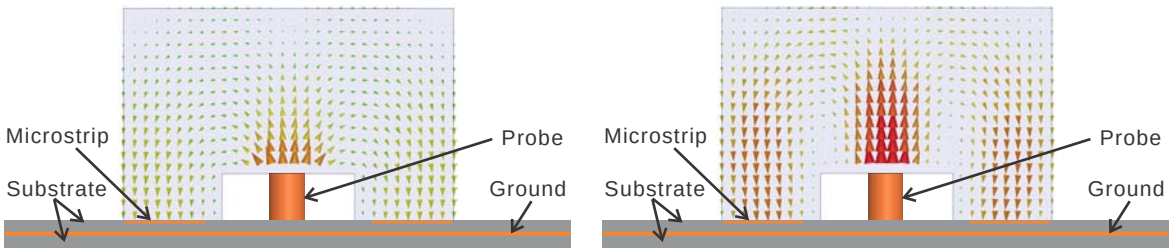

(a) 5.5 GHz (b) 6 GHz

Figure 4.14. Simulated E-field distribution of Quasi-TM_{111} mode in one rectangular arm of the cross-shaped DR using two-side feeding.

4.3 Antenna performance

The prototype of the designed multifunction and diversity cross-shaped DRA with symmetric feeding is measured in the anechoic chamber. The measurement results are presented in this section.

4.3.1 S parameters

The simulated and measured reflection and coupling coefficients for the dual feed antenna are shown in Fig. 4.15. The Port 1 excites the TE_{111} modes and presents an impedance bandwidth (defined for $|S_{11}| <$ -10 dB) of 13.5%, whereas the Port 2 excites the Quasi-TM_{111} mode with a 38.5% impedance bandwidth. The simulated and measured coupling coefficient demonstrates a significant reduction of coupling between these two modes as a result of using a sequential symmetrical feeding. With the symmetric feeding, the coupling coefficient is below -25 dB in the overlapping CP and LP bandwidth. A small offset between simulation and measurement is attributed to fabrication imperfections.

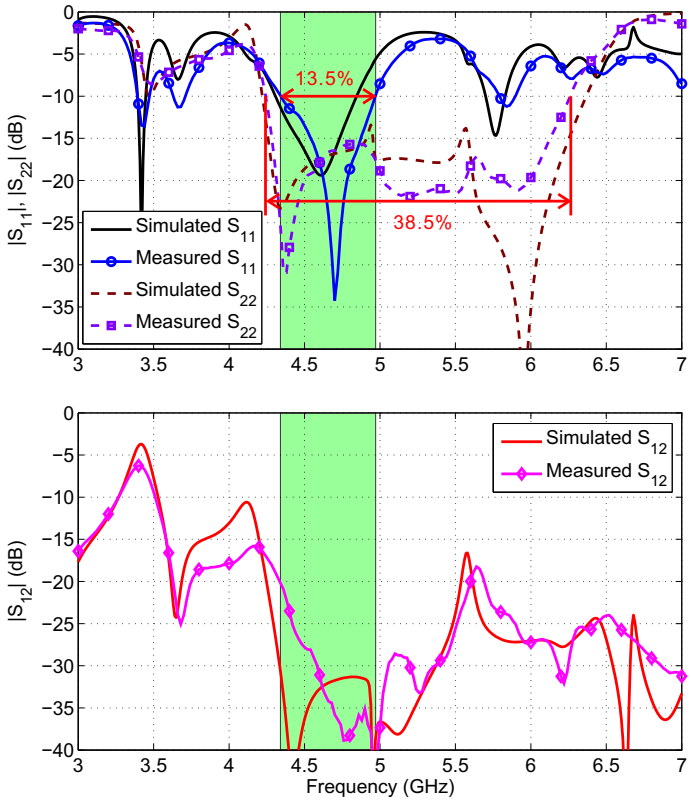

Figure 4.15. Simulated and measured antenna reflection and coupling coefficient for Port 1 (TE_{111} mode) and Port 2 (Quasi-TM_{111} mode). The shaded area shows the usable overlapping impedance band.

4.3.2 Axial ratio

The AR of the circular polarized mode (Port 1) is measured and calculated according to the third definition of Ludwig [93]. Fig. 4.16 shows a comparison between simulated and measured AR in broadside direction ($\theta = 0°$). The 3-dB AR bandwidth extends from 4.52 to 4.84 GHz, which yields an overlap with the impedance bandwidth of 6.8%. The frequency shift by 0.06 GHz to higher frequency is again attributed to fabrication imperfection. Over the CP bandwidth, the coupling coefficient between the two ports (Fig. 4.15) is below -30 dB. It is worth to mention that the impedance and CP bandwidth might possibly be further increased by using an hybrid-ring feeding network [97] or operating the antenna in a sequentially-fed 2x2 sub-array [96, 97] for high-gain applications.

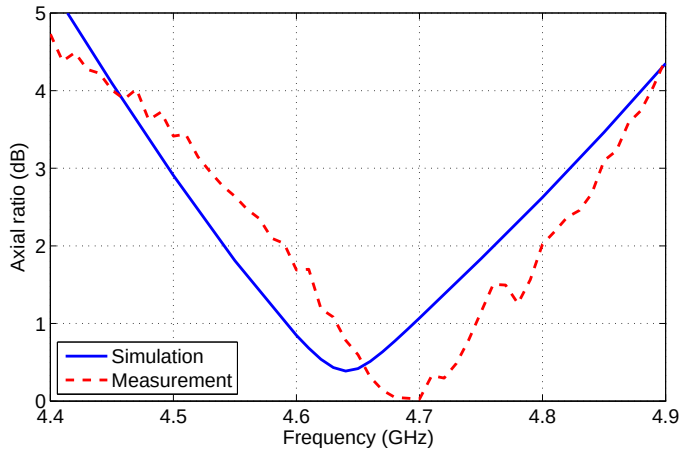

Figure 4.16. Simulated and measured axial ratio of Port 1.

4.3.3 Radiation patterns and gain

The circular and linear polarization radiation patterns have been measured in the respective bands of the two ports. For the Port 1, broadside patterns with left-hand CP (LHCP) radiation patterns are obtained in both XZ and YZ planes, as shown in Fig. 6.14. Sample patterns are shown here for 4.52, 4.69 and 4.84 GHz, i.e. in the left, centre, and right of the AR band. The LHCP fields are at least 15 dB higher than right-hand CP (RHCP) fields in the broadside direction. The angle off broadside, where CP is achieved, extends to more than 60° with reasonably rotationally symmetric radiation pattern.

The sample radiation patterns of Port 2 are shown at the same frequencies as Port 1 in Fig. 6.15. The ommnidirectional Quasi-TM_{111} radiating mode yields a vertically polarized monopole-type radiation patterns. In Fig. 4.19, two other radiation patterns at 5.5 and 6 GHz are also plotted to illustrate the stable radiation pattern over the higher frequency range of the impedance bandwidth of Port 2. The simulated and measured cross-polarization levels are at least 20 dB lower than co-polarization levels.

Figure 4.20 shows the simulated and measured gain for operation in both ports. In the operation bandwidth, the gain of the Port 1 (circularly polarization) at broadside direction is in the range of 2.3-4.3 dB. The maximum gain of the Port 2 (linear polarization) at XY plane is above -0.5 dB. The two peaks of Port 2 gain at 4.93 and 5.54 GHz result from the coupling between the notch and probe. The peaks can also be observed at the same frequencies in S-parameter of Port 2 in Fig. 4.15. The simulated 3D patterns

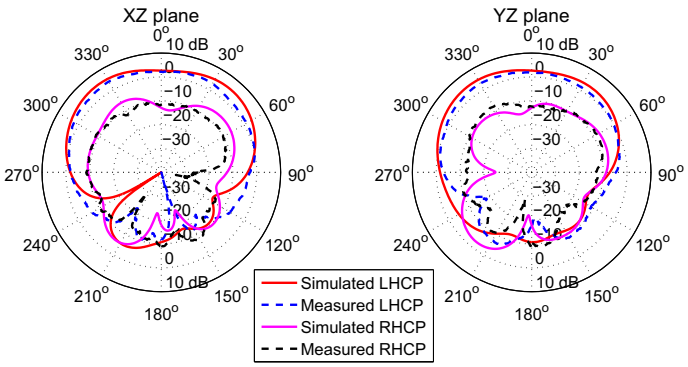

(a) Radiation pattern at 4.52 GHz

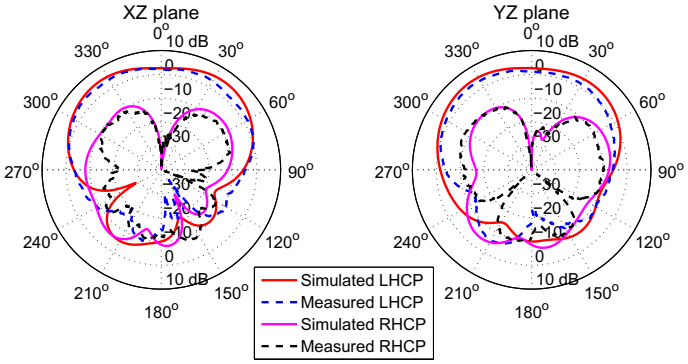

(b) Radiation pattern at 4.70 GHz

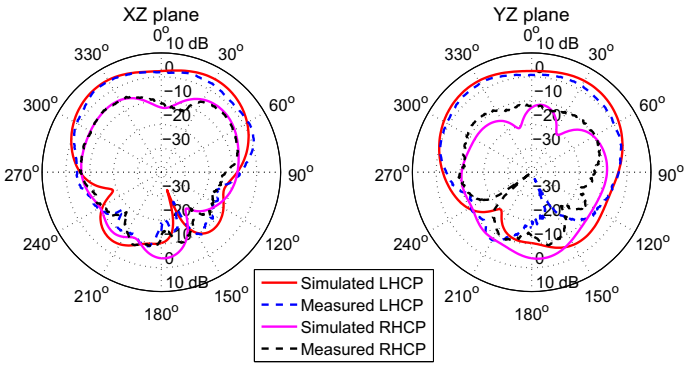

(c) Radiation pattern at 4.84 GHz

Figure 4.17. Simulated and measured circularly polarized radiation patterns of Port 1 at 4.52, 4.70 and 4.84 GHz.

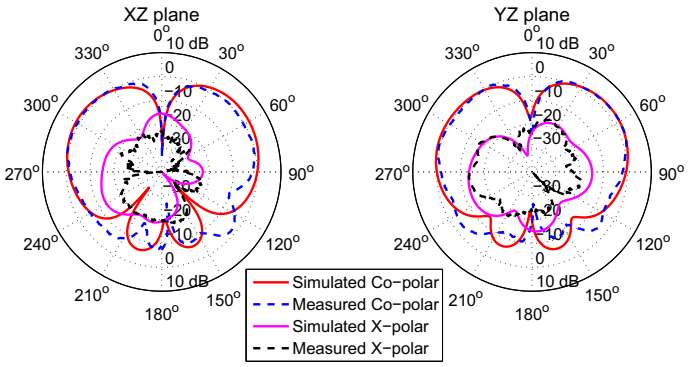

(a) Radiation pattern at 4.52 GHz

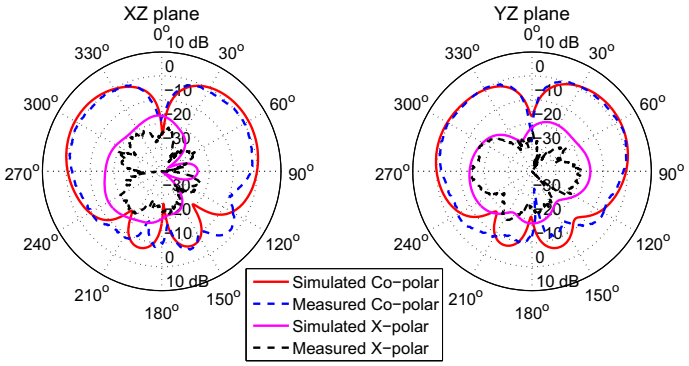

(b) Radiation pattern at 4.70 GHz

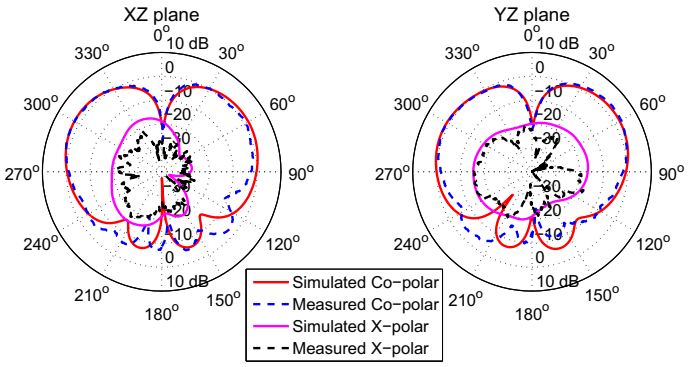

(c) Radiation pattern at 4.84 GHz

Figure 4.18. Simulated and measured linearly polarized radiation patterns of Port 2 at 4.52, 4.70 and 4.84 GHz.

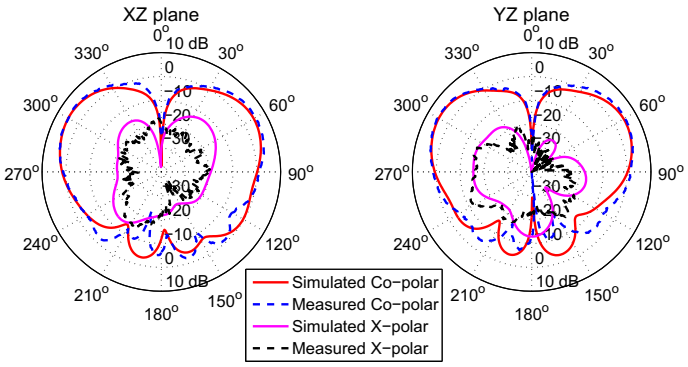

(a) Radiation pattern at 5.5 GHz

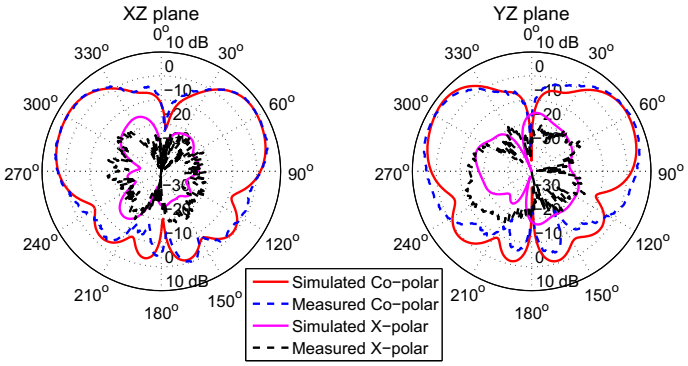

(b) Radiation pattern at 6 GHz

Figure 4.19. Simulated and measured linearly polarized radiation patterns of Port 2 at 5.5 and 6 GHz.

at these two frequencies are shown in Fig. 4.21. Although the coupling reduces the symmetry of the radiation patterns, reasonably omnidirectional radiation patterns can still be obtained at 4.93 and 5.54 GHz.

4.3.4 Diversity

The proposed antenna could also be used as diversity antenna due to the wide bandwidth overlap of the omnidirectional LP and broadside CP patterns. Two commonly used benchmarks, i.e. the mean effective gain (MEG) and the envelope correlation coefficient (ECC), are utilized to evaluate the antenna diversity performance.

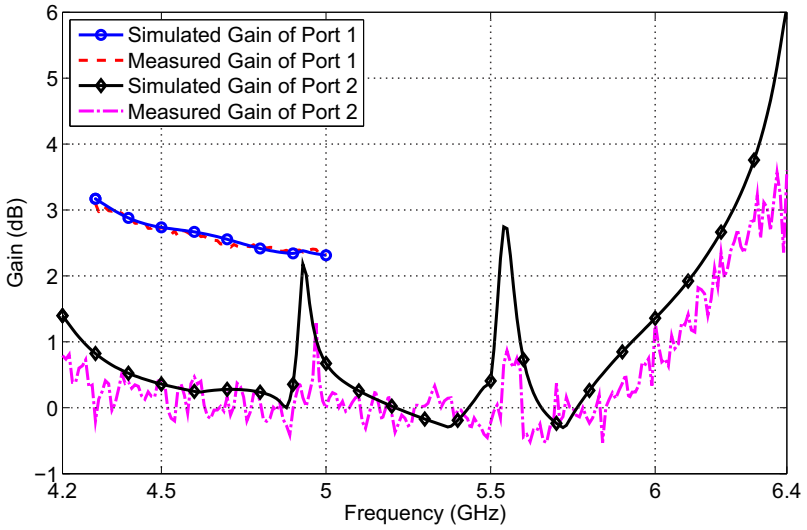

Figure 4.20. Simulated and measured gain of Port 1 and 2. The gain of Port 1 is the broadside direction. The gain of Port 2 shows the maximum gain at XY plane.

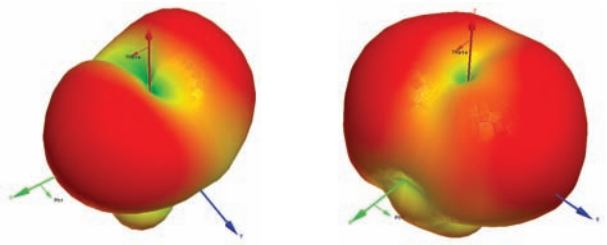

(a) 4.93 GHz (b) 5.54 GHz

Figure 4.21. Simulated 3D radiation patterns at 4.93 and 5.54 GHz.

Mean effective gain

In multipath fading environments, the MEG is typically employed to characterize the performance of a diversity antenna. The MEG (G_{MEG}) is defined as [98]

$$G_{\mathrm{MEG}} = \frac{P_{\mathrm{rec}}}{P_v + P_h} \ , \tag{4.1}$$

where P_{rec} is the mean received power of the antenna over the random route; P_v and P_h are the mean incident powers of the vertically polarized and horizontally polarized components of incident waves. The cross-polarization power ratio (XPR) is denoted by

$$R_{\mathrm{XPR}} = \frac{P_v}{P_h}. \tag{4.2}$$

In spherical coordinates $\Omega = (\theta, \phi)$, the θ and ϕ components, respectively, correspond to the vertically polarized and horizontally polarized components if the antenna is located in the XY plane.

The mean received power P_{rec} of the antenna is given by [94]

$$P_{\text{rec}} = \int_0^{2\pi} \int_0^{\pi} \left\{ P_1 G_\theta(\Omega) P_\theta(\Omega) + P_2 G_\phi(\Omega) P_\phi(\Omega) \right\} \sin\theta \, d\theta \, d\phi, \tag{4.3}$$

where $G_\theta(\Omega)$ and $P_\theta(\Omega)$ are the θ components of the antenna gain and the angular power density functions of the incoming plane waves, respectively; $G_\phi(\Omega)$ and $P_\phi(\Omega)$ are the ϕ components of the antenna gain and the angular power density functions of the incoming plane waves, respectively. Here, P_1 and P_2 are mean received powers that would be received by a vertically polarized and horizontally polarized isotropic antenna, respectively. The ratio of P_1 and P_2 is equal to R_{XPR}.

By combining Eq. (4.3) and the definition of the XPR (4.2) into Eq. (4.1), the MEG is rearranged as

$$G_{\text{MEG}} = \int_0^{2\pi} \int_0^{\pi} \left\{ \frac{R_{\text{XPR}}}{1+R_{\text{XPR}}} G_\theta(\Omega) P_\theta(\Omega) + \frac{R_{\text{XPR}}}{1+R_{\text{XPR}}} G_\phi(\Omega) P_\phi(\Omega) \right\} \sin\theta \, d\theta \, d\phi. \tag{4.4}$$

However, the determination of the MEG from Eq. (4.4) requires a large number of measurements as it is based on 3D patterns, which have to be sampled with a reasonably fine resolution. In the free space, the MEG is approximately equal to half the total radiation efficiency η_{rad} [99], i.e.,

$$G_{\text{MEG}} = \frac{1}{2} \eta_{\text{rad}}. \tag{4.5}$$

In this case, the antenna performance is mostly determined by the total radiation efficiency instead of the shape of the radiation pattern or the realized gain [98]. The total radiation efficiency η_{rad} can be defined as the ratio of the total radiated power P_{rad} and the maximum available power that can be delivered from the generator P_{in}. Thus, for a M-port lossless antenna, the MEG for Port i can be approximately calculated by [99],

$$G_{\text{MEG}_\text{i}} = \frac{1}{2} \left(1 - \sum_{k=1}^{M} \mid S_{ik} \mid^2 \right). \tag{4.6}$$

Equation (4.6) offers a simple and fast way to calculated MEG from S parameters with moderate accuracy.

For multiport antennas, all ports need to have a MEG that is approximately equal and as high as possible. For 100% radiation efficiency, the term $\sum_{k=1}^{M} \mid S_{ik} \mid^2$ in Eq. (4.6) is close to 0 and thus the MEG will be -3 dB. The MEG should be above -10 dB for better diversity performance [100]. The simulated and measured results of MEG are shown in Fig. 4.22. The MEG of Port 1 and 2 are both between -3.1 and -4.5 dB in the overlapping bandwidth.

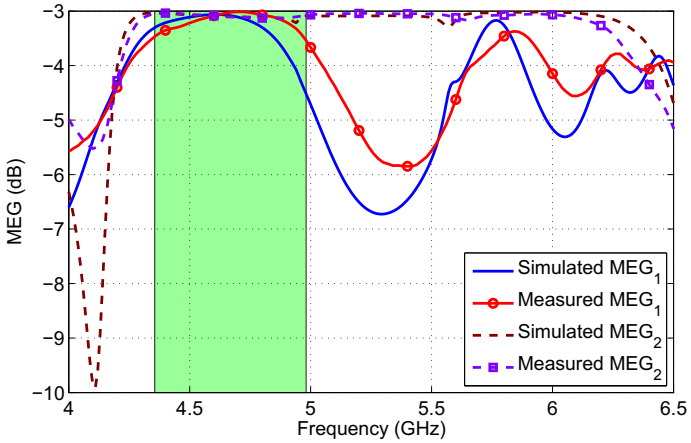

Figure 4.22. Simulated and measured mean effective gain.. The shaded area shows the usable overlapping impedance band.

The difference of MEG between the ports may lead to a branch power imbalance and deteriorate the performance. The ratio of MEG of Port i and k is defined as

$$R_{\mathrm{MEG_{ik}}} = \frac{G_{\mathrm{MEG_i}}}{G_{\mathrm{MEG_k}}}. \tag{4.7}$$

The simulated and measured MEG difference between Port 1 and 2 is less than 1.5 dB, as shown in Fig. 4.23.

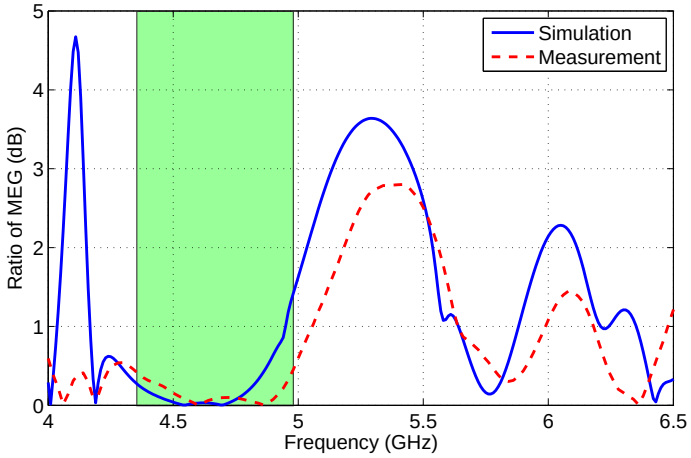

Figure 4.23. Simulated and measured ratio of mean effective gain of Port 1 and 2. The shaded area shows the usable overlapping impedance band.

Envelope correlation coefficient

The envelope correlation coefficient (ECC) ρ_e is another one of the important parameters for a diversity antenna. It measures the degree of similarity between the beam

patterns for the different antenna ports. Low ECC means high diversity gain and a criteria $\rho_e < 0.5$ is commonly regarded as acceptable. In the general case, the ECC depends on the propagation environment and the far field radiation pattern of the antenna. In spherical coordinates $\Omega = (\theta, \phi)$, the ECC of a two ports antenna can be expressed as [101]:

$$\rho_e = \frac{|\int_0^{2\pi}\int_0^{\pi}[\vec{F}_1(\Omega)\cdot\vec{F}_2(\Omega)]\,d\Omega\,|^2}{\int_0^{2\pi}\int_0^{\pi}|\,\vec{F}_1(\Omega)\,|^2\,d\Omega\,\int_0^{2\pi}\int_0^{\pi}|\,\vec{F}_2(\Omega)\,|^2\,d\Omega}, \tag{4.8}$$

where $\vec{F}_i$ is the field radiation pattern when the Port i is excited (i=1, 2); "$\cdot$" denotes the Hermitian product; and $d\Omega = \sin\theta\, d\theta\, d\varphi$.

Similarly to the computation of the MEG from 3D patterns, the determination of the ECC is a time-consuming process whether it is done numerically or experimentally. To solve the problem, Blanch et al. [102] proposed a method to calculate ECC from the S-parameter characterisation of a two-antenna diversity system. The method has been further validated for calculating ECC of multiport antennas [103–105].

Considering a two-port diversity antenna, the total radiated electric field at an arbitrary point (r, θ, ϕ) in the far field region is the sum of the radiated electric field $\vec{E}_1$ from Port 1 and $\vec{E}_2$ from Port 2 [102],

$$\begin{aligned}\vec{E} &= \vec{E}_1 + \vec{E}_2 \\ &= \left(\alpha_1\sqrt{\frac{D_1}{4\pi}}\vec{F}_1(\Omega) + \alpha_2\sqrt{\frac{D_2}{4\pi}}\vec{F}_2(\Omega)\right)\frac{\sqrt{\eta_0}e^{-jkr}}{r},\end{aligned} \tag{4.9}$$

where α_i is the incident wave amplitude from Port i; D_i is the maximum directivity of Port i; and η_0 and k are the free-space wave impedance and wave number, respectively. The total power radiated by the antenna can be calculated by integrating the power density over the whole space

$$\begin{aligned}P_{\text{total}} &= \frac{1}{\eta_0}\int_0^{2\pi}\int_0^{\pi}|\vec{E}_i|^2 dS \\ &= \frac{1}{\eta_0}\int_0^{2\pi}\int_0^{\pi}\left(|\vec{E}_1|^2 + |\vec{E}_2|^2 + \vec{E}_1\cdot\vec{E}_2 + \vec{E}_2\cdot\vec{E}_1\right)dS \\ &= A_{11}|\alpha_1|^2 + A_{22}|\alpha_2|^2 + A_{12}\alpha_1\alpha_2^* + A_{21}\alpha_2\alpha_1^*,\end{aligned} \tag{4.10}$$

denoting

$$\begin{aligned}A_{ii} &= \frac{D_i}{4\pi}\int_0^{2\pi}\int_0^{\pi}|\vec{F}_i(\Omega)|^2 d\Omega \\ A_{il} &= \frac{\sqrt{D_i D_l}}{4\pi}\int_0^{2\pi}\int_0^{\pi}[\vec{F}_i(\Omega)\cdot\vec{F}_l(\Omega)]d\Omega,\end{aligned} \tag{4.11}$$

where i, l = 1 or 2 and $d\Omega = dS/r^2$. Since A_{il} is equal to A_{li}^* (based on the definition of the scalar product), the compact form of Eq. (4.10) is given as

$$P_{\text{total}} = \boldsymbol{\alpha}^{\dagger} \boldsymbol{A}\, \boldsymbol{\alpha}, \tag{4.12}$$

where $\boldsymbol{\alpha} = [\alpha_1\ \alpha_2]$; $\boldsymbol{A} = \begin{bmatrix} A_{11} & A_{12} \\ A_{21} & A_{22} \end{bmatrix}$; the symbol '†' indicates the Hermitian transpose operation.

According to the S-parameter theory, the total radiated power is presented by

$$P_{\text{total}} = \boldsymbol{\alpha}^{\dagger}(\boldsymbol{I} - \boldsymbol{S}^{\dagger}\boldsymbol{S})\, \boldsymbol{\alpha}, \tag{4.13}$$

being $\boldsymbol{I}$ the identity matrix and $\boldsymbol{S}$ the S-parameters matrix. Comparing Eq. (4.12) and (4.13), we can directly see that $\boldsymbol{A} = \boldsymbol{I} - \boldsymbol{S}^{\dagger}\boldsymbol{S}$. The equivalent equations are presented by

$$\begin{aligned} \frac{D_1}{4\pi}\int_0^{2\pi}\int_0^{\pi} |\vec{F}_1(\Omega)|^2 d\Omega &= 1 - (|S_{11}|^2 + |S_{21}|^2) \\ \frac{D_2}{4\pi}\int_0^{2\pi}\int_0^{\pi} |\vec{F}_2(\Omega)|^2 d\Omega &= 1 - (|S_{22}|^2 + |S_{12}|^2) \\ \frac{\sqrt{D_1 D_2}}{4\pi}\int_0^{2\pi}\int_0^{\pi} [\vec{F}_1(\Omega)\cdot\vec{F}_2(\Omega)] d\Omega &= -(S_{11}^* S_{12} + S_{21}^* S_{22}). \end{aligned} \tag{4.14}$$

Substituting Eq. (4.14) into Eq. (4.24), a more convenient expression to calculate ECC from the S parameters is given by

$$\rho_e = \frac{|\ S_{11}^* S_{12} + S_{21}^* S_{22}\ |^2}{(1 - |S_{11}|^2 - |S_{21}|^2)\ (1 - |S_{22}|^2 - |S_{12}|^2)}. \tag{4.15}$$

The simulated and measured S-parameters of the proposed multifunction DRA are utilized to calculate the ECC by using Eq. (4.15). The simulated and measured ECC, given in Fig. 4.24, demonstrate the low correlation coefficients between the two ports in the overlapping bandwidth. This low ECC indicates little overlapping between radiation patterns of these two ports. Consequently, the incoming signal from any direction will be predominantly received by one port. As a consequence, the proposed antenna will be more robust than using a single omnidirectional antenna.

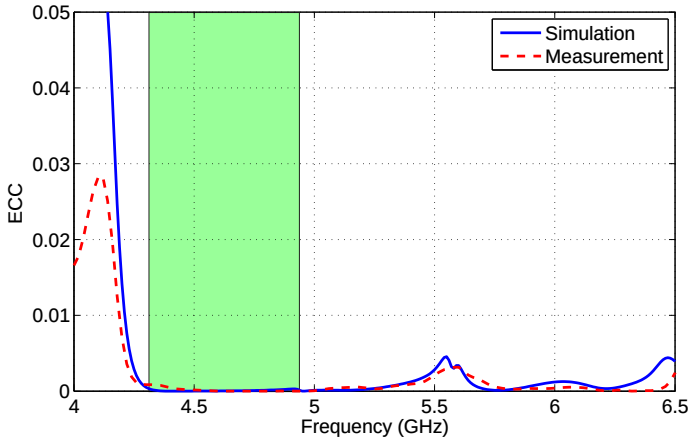

Figure 4.24. Simulated and measured envelope correlation coefficients. The shaded area shows the usable overlapping impedance band.

4.4 Conclusion

This chapter has proposed a cross-shaped DRA for multifunction or diversity applications. A broadside CP and an omnidirectional LP patterns are radiated in overlapping frequency bands by exciting TE_{111} and Quasi-TM_{111} modes in a single cross-shaped DR. The coupling between these two modes is theoretically zero due to their orthogonal field distribution. However, the asymmetric feeding method can disturb the field distribution in the DR and thus increase the mutual coupling between these two modes. The asymmetric field distribution can be corrected by using either an asymmetric DR structure or a symmetrized feeding method. Using either of these two methods, the simulated coupling coefficient is reduced to less than -15 dB.

In the validation measurements, an impedance bandwidth of 13.5% is achieved for Port 1 with a prototype using a symmetrical feeding network based on sequential rotation technique. The proposed feeding method will be employed extensively in the following chapters. The measured 3 dB AR bandwidth extends from 4.52 to 4.84 GHz, which yields an overlap with the impedance bandwidth of 6.8%. The measured mutual coupling is below -30 dB throughout the CP band. The simulated and measured radiation patterns show broadside LHCP radiation patterns with more than 60° usable CP angle.

For the measurement of Port 2, vertically polarized monopole-type radiation patterns with low cross-polarization are obtained, with an impedance bandwidth of 38.5%. The overlapping of the CP and LP band makes the proposed antenna suitable for diversity application. The MEG and ECC are calculated from S-parameters to evaluate the

diversity performance of the proposed antenna. Both simulated and measured results demonstrate good diversity antenna performance with low port mutual coupling, high port MEG and low ECC.

Chapter 5

Horizontally polarized omnidirectional DRA

THIS chapter introduces the concept of using cylindrical dielectric resonator antenna (DRA) as horizontally polarized omnidirectional antenna. The design is achieved through the excitation of the $TE_{01\delta}$ mode in the dielectric cylinder, a mode traditionally exploited in filtering applications of dielectric resonators (DRs). As the mode is intrinsically resonant in a narrow band, an air gap is introduced in the design and a dual point feeding network is optimized to achieve a wider impedance bandwidth with radially symmetric radiation patterns. The experimental results show a good agreement with simulation and demonstrate omnidirectional operation with horizontal polarization over a bandwidth of 5.6% around the centre frequency of 3.9 GHz.

5.1 Introduction

The electric monopole is one of the commonly used vertically polarized (VP) antennas in urban or indoor wireless environment due to its omnidirectional coverage and simplicity. However, monopole antennas usually exhibit a high profile, which cannot be applied in some wireless communication scenarios. From the wireless system point of view, the polarization of a propagating electromagnetic wave may change significantly due to the complicated wave propagation conditions, such as reflection, diffraction, and refraction, in indoor and urban areas. Therefore, the use of horizontally polarized (HP) antennas with conical radiation pattern [106–108] could also supplement VP receiving antennas to enhance diversity or realize a multiple-input-multiple-output (MIMO) system and solve the problem of polarization change resulting from reflection and scattering. Furthermore, HP antennas have advantages of compact size and low profile and therefore can be an attractive alternative for various mobile applications [109–111].

Most of HP omnidirectional antennas are designed based on loop structures. The electromagnetic field of an electrically small loop with a uniform current distribution is the same as that of a magnetic dipole [99]. Jiang et al. [110] proposed a compact ⌖ shaped HP omnidirectional antenna with impedance bandwidth of 5.6% and an average gain of 1.42 dB. In the design, the practical realization of small loops with uniform current distribution lead to good omnidirectional patterns. However, small loops have very small radiation resistance and high reactance and consequently result in impedance matching problem and narrow bandwidth of normally below 6%. A ladder network with left-handed loading was introduced to improve the impedance matching of a loop antenna in [112]. The impedance bandwidth of loop-structure HP antennas was slightly increased by introducing parasitic arc-shaped strips in [111] and an electromagnetic band gap (EBG) reflector in [113]. Recently, a periodical capacitive loading was proposed to solve the impedance matching problem [114]. The periodical capacitive loading was realized by adding interlaced coupling lines at the end of each arc-shaped strip section. With the periodical capacitive loading, a HP omnidirectional printed loop antenna with impedance bandwidth of 31.2% was achieved. An alternative way of realizing a uniform loop current distribution has been proposed by Alford [115]. A printed Alford-loop-structure antenna with 2% impedance bandwidth was designed for WLAN application in [109]. This Alford-loop-structure antenna consists of two Z-shaped strips printed on the top and bottom of the printed circuit board

(PCB). The "loop" type current distribution is formed by the two "wings" of each Z-shaped stripes.

Additional to these loop-structure antennas, several HP omnidirectional antenna arrays are proposed to achieve high gain and wide bandwidth. The early attempt of designing HP patch antenna array only resulted in an impedance bandwidth of 2.1% in [116]. An impedance bandwidth of 38% was achieved by using four magneto-electric dipoles in a ring configuration [106]. An in-phase power divider was utilized to excite these magneto-electric dipoles. Qing et al. [117] proposed a HP omnidirectional slot antenna array with two slot-elements, achieving an impedance bandwidth of 21.3% and the maximum gain of 5.5 dBi. In order to have current remaining in phase and uniform along a loop-structure, an artificial mu-negative transmission line (MNG-TL) was utilized to form the loop in [118]. The fabricated four-element series-fed MNT-TL loop antenna array offers HP radiation patterns with impedance bandwidth of 10.6% and gain of 6.5-7.9 dBi.

Although the impedance bandwidth and gain can be improved by using an array structure, the conventional metallic HP antenna array has bulk size and high manufacture cost. In this chapter, inspired by the fact that the $TE_{01\delta}$ mode in a cylindrical dielectric resonator (DR) has a similar E-field distribution as that of a loop-structure, we propose to use the $TE_{01\delta}$ mode to radiate HP omnidirectional patterns. The $TE_{01\delta}$ mode is traditionally exploited in filtering applications [16,73] because of its high quality (Q) factor. An attempt to obtain a horizontally polarized pattern by exciting this $TE_{01\delta}$ mode is found in [119]. However, only a 2% impedance bandwidth is achieved in simulation and impedance is mismatched in the prototype measurements.

To overcome the detrimental effect of high Q factor on the operation bandwidth of the dielectric resonator antenna (DRA), an air gap between the DR and the substrate is introduced. A dual point feeding structure is proposed, and includes two microstrip arcs which are optimized for further enlarging the DRA bandwidth and to achieve rotationally symmetric radiation patterns. The design principle is validated through measurements performed on a fabricated prototype. Compared with conventional horizontally polarized antennas, the proposed antenna has advantages of compact size, low profile and simplicity of design and manufacture. Based on the HP DRA structure proposed in this chapter, an extension to a dual polarized DRA is realized in the next chapter.

5.2 HP DRA design

The magnetic field distribution of the $TE_{01\delta}$ mode of a cylindrical DR is equivalent to a magnetic dipole located at the centre of cylinder, as shown in Fig. 5.1(a). According to the field distribution, it is evident that coupling can occur when an appropriate microstrip line excitation is placed close to the DR. To obtain an efficient coupling in filter design, a balanced coupling method is usually employed by placing two arc-shaped microstrip lines on each side of the DR [73, 120], as shown in Fig. 5.1(b). The balanced coupling method will be utilized to design an HP omnidirectional DRA in this chapter. The feeding structure is optimized to achieve a the maximum impedance bandwidth in Section 5.2.3.

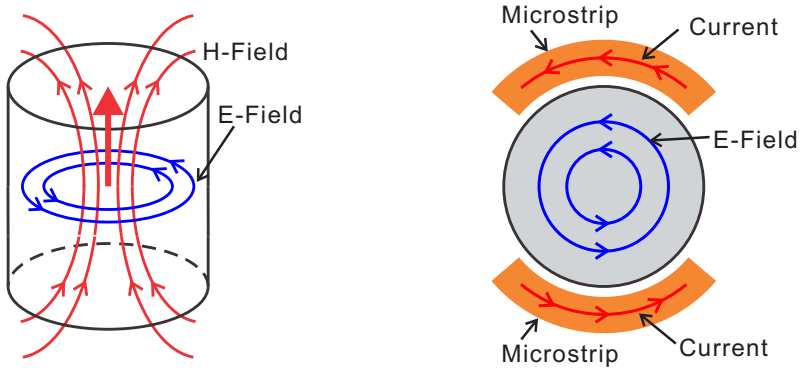

(a) Field distribution (b) A balanced coupling method

Figure 5.1. (a). Field distribution of $TE_{01\delta}$ mode in a cylindrical DR. (b). A balanced coupling method by placing two arc-shaped microstrip feeding lines in each side of a DR.

The DR design is based on a Rogers® dielectric board with 7.62 mm thickness and relative permittivity ε_r = 10. To simplify the manufacture process, the DR height is kept as the original dielectric board thickness of 7.62 mm.

5.2.1 Excitation of the $TE_{01\delta}$ mode

In the initial design, a cylindrical DR is directly positioned onto two arc-shaped microstrip feeding lines excited in-phase. The feeding lines are placed underneath the DR in order to maximize coupling and reduce the unwanted radiation from the feeding lines. Given the DR relative dielectric permittivity of 10 and height of 7.62 mm,

the radius of the DR is determined according to the standard engineering formulas Eq. (2.36) found in [36] for resonance of cylindrical DRs at the desired frequency in the desired mode. For a resonance frequency f_c = 4 GHz as chosen here, a cylinder with radius 20 mm and height 7.62 mm will be resonant in the $TE_{01\delta}$ mode. Based on these initial parameters, the DRA element and feeding network are simulated and optimized by using the field solver Ansoft® HFSS, employing the finite-element method (FEM) in the frequency-domain. The red curve in Fig. 5.2 shows a simulated impedance bandwidth of 2.7%, which is consistent with the intrinsic high Q-factor for the $TE_{01\delta}$ mode reported in filter applications.

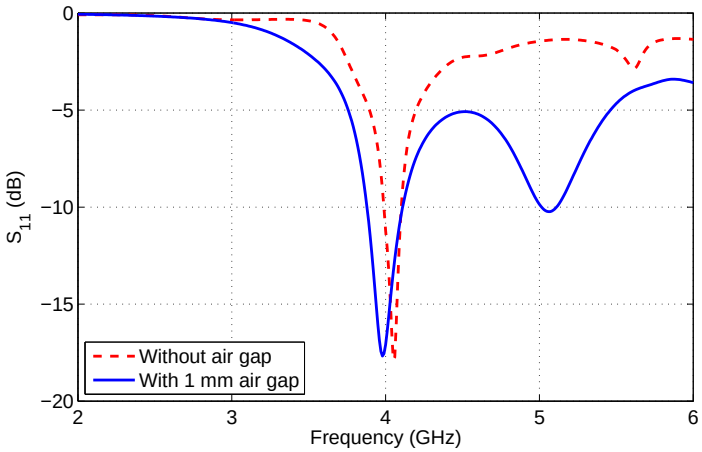

Figure 5.2. Simulated reflection coefficient for two DRAs, showing the increase of bandwidth resulting from the addition of a 1 mm air gap.

5.2.2 Bandwidth enhancement by addition of an air gap

Junker et al. [121] indicated that an air gap can increase the bandwidth of a cylindrical DR operating in TM_{01} mode, which has a electric field component normal to the ground plane. In this design, we validate that an air gap can also increase the impedance bandwidth of cylindrical DR operating in $TE_{01\delta}$ mode, which has a electric field component parallel to the ground plane. The air gap is also helpful to increase the distance between E-field and the ground plane. Indeed, if the DR is directly placed on the ground plane, the $TE_{01\delta}$ mode will be suppressed since it is parallel to the ground plane, as shown in Fig. 5.1(a). To realize this air gap, the main DR with radius R_1 = 20 mm and height h_1 = 6.62 mm is placed on top of a smaller cylinder with radius of

R_2 and height of h_2, as shown in Fig. 5.3. Through addition of a 1 mm air gap, the simulated impedance bandwidth is successfully increased from 2.7% to 5.7%, as shown in Fig. 5.2.

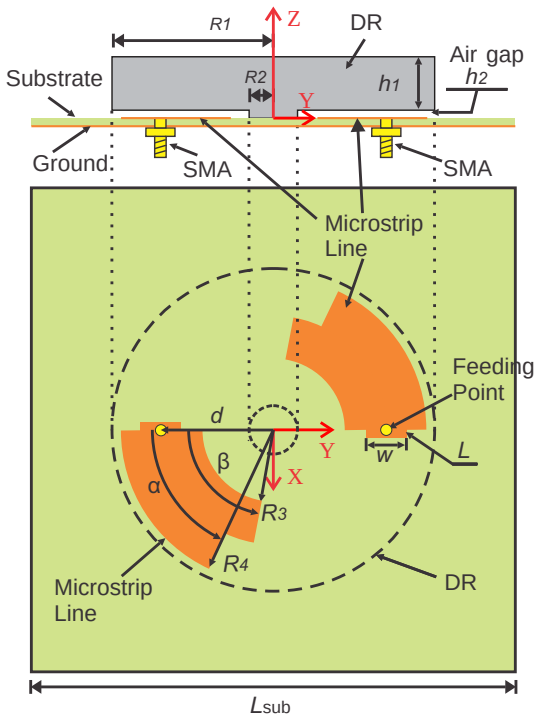

Figure 5.3. Side and top view of the proposed antenna.

A second resonance can be observed in Fig. 5.2 at a frequency above the $TE_{01\delta}$ resonance. This second resonance has been investigated to see if it could be merged with the $TE_{01\delta}$ resonance to enhance the bandwidth while preserving the radiation properties. This second resonant frequency shifts downward from 5.22 GHz to 4.76 GHz when the height of lower cylinder (i.e. the height of air gap) is reduced from 1.5 mm to 0.5 mm, as shown in Fig. 5.4(a). The impedance bandwidth is increased from 5.42% to 7.58% due to the downward moving of the second resonant frequency. The electric field distribution for the first resonance at 3.9 GHz and the second one at 5.1 GHz are illustrated in Fig. 5.5(a) and 5.5(b), respectively. The magnetic field distributions in the YZ plane of these two resonance frequencies are also plotted in Fig. 5.6(a) and 5.6(b). These field plots confirm that the first resonant frequency is related to the excitation of the $TE_{01\delta}$ mode, and reveal that the second resonance is linked to the $HEM_{21\delta}$ mode. The resonance of the $TE_{01\delta}$ mode is also confirmed by the calculated frequency using engineering equations Eqs. (2.38). However, there are no closed-form equations to calculate the resonance frequency of the higher-order $HEM_{21\delta}$ mode. The discussion of

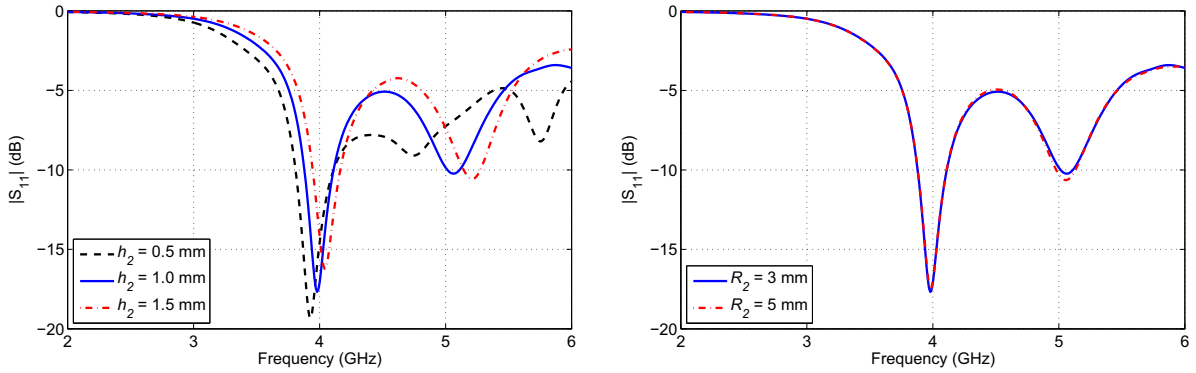

(a) Height h_2 effect

(b) Radius R_2 effect

Figure 5.4. Simulated reflection coefficient of different the lower cylinder height and radius values.

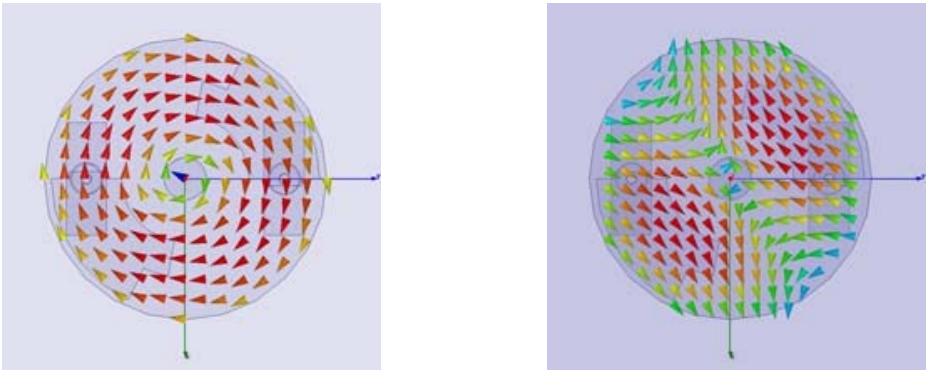

(a) $TE_{01\delta}$ mode (3.9 GHz)

(b) $HEM_{21\delta}$ mode (5.1 GHz)

Figure 5.5. Top view of electric field distribution inside the DR with 1 mm air gap.

the higher-order modes is out of the scope of this thesis and the reader interested in further information is referred to [122]. Fig. 5.7 shows the simulated 3D radiation pattern of these two modes. Although they have similar co-polarization radiation patterns, the $HEM_{21\delta}$ mode exhibits higher cross-polarization level. Therefore, the two modes are not compatible for merging with consistent radiation patterns. The simulation result in Fig. 5.4(b) indicates that the radius of the lower cylinder DR has little effect on the impedance and resonant frequency. The lower DR with height $h_2 = 1$ mm and radius $R_2 = 3$ mm is utilized to form the air gap, as shown in Fig. 5.3.

(a) $TE_{01\delta}$ mode (3.9 GHz) (b) $HEM_{21\delta}$ mode (5.1 GHz)

Figure 5.6. Side view (YZ plane) of magnetic field distribution inside the DR with 1 mm air gap.

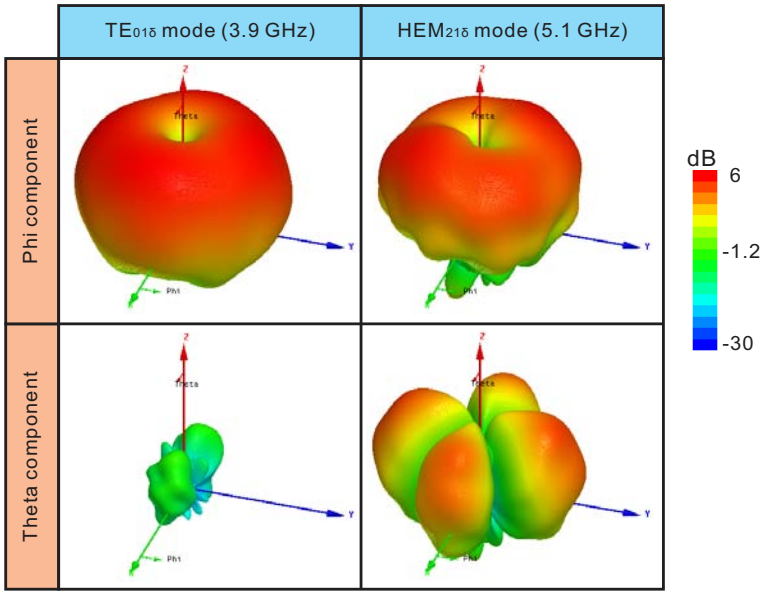

Figure 5.7. Simulated 3D radiation patterns of the $TE_{01\delta}$ mode at 3.9 GHz and the $HEM_{21\delta}$ mode at 5.1 GHz.

5.2.3 Feeding structure optimization

The $TE_{01\delta}$ mode is excited by a balanced coupling method formed by two curved microstrip lines. The impedance bandwidth is optimized by adjusting the shape of these two feeding lines. The schematic of Fig. 5.3 shows that these microstrip lines have a wide arc followed by a narrower one. Using a wide segment is necessary to increase the coupling to the DR because of the air gap, while the arc length α of the wider arc provides an additional degree of freedom in the design. The effect of varying α on the impedance bandwidth is illustrated in Fig. 5.8. With the increase of α, the bandwidth of the $TE_{01\delta}$ mode is widened towards higher frequencies. The simulated bandwidth extends to 12.5% when α is equal to 80°. However, this bandwidth extension is at the cost of increase in cross polarization, as shown in Fig. 5.9. This increased horizontal

Table 5.1. Antenna parameters for the final design, in the geometry of Fig. 5.3

Symbol	Value	Symbol	Value	Symbol	Value
h_1	6.62 mm	h_2	1 mm	R_1	20 mm
R_2	3 mm	R_3	9 mm	R_4	19 mm
α	65°	β	80°	d	14 mm
w	5 mm	L	1 mm	L_{sub}	100 mm

polarization is most probably explained by the detrimental effect of the the coupling with the $\text{HEM}_{21\delta}$ mode, as discussed in the previous paragraph and shown in Fig. 5.7. Thus, there exists a trade-off between bandwidth and cross-polarization in the present design. A value of $\alpha = 65°$ is chosen as final value to ensure that cross-polarization levels are at least 15 dB lower than co-polarization levels in the direction of maximum radiation. Finally, a small stub with $L = 1$ mm and $w = 5$ mm is added behind the feed point of each microstrip line to ease impedance matching and reduce reflections. The final antenna parameters are tabulated in Table 6.1.

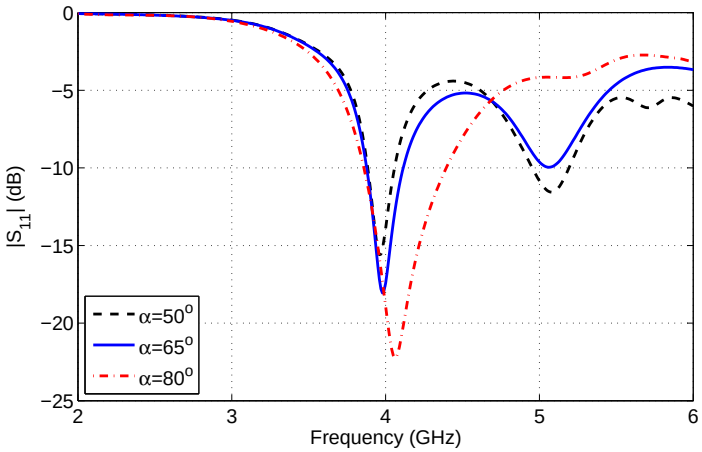

Figure 5.8. Simulated impedance bandwidth for different values of α.

5.3 Fabrication

A prototype has been fabricated for the optimal design parameters mentioned above, as shown in Fig. 5.10. In the manufacture, the DR is cut from a Rogers® dielectric board with 7.62 mm thickness and relative permittivity $\varepsilon_r = 10$. Then, a ring with height $h_2 = 1$ mm and inside radius $R_2 = 3$ mm is removed from the bottom of the

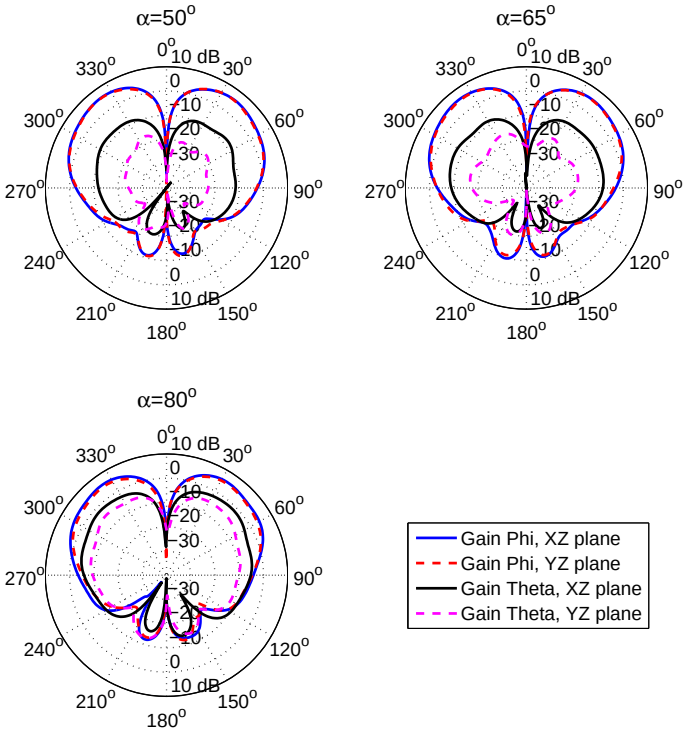

Figure 5.9. Simulated radiation patterns at the upper limit of the bandwidth, for different values of α.

cylinder to form the lower cylinder. The cylindrical DR is mounted on a Rogers® Ultralam substrate with back-side metallization. The square substrate, with side length of 100 mm and thickness of 1.524 mm, has a relative dielectric permittivity of 2.5 and a loss tangent of 0.001. The $TE_{01\delta}$ mode is excited by two curved microstrip lines with identical sizes printed on the top of the substrate. Two SMA connectors, located at the back of the substrate, are utilized to connect the two microstrip lines to the Agilent N5230A network analyzer through a T-junction splitter. The pins of the SMA connectors are soldered onto the microstrip lines.

5.4 Experimental results

The simulated and measured reflection coefficients for the proposed antenna are shown in Fig. 5.11. The measured impedance bandwidth ($|S| <$ -10 dB) covers a frequency range from 3.84 to 4.06 GHz. A small offset of the $TE_{01\delta}$ resonance frequency is observed between measurement and simulation. This offset most probably arises from fabrication imperfections. Compared with simulation results, a stronger resonance is observed at 5.1 GHz in the measurement result, which can be explained by the effect

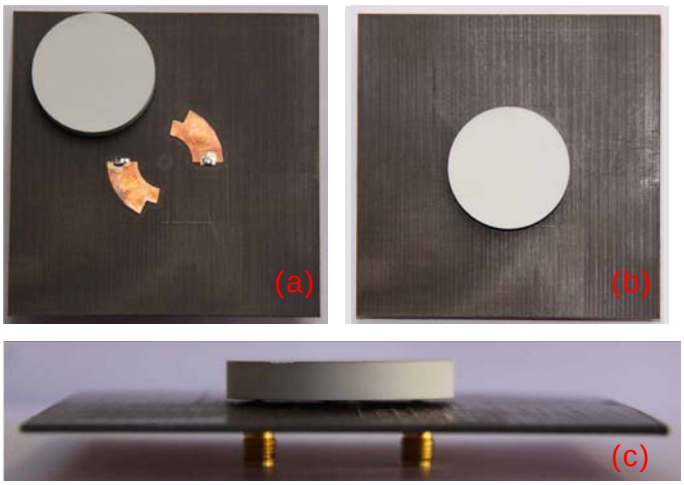

Figure 5.10. Realized prototype of horizontally polarized DRA. (a) and (b) Top view without and with DR on microstrip arcs; (c) Side view.

of inaccurate clearance radius around the feeding vias. The metal around the via holes is removed to avoid a short between pin and ground, as shown in Fig.5.12. The designed radius for the feeding vias and metal clearance are 0.635 mm and 0.75 mm, respectively. In the substrate of the realized prototype, the radius of the metal clearance was measured to be about 0.9 mm. The inaccuracy of this clearance radius only affects the impedance of the higher mode. A re-simulation of the reflection coefficient for the antenna, including the realized clearance radius shows a good agreement with the measured result at both $TE_{01\delta}$ and $HEM_{21\delta}$ mode resonant frequencies, as shown in Fig. 5.11.

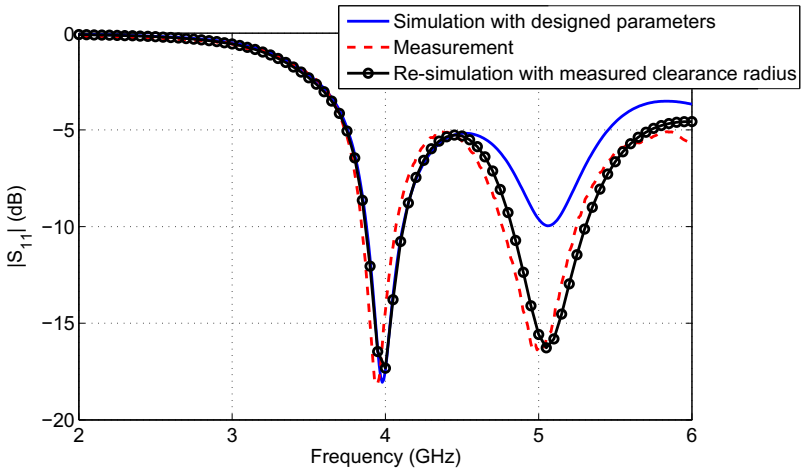

Figure 5.11. Simulated and measured antenna reflection coefficient.

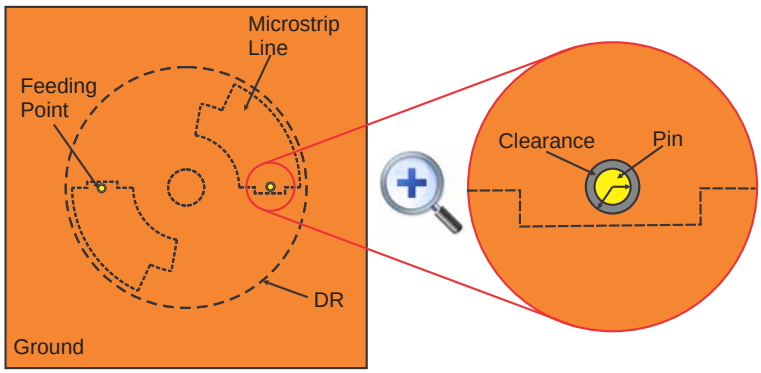

Figure 5.12. Bottom view of the substrate showing the ground plane. The zoomed in view of the region around a via shows the clearance zone where the metal is removed.

The measured and simulated radiation patterns are depicted in the Fig. 5.13 at the resonance frequency of 3.9 GHz. As desired, these radiation patterns correspond to the patterns of a vertical magnetic monopole, i.e omnidirectional patterns with a horizontal main polarization component. The relatively high cross-polarization level in the XZ plane (as defined in Fig. 5.3) compared to that in the YZ plane results from radiation at the end of the wide microstrip arcs. The cross-polarization level is reduced by using narrow microstrip arcs in a dual polarized omnidirectional DRA design in the next chapter. In the XZ plane, the difference between cross-polarization levels and co-polarization levels are in the range of 13.1 to 19.7 dB with a minimum at $\theta = 90^o$ and a maximum at $\theta = 45^o$, respectively. The simulated and measured radiation pattern in the XY plane further validates the omnidirectional features. The oscillations of the patterns in the XY planes are attributed to the imperfections of the anechoic chamber, which are accentuated in the measurement of omnidirectional antennas.

The maximum gain of the proposed antenna has been measured by using the gain-transfer method, as described in the Section 3.3, in comparison with a linear standard gain horn antenna. A good agreement between simulated and measured gain can be observed in Fig. 5.14. Within the frequency range from 3.84 to 4.06 GHz, the antenna gain remains above 4 dB with a maximum of 5.2 dB.

The performance of the proposed cylindrical DRA is compared with that of other horizontally polarized antenna designs found in the literature. This comparison considers the antenna length, height, bandwidth and peak gain. The size and performance of each antenna are tabulated in Table 5.2. HP antennas in [109, 110, 114, 116] are based

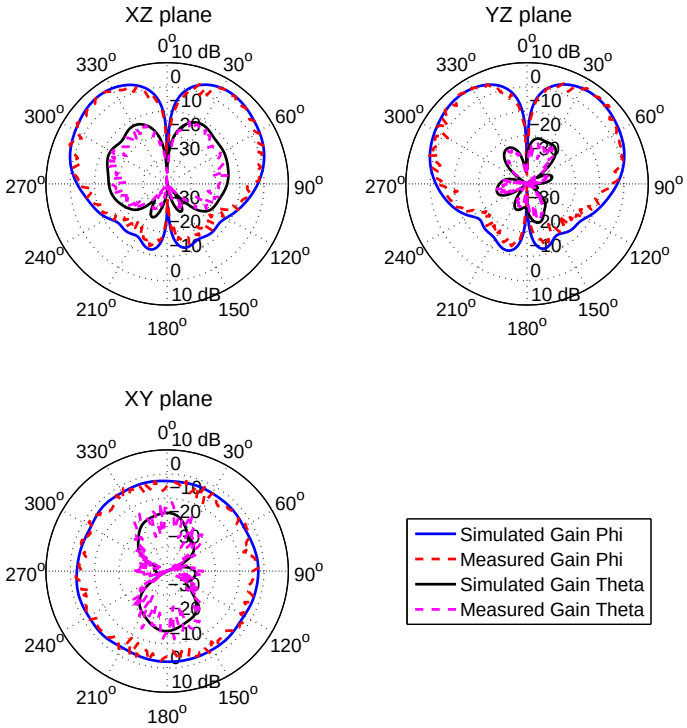

Figure 5.13. Simulated and measured gain patterns at 3.9 GHz.

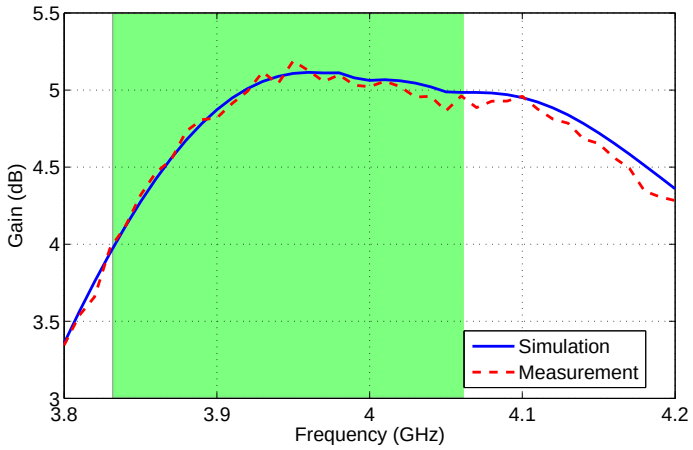

Figure 5.14. Simulated and measured maximum gain of the conical pattern.

on microstrip printed on a substrate. These antennas have features of low profile and cost but usually exhibit low gain. The HP antenna arrays in [106, 117, 118] achieve a wide bandwidth and relatively high gain. However, these arrays have large structure and high profile. The antenna proposed in the present chapter is characterized by its of simplicity, low profile and relatively high gain.

Table 5.2. Comparison between horizontally-polarized omnidirectional antennas

Description	Length	Height	Bandwidth	Peak gain
Alfrod loop antenna [109]	$0.14\lambda_0$	-	2%	0.1 dBi
⌀ shaped antenna [110]	$0.36\lambda_0$	-	5.6%	1.42 dB
Loop with periodical capacitive loading [114]	$0.38\lambda_0$	-	31.2%	2.5 dBi
Patch array [116]	$1.33\lambda_0$	-	2.1%	0 dB
Cylindrical DRA	$0.53\lambda_0$	$0.10\lambda_0$	5.6%	5.1 dB
Magneto-electric dipoles [106]	$0.86\lambda_0$	$0.19\lambda_0$	38%	6.5 dBi
Slot antenna array [117]	$1.92\lambda_0$	$0.18\lambda_0$	21.3%	5.5 dBi
MNG-TL loop antenna array [118]	$4\lambda_0$	$1.2\lambda_0$	10.6%	7.9 dBi

5.5 Conclusion

This chapter has proposed a horizontally polarized cylindrical DRA. The omnidirectional radiation pattern is achieved by exciting the $TE_{01\delta}$ mode in a cylindrical DR. This mode has been only used successfully in filter applications before, to the best of our knowledge. The $TE_{01\delta}$ mode is excited by a dual-point feed scheme with identical microstrip line arcs, and radiates as a vertical magnetic dipole. The main disadvantage of this resonant mode, is its high Q-factor that results in a narrow bandwidth.

Two techniques have been proposed to enhance this bandwidth. Firstly, an air gap is introduced between the cylindrical DR and the ground plane. Secondly, a balanced coupling method is realized, by placing two arc-shaped microstrip lines on each side of the DR. This scheme has been demonstrated to provide effective coupling to the DR. The feeding lines are optimized to enhance the bandwidth, while preserving the desired radiation characteristics. A numerically optimized design has been validated through measurements and has demonstrated a 5.6% bandwidth with omnidirectional horizontally polarized radiation. The proposed antenna is extended to an omnidirectional dual polarized DRA for diversity application in the next chapter.

Chapter 6

Horizontally and vertically polarized omnidirectional DRA

THIS chapter proposes a diversity annular cylindrical dielectric resonator antenna (DRA) realizing simultaneously omnidirectional horizontally and vertically polarized radiation patterns with low cross-coupling. The horizontally and vertically polarized radiation patterns are achieved by exciting the orthogonal $TE_{01\delta}$ and $TM_{01\delta}$ modes in a single cylindrical DR, respectively. Due to the high Q factor of the $TE_{01\delta}$ mode, an air gap and multi-feeding lines have been introduced to increase the impedance bandwidth. The proposed antenna provides an impedance bandwidth of 19.1% in the vertically polarized mode and an overlapping bandwidth of 7.4% in the horizontally polarized mode, the overlapping band ranging from 3.78 to 4.07 GHz. Antenna diversity and multiple-input multiple-output (MIMO) performance are examined in terms of envelope correlation coefficient and mean effective gain.

6.1 Introduction

Systems employing polarization diversity are robust against polarization mismatch between the receiver and transmitter. Unlike space and pattern diversity in which multiple antenna elements are separated by large distances to obtain high-diversity gain, polarization diversity offers the desired diversity benefits without physical separation of the branches, which is suitable for space-constrained locations [99]. Especially, the use of two orthogonal polarizations, typically the vertical polarization (VP) and the horizontal polarization (HP), allows to realize polarization diversity in one antenna element because of small cross correlation between orthogonal polarization components.

Several dual-polarized omnidirectional antennas have been proposed in attempts to solve the polarization mismatch in cell phone and WLAN applications. A compact notch-wire antenna, composed of a wire-loop antenna for VP and a three-notched disk antenna for HP, was realized for polarization diversity reception in an indoor base-station system [123]. An impedance bandwidth of 8.5% for VP and of 17% for HP were measured, with the low isolation of 14 dB between two ports. Ando et al. [108] proposed a dual-polarized omnidirectional antenna for personal-handy phone base stations mounted on the rooftops of buildings. The proposed antenna is composed by a conventional collinear array and a dielectric-loaded slotted-cylinder antenna for VP and HP, respectively. The measured impedance bandwidth for the combined dual-polarized antenna reaches about 5%. In a 5.2 GHz planar slot antenna design proposed in [124], the VP and HP were realized by exciting coplanar and slotline mode, respectively. The common working band of the antenna is 10.6% with high port-to-port isolation of below 59 dB. The gain of these two ports are 2.59 and 3.52 dB, respectively. Deng et al. [125] proposed a dual-polarization microstrip patch antenna with high ports isolation of below 35 dB. The HP with impedance bandwidth of 3.8% is realized by four in-phase identical curved branches arranged in a circle, while VP with impedance bandwidth of 9.4% is realized by an annular-ring patch fed by coupling of a modified capacitive coupling structure.

To achieve a dual-polarization antenna with omnidirectional radiation patterns, the horizontally polarized radiated element design is the key challenge because of the impedance matching and uniform current distribution issues, as discussed in the Chapter 5. In that chapter, the concept of using the $TE_{01\delta}$ mode in a cylindrical dielectric resonator (DR) as a radiating mode has been validated by optimizing the feeding network

and introducing an air gap between the resonator and the substrate. An impedance bandwidth of 5.6% has been demonstrated in both simulation and measurement.

In this chapter, this concept is extend to a dual-mode DRA with a magnetic-dipole-like and electric-monopole-like radiation patterns obtained simultaneously by exciting the $TE_{01\delta}$ and $TM_{01\delta}$ modes in a single annular cylindrical DR. Two groups of four radially arranged microstrip feeding lines with two different lengths are utilized to increase the bandwidth of the $TE_{01\delta}$ mode and suppress the influence of higher-order modes. The overlapping operating band for the two functions makes the proposed antenna suitable for being used in diversity or MIMO communication systems, when omnidirectional characteristics are required. The proposed antenna has the advantage of the combination of compact size and wide bandwidth.

6.2 Dual polarized DRA design

The prototype of the proposed dual polarized antenna and schematic $TE_{01\delta}$ and $TM_{01\delta}$ mode field distribution are shown in Fig. 6.1. An annular cylindrical DR is mounted on a Rogers® Ultralam substrate with thickness of 1.524 mm and relative permittivity of 2.5. The two functions of the antennas are fed through two SMA connector ports located on left and right side of substrate. The feeding network is located on the back side of the ground plane and shielded in a metallic cavity. A schematic of the proposed dual polarized antenna is illustrated in Fig. 6.2, with all dimensions listed in Table 6.1. The design procedure is explained in the following.

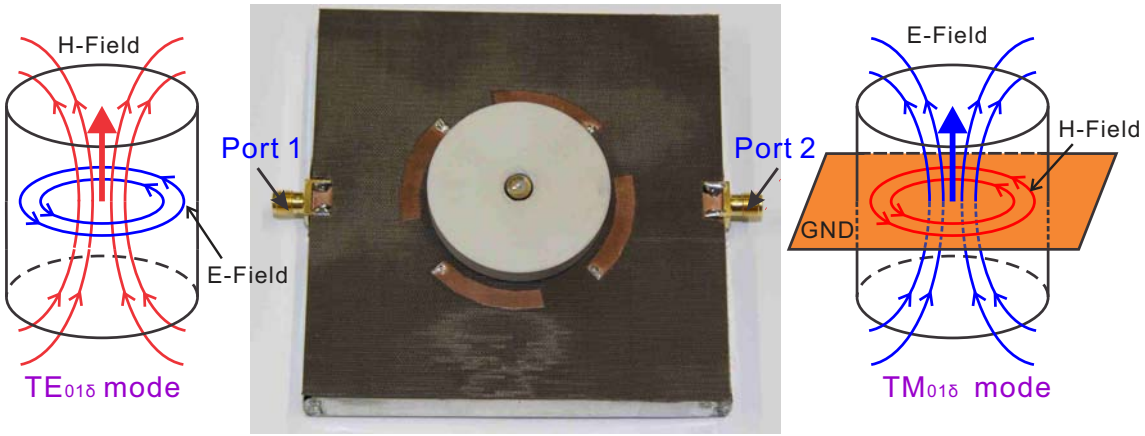

Figure 6.1. Prototype of the proposed dual polarized omnidirectional DRA with schematic field distributions for the two orthogonal modes excited.

Table 6.1. Antenna parameters of the dual polarized DRA

Symbol	Value (mm)	Symbol	Value (mm)	Symbol	Value (mm)
L_1	12	L_2	13	L_3	35
L_4	78	L_5	13.5	L_6	14
L_7	36.5	W_1	3	W_2	3.5
W_3	1.22	W_4	1.22	W_5	4.35
W_6	3	W_7	4.35	W_8	3
W_9	4.5	W_{10}	4	L_{sub}	100
h_1	6.62	h_2	1	h_3	10
R_1	22	R_2	10	R_3	3.5
R_4	14	R_5	2.9	L_{arc1}	22.7
L_{arc2}	6.4				

The horizontally and vertically polarized radiation patterns are realized by exciting the orthogonal $TE_{01\delta}$ and $TM_{01\delta}$ modes from Ports 1 and 2, respectively. The design is carried out in three steps: Firstly the DR geometry is calculated; secondly the feeding network for the $TE_{01\delta}$ mode is realized, and thirdly the design is extended to include the feeding network for the $TM_{01\delta}$ mode. The DR and feeding networks are simulated and optimized with Ansys® HFSS.

6.2.1 DR design

A cylindrical DR is firstly designed to excite the horizontally polarized $TE_{01\delta}$ mode resonant at 3.9 GHz. The initial size of the DR is calculated based on closed-form formulas given in [7]. An air gap is introduced between the DR and the substrate to increase distance between DR and ground and hence widen the impedance bandwidth of this $TE_{01\delta}$ mode [24]. The effect of the air gap and radius of bottom cylinder is not specifically described here since it has been discussed in the previous chapter. The DR is cut from a dielectric slab with thickness of 7.62 mm and relative permittivity of 10. For simplicity of manufacture, the DR is kept at the original slab height of 7.62 mm. The size of DR can be scaled up or down for operation at other frequencies. The centre of the cylindrical DR is removed to provide room for a central probe feed, as shown in Fig. 6.3. The radius of the top and bottom cylinder and the hole are optimized to achieve the maximum impedance bandwidth.

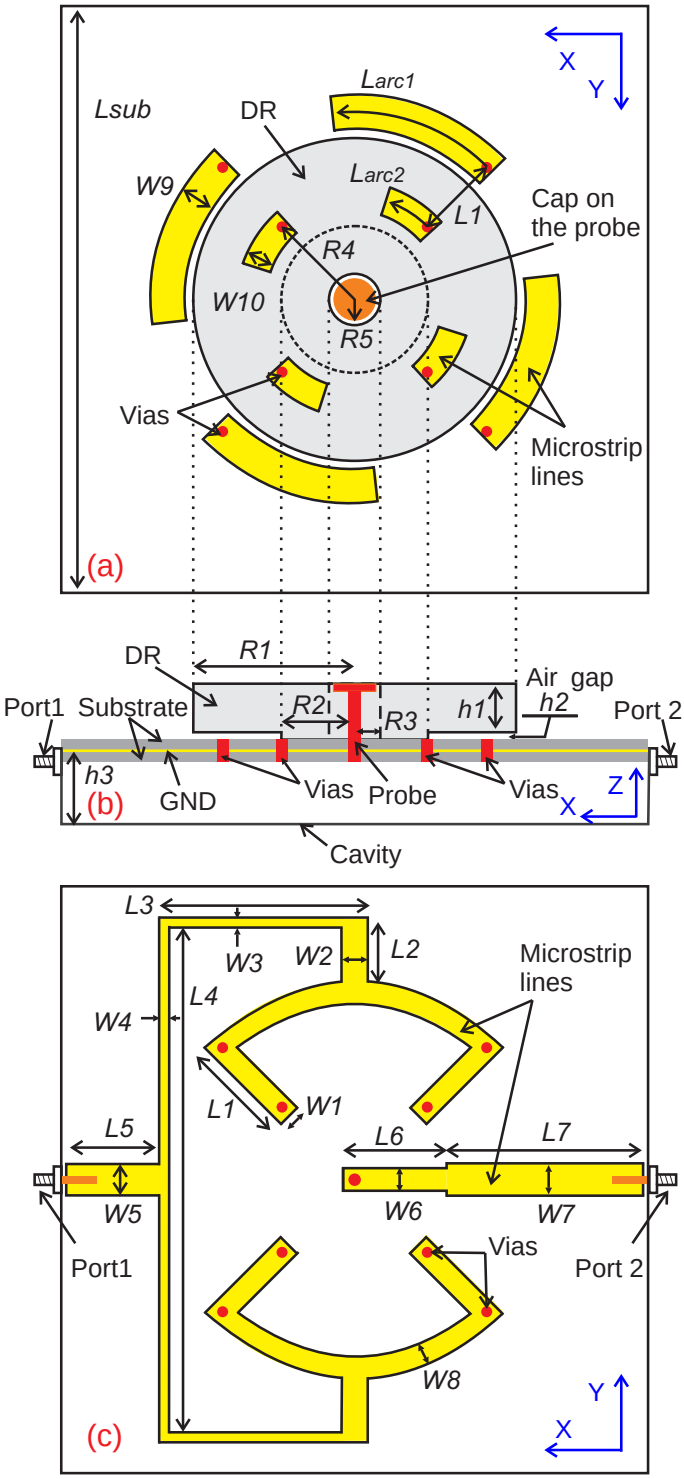

Figure 6.2. Geometry of the proposed dual-polarized DRA. (a) Top view. (b) Side view. (c) Bottom view (without cavity).

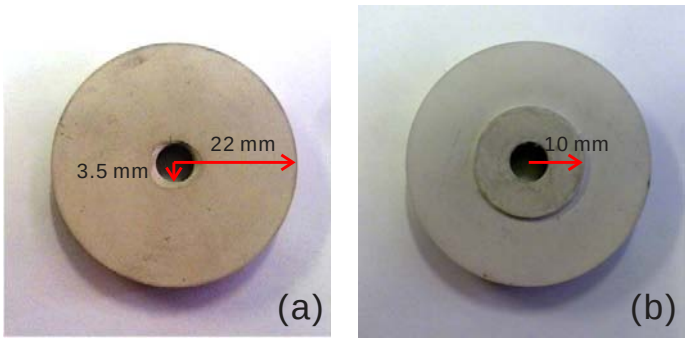

Figure 6.3. Prototype of DR. (a) Top view. (b) Bottom view

6.2.2 Excitation of $TE_{01\delta}$ Mode

In the previous chapter, the impedance bandwidth of the $TE_{01\delta}$ mode was increased to 5.6% by using two long and wide curved microstrip feeding lines. However, this bandwidth improvement was obtained at the cost of the increase in cross-polarization due to the detrimental effect of the coupling with the higher mode $HEM_{21\delta}$. In the presently proposed design, two groups of four arc-shaped microstrip lines of different length and width are utilized to excite the DR, as shown in Fig. 6.2. By using this novel feeding method, the simulated impedance bandwidth, shown in Fig. 6.4(a), is further increased to 7.4% due to the combination of overlapping resonances excited by these two group feeding lines. The electric field distributions for the first resonant mode at 3.87 GHz and the second one at 4.02 GHz are shown in the inset of Fig. 6.4(a). These field plots confirm that both resonant frequencies are related to the excitation of the $TE_{01\delta}$ mode in the DR. In addition, increasing the number of feeding groups to four suppresses the radially asymmetric $HEM_{21\delta}$ mode. The real and imaginary parts of the input impedance shown in Fig. 6.4(b) demonstrates the branching into two resonant frequencies.

In the feeding network design process, a group of 50 Ω curved half wavelength microstrip lines (L_{arc1}) are firstly designed to excite a single resonant frequency. The feeding lines are initially placed at the outer periphery of the DR to achieve a good excitation efficiency and leave space for the inner feeding lines. The width of the feeding lines is slightly adjusted to match the feeding network. The location of the feeding lines is further moved as far out as possible from the DR to reduce the impact on other feeding parts while keeping the excitation efficiency within acceptable level.

The inner feeding lines are added to create a fork-like feeding structure and excite the higher resonant frequency. The width of the feeding lines is set to 4 mm to match

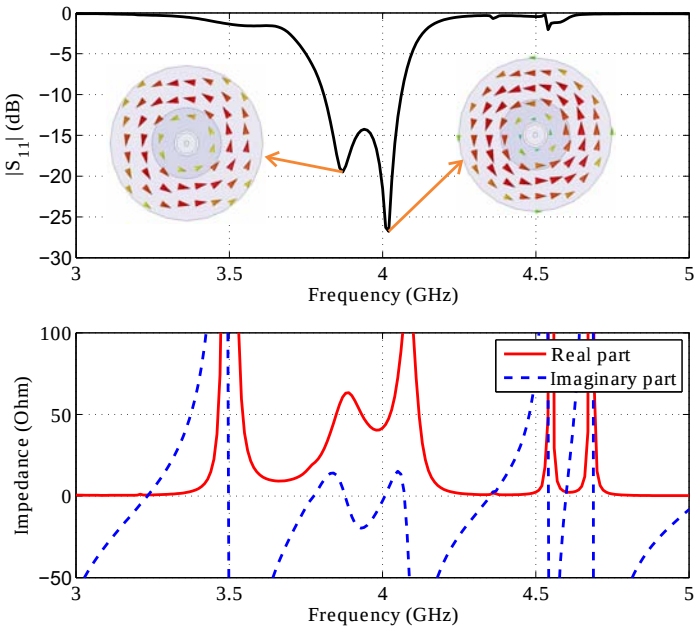

Figure 6.4. Simulated reflection coefficient and impedance of Port 1. Inset: $TE_{01\delta}$ mode electric field distribution inside the dielectric resonator at 3.87 and 4.02 GHz.

the existing feeding network. The higher resonant frequency is related to the added length of the shorter curved lines L_{arc2} and radial microstrip line L_1, as demonstrated in Fig. 6.5, where the first resonant frequency remains unchanged and the higher resonant frequency moves to higher or lower frequency with the decrease or increase of the length of the radial microstrip line (L_1), respectively. Furthermore, Fig. 6.6 illustrates that the impedance bandwidth can be further increased to 8.1% by moving the second resonant frequency toward to higher frequency through the optimization of the length L_1 and L_{arc2}. However the reflection coefficient of the middle frequency band becomes too close to -10 dB. Considering the manufacturing accuracy, the conservatively chosen length L_1 = 14 mm was used to realize a prototype.

In the manufacture, two substrates are cut from a Rogers® Ultralam substrate with backside metallization, as shown in Fig. 6.7. The curved microstrip feeding lines are printed on the top of Substrate I and the feeding networks is printed on the bottom of Substrate II. Then, the backside metal of these two substrates are attached together to form the ground plane. In order to reduce the impact from the feeding network, it is physically separated from the microstrip feeding lines by the ground plane. Vias with a diameter of 1 mm are employed to connect the feeding network and the arc-shaped microstrip feeding lines through holes in the ground plane and substrates.

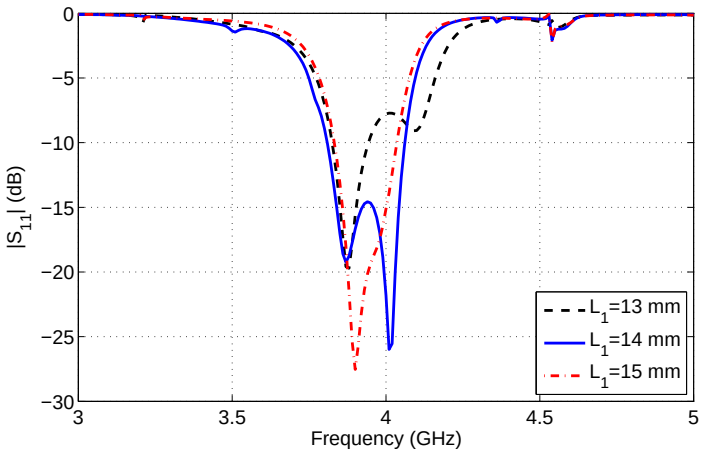

Figure 6.5. Simulated reflection coefficient of Port 1 with different length of L_1.

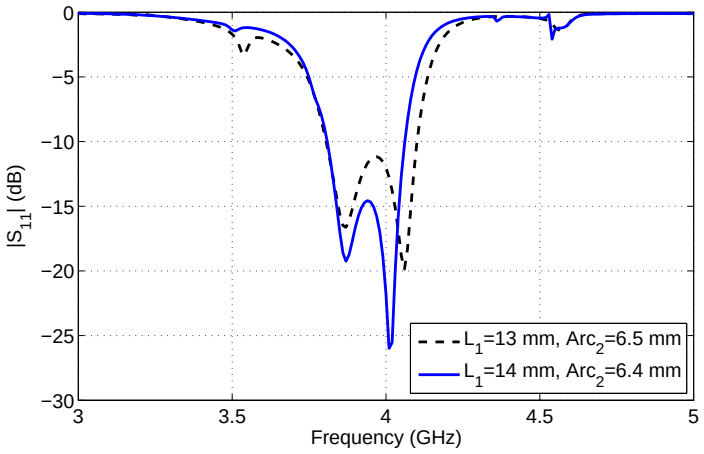

Figure 6.6. Simulated reflection coefficient of Port 1. Further bandwidth increase is in principle possible by optimizing length of L_{arc2} and L_1.

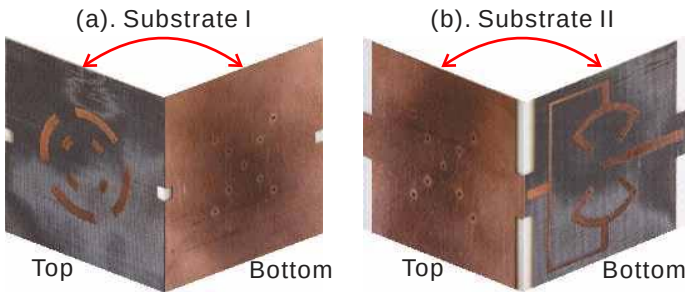

Figure 6.7. Physical layout of the substrate. (a) and (b): Top and bottom of Substrate I and II, respectively.

To connect the multiple arc-shaped feeding structure to Port 1, several T-junctions are printed on the bottom of Substrate II. The first T-junction, located on left side in Fig. 6.2(c) and 6.7(b), is utilized to connect the 50 Ω transmission line from the SMA connector (Port 1) to two 100 Ω transmission lines. Further, as seen on top and bottom of Fig. 6.2(c) and Fig. 6.7(b) the 100 Ω line branches out to two 31 Ω arcs, with matching realized through quarter-wave transformers (with length L_2 and width W_2).

Fig. 6.8 shows the first prototype antenna which does not include a metallic back cavity to seal the feeding network. The antenna exhibits a large back lobe radiation component in two resonant frequencies of Port 1 even with the large substrate and ground plane (150 mm), as shown in Fig. 6.9. This unwanted back radiation deforms the overall radiation pattern and degrades the efficiency. The back radiation mostly results from the curved feeding line on the bottom of the substrate. Therefore, a metallic cavity is employed to reduce the back radiation in the final prototype. The cavity height of 10 mm is less than a quarter wavelength to eliminate the resonance in the cavity. With the back cavity, the back lobe radiation is successfully reduced and the size of the substrate is also reduced to 100 mm. The simulated and measured radiation patterns are provided in the Section 6.3.

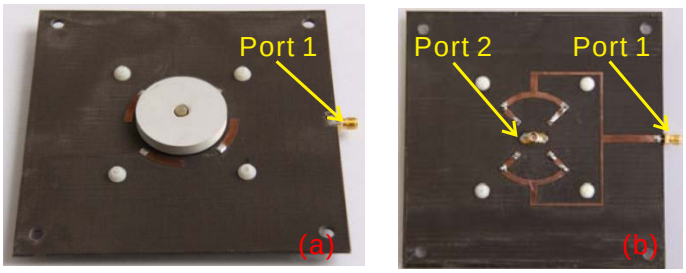

Figure 6.8. Top (a) and bottom (b) view of the first prototype antenna without back cavity.

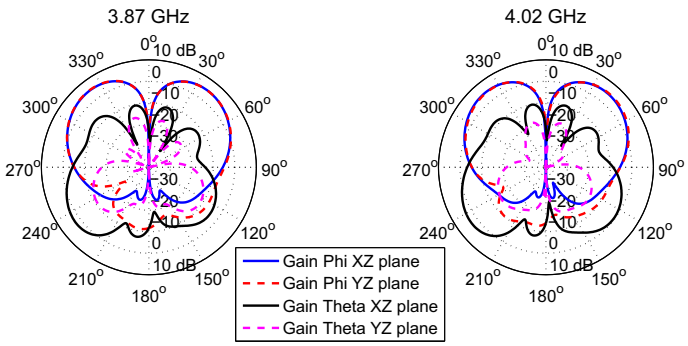

Figure 6.9. Simulated radiation patterns of Port 2 of the first prototype antenna without back cavity.

6.2.3 Excitation of the $TM_{01\delta}$ mode

In the first prototype, the central probe is directly connected to the SMA, located at the bottom of the substrate, as shown in Fig. 6.8(b). For better electromagnetic shielding performance and reduced manufacturing difficulty in the final design, the central probe (Port 2) is connected to a 50 Ω microstrip line by a quarter wavelength transmission line matching section, located at the bottom of the substrate, as shown on right side of Fig. 6.10(b).

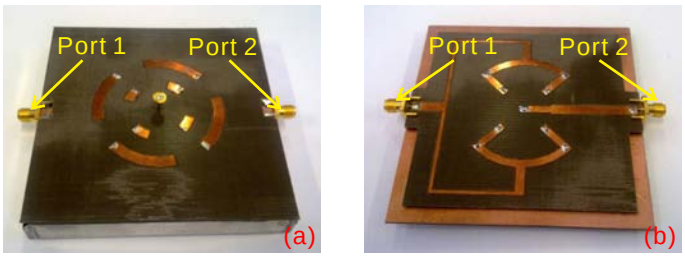

Figure 6.10. The realized feeding network. (a) Top view. (b) Bottom view.

The introduction of the annular geometry for the $TM_{01\delta}$ mode probe excitation does not influence markedly the $TE_{01\delta}$ mode, which has a zero E-field in the DR centre. For diversity and MIMO operation of the antenna, the impedance band of the two ports should overlap as much as possible to maximize the operation bandwidth. However, the resonant frequency of the pure $TM_{01\delta}$ mode is higher than that of the $TE_{01\delta}$ mode. Figure 6.11 shows the calculated resonance frequency of the $TE_{01\delta}$ and $TM_{01\delta}$ modes in a cylindrical DR with relative dielectric permittivity of 10 by using Eq. (2.36) and (2.38), respectively. The designed DR dimension has a ratio of 2.89 (radius 22 mm and height of 7.62 mm), indicated as the dash line in the figure. Therefore, in this third design step, the hybrid monopole DRA concept [31] is utilized to increase the bandwidth of Port 2. A metal cap is added on top of the electric monopole to shorten it [32] and hence lower the overall antenna profile, as shown in Fig. 6.10(a). The inner radius of the annular cylindrical DR and cap are adjusted to widen the bandwidth response of Port 2 and maximize its overlap with the bandwidth of Port 1. The radius of the cap is firstly set to 0.5 mm less than the inner radius of the annular cylindrical DR (R_3). The maximal bandwidth is obtained when R_3 is equal to 3.5 mm, as shown in Fig. 6.12. The radius the fabricated metal cap (R_5) is 2.9 mm which is close to the design value of 3 mm. This small tolerance has little effect on the measurement results, as shown in Fig. 6.13.

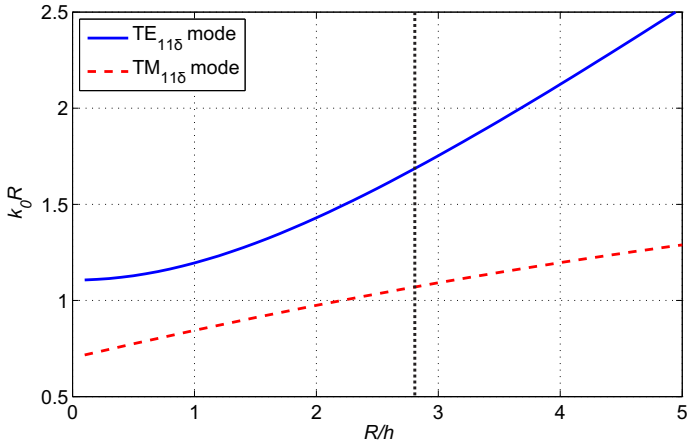

Figure 6.11. The comparison between the calculated resonance frequency of $TE_{01\delta}$ and $TM_{01\delta}$ mode in a cylindrical DR with dielectric permittivity of 10. k_0 is free-space wavenumber; R and h are DR radius and height, respectively.

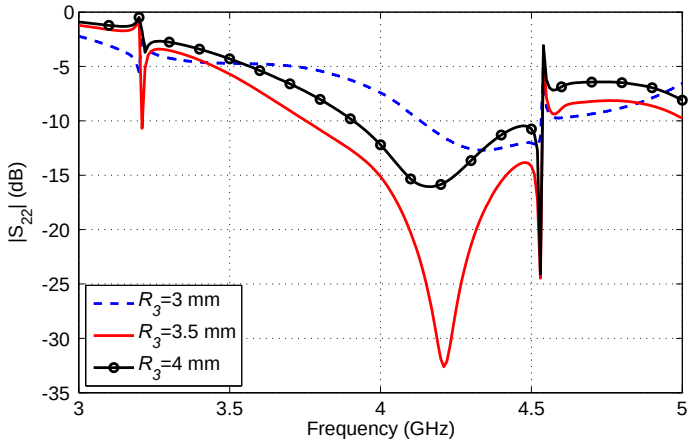

Figure 6.12. Simulated reflection coefficient of Port 2 for different values of inner radius of the annular cylindrical DR. The radius R_5 of the cap on the probe is 0.5 mm smaller than the inner radius R_3 of the annular cylindrical DR.

6.3 Antenna performance

6.3.1 S parameters

The reflection coefficients of Ports 1 and 2 are shown in Fig. 6.13(a), exhibiting a good agreement between simulation and measurement. The Port 1 excites the $TE_{01\delta}$ mode and presents an impedance bandwidth ($|S_{11}|$ < -10 dB) of 7.4%, whereas the Port 2 excites the $TM_{01\delta}$ mode with a 19.1% impedance bandwidth. The shaded area shows the usable overlapping band, which corresponds to the impedance working frequency band of Port 1, from 3.78 to 4.07 GHz. As shown in Fig. 6.13(b), the mutual coupling

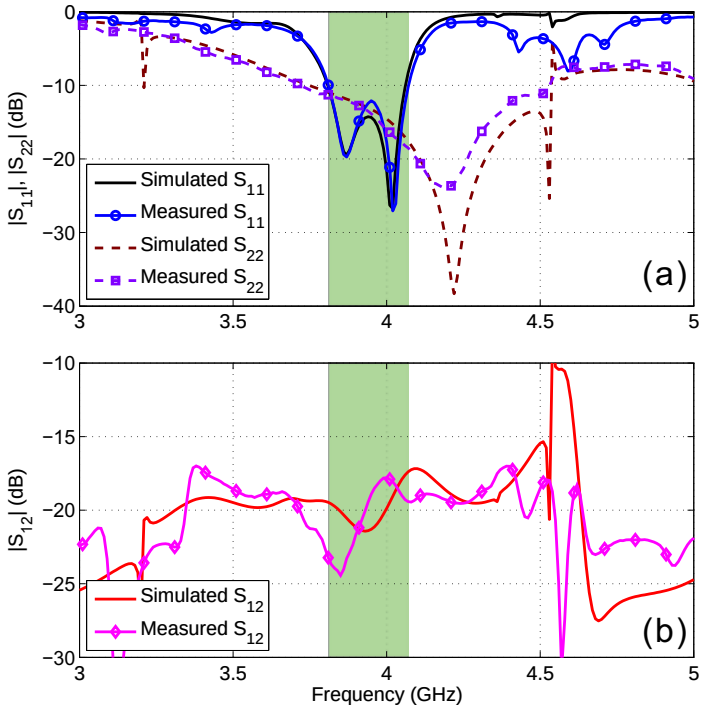

Figure 6.13. Simulated and measured magnitude of the antenna reflection coefficient for both ports (a) and inter-port coupling coefficient (b).

between these two ports is well below -15 dB in the overlapping band. The mutual coupling mainly results from coupling between the feeding networks of these two ports, printed on the bottom of substrate, as shown in Fig. 6.2(c). Thus, the mutual coupling can be further reduced by increasing space between these feeding lines. In this case, the diameter of the DR will be increased and consequently the height of DR should be reduced to resonance at the same frequency.

6.3.2 Radiation pattern and gain

Omnidirectional radiation patterns are measured in the overlapping band of the two ports. The radiation patterns at the centre of the band (3.93 GHz) are shown as illustrative example in the following. Fig. 6.14 depicts simulated and measured radiation patterns of Port 1 in the XZ and YZ plane. An omnidirectional horizontally polarized conical pattern is obtained with measured co-polarization levels at least 15 dB higher than the cross-polarization levels in both planes. Symmetric patterns and low cross-polarization are obtained because of the symmetry of the eight-arc feeding network. For Port 2, vertically polarized electric-monopole-like radiation patterns are achieved as shown in Fig. 6.15 at 3.93 GHz. The patterns shown in the XZ and YZ plane have

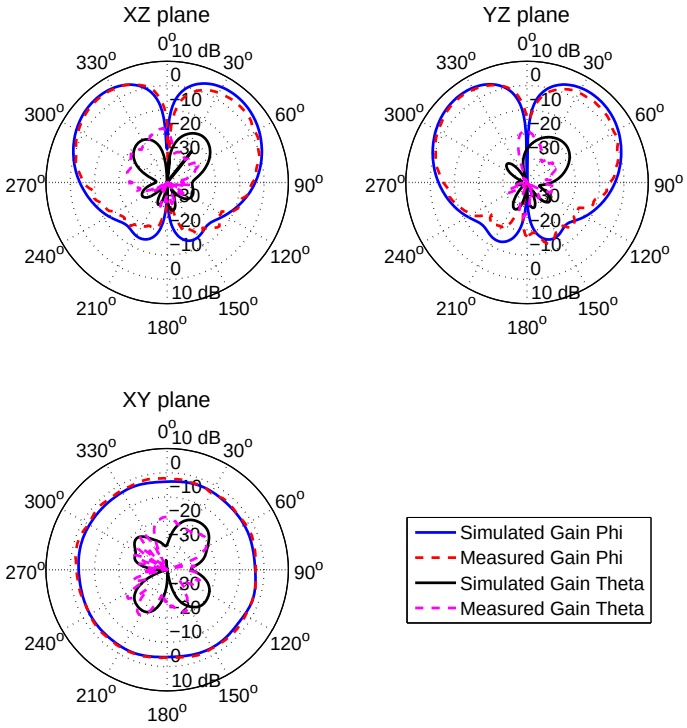

Figure 6.14. Simulated and measured radiation pattern of Port 1 (HP) at 3.93 GHz.

cross-polarization levels below -20 dB. The patterns of Port 1 and 2 in the XY plane shows omnidirectional characteristics. In the overlapping band, the average gain at $\theta = 45^o$ is in the range of 5.1 to 5.3 dB for the horizontally polarized pattern, and between 1.7 and 2.1 dB for the vertically polarized one. The gain difference of Port 1 and 2 results from the fact that the $TE_{01\delta}$ mode (Port 1) is a vertical magnetic dipole at a certain distance from the ground plane, whereas the $TM_{01\delta}$ mode (Port 2) is a electric monopole vertically located on the finite-size ground plane. The maximum gain of the conical pattern of Port 1 and 2 is shown in Fig. 6.16. A good agreement between simulation and measurement is observed. Within the frequency range from 3.78 to 4.07 GHz, the gain of Port 1 (horizontal polarization) remains above 5 dB with a maximum of 5.4 dB. The gain of Port 2 (vertical polarization) is in the range of 3 to 3.7 dB at the operational bandwidth.

6.3.3 Diversity

The overlapping working bandwidth for both modes suggests the application of the proposed antenna as a diversity or MIMO antenna. To evaluate the diversity characteristics and MIMO performance of the proposed device, the envelope correlation

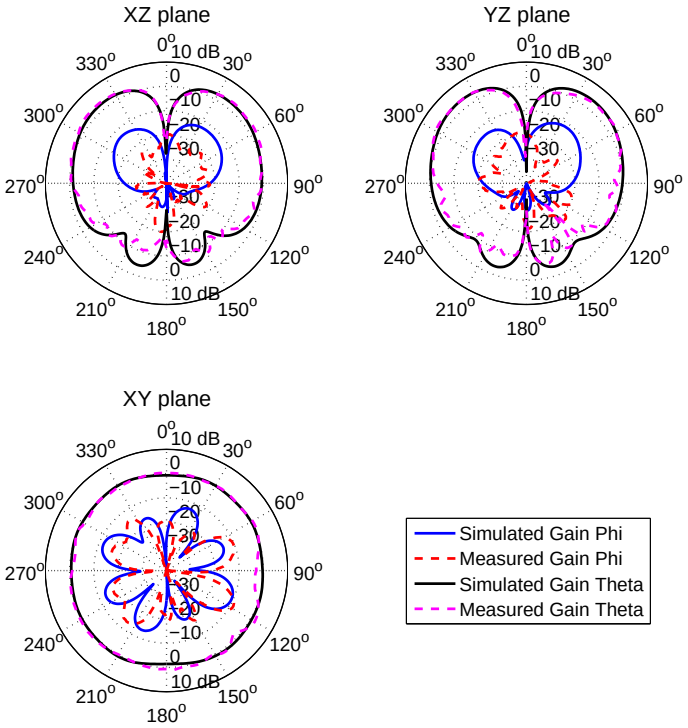

Figure 6.15. Simulated and measured radiation pattern of Port 2 (VP) at 3.93 GHz.

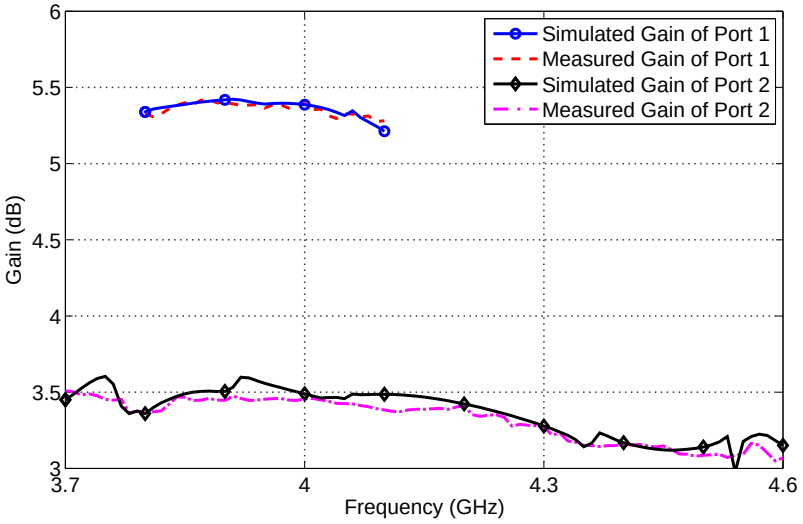

Figure 6.16. Simulated and measured maximum gain of the conical pattern of Port 1 and 2.

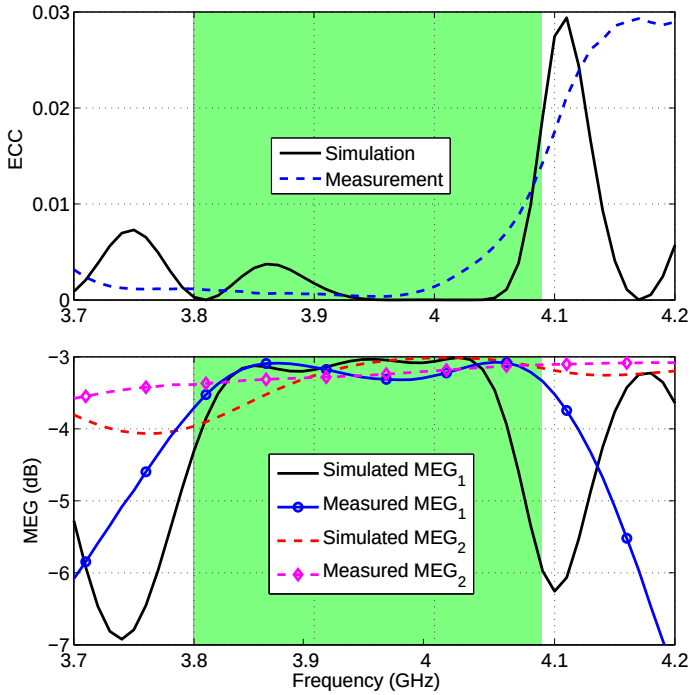

Figure 6.17. Simulated and measured envelope correlation coefficients and mean effective gain.

(ECC) [102] and mean effective gain (MEG) [98] are calculated using S-parameters for both simulation and measurement results. The detailed explanation of ECC and MEG and the corresponding calculation method can be found in the Section 4.3.4. The calculated results in Fig. 6.17 satisfy the criteria of low correlation (ECC $<$ 0.5) and comparable average received power (MEG_1 and MEG_2 $>$ -10 dB, $|MEG_1\text{-}MEG_2|$ $<$ 3 dB). Thus, a good diversity performance of the proposed antenna can be expected.

6.4 Conclusion

This chapter has proposed a dual-mode annular cylindrical DRA able to operate simultaneously with horizontally and vertically polarized omnidirectional radiation characteristics. The horizontally polarized radiation patterns is achieved by exciting the $TE_{01\delta}$ mode of the DR, with an impedance bandwidth increased to 7.4% by using an air gap and four sets of double microstrip feeding arcs. In contrast, the omnidirectional $TM_{01\delta}$ radiating mode yields a vertically polarized monopole-type radiation pattern. By exploiting the hybrid monopole-DRA structure, the bandwidth of the $TM_{01\delta}$ mode

is increased to 19.1% and overlaps with the bandwidth of the $TE_{01\delta}$ mode. The calculated ECC and MEG indicates a good diversity performance across the common band from 3.78 to 4.07 GHz.

Chapter 7

On the scaling of DRAs from microwave towards visible frequencies

THE efficiency of conventional resonant metallic antennas decreases significantly with increasing frequency in the millimeter wave frequency range. Recent research has exploited the absence of intrinsic conductor loss of dielectric resonators (DRs) for the realization of high efficiency dielectric resonators antennas (DRAs) in this spectral range. Based on this fact, the optical DRA concept is proposed as a prominent extension to the current DRA research. To scale DRA from microwave towards visible frequencies, a generic scalable DRA model is firstly proposed in this chapter. One of the critical issues is that the properties of a metallic ground plane are largely different from a perfect electric conductor (PEC) at optical frequencies. Therefore, the approaches for modeling metals in different spectral bands are considered in the second part. Combining the scalable geometry and the material models, the field distributions and the scaling behaviour are studied next, at frequency ranges from microwave to visible spectrum. The simulated field distributions in the final section confirm the excitation of the fundamental mode at optical frequencies. Based on these results, reflectarrays of optical dielectric resonator nano-antennas are designed in the next chapter.

7.1 Introduction

Millimeter-wave (MMW) transmission, especially in the unlicensed spectrum around 60 GHz, permits high data rates for future wireless personal area network (WPAN) systems. Indeed, MMW systems have appealing features for an extensive range of applications such as high definition (HD) video streaming, imaging, sensing and multi Gbps WAN. However, compared to lower bands, signals in this band are extremely prone to atmospheric attenuation and the efficiency of conventional metallic structure antenna deteriorates significantly due to the inherent conductor losses [126]. These losses have to be compensated by increasing the transmitter or receiver antenna gain. Furthermore, the small size of the MMW antennas also results in their effective area being small, which also has to be compensated by antenna gain [126]. Therefore, high gain MMW antennas have become key components in system implementation.

When the dielectric resonator antenna (DRA) was firstly proposed by Long et al. in the 1980s [5], it was predicted that the device had the capacity of providing efficient radiation for future applications in the MMW frequency region. The prediction was later proved experimentally through comparison of a DRA with a conventional microstrip antenna at 35 GHz [11]. In particular, it has been shown that a DRA exhibits a wide impedance bandwidth of 15.6% and high radiation efficiency (>90%) with negligible dissipation loss, whilst the performance of conventional metallic antennas rapidly degrades with impedance bandwidth of only 2.6% and radiation efficiency of around 80%. Furthermore, Yang et al. [127] mentioned to use resonant dielectric elements to eliminate conductive loss in a study of effects and models of material loss in infrared reflectarray design.

Several high performance MMW DRA designs have been studied and reported in the literature. A 60 GHz hybrid circularly polarized microstrip/elliptical dielectric ring resonator antenna was realized by using a reversed T-shaped coupling slot in [128]. Perron et al. proposed a hybrid DRA, with a high gain of 11.9 dB, composed of a ring-shaped dielectric resonator (DR) and a circular microstrip patch fed by a resonant slot [129]. In [130], the slot coupling method was utilized to excite higher-order TE_{115} and TE_{119} modes in a MMW DRA design. The size of the DRA is increased by using these higher-order modes, which increases the effective area of the antenna and mitigates the tolerance in fabrication. In general, traditional planar feeding schemes result in a degradation of the radiation efficiency because of considerable feed conduction and radiation losses in the millimeter-wave frequency range. As an alternative feeding

method in this spectral range, the substrate integrated waveguide (SIW) and half-mode (HMSIW) can be considered. They offer the advantages of compact size, high-Q factor, low profile, and low manufacturing costs since they can be realized with conventional printed circuit board (PCB) technology. SIW-fed rectangular DRA [71] and SIW-fed rectangular DRA array [72] operating at 37 GHz were realized using standard PCB processes. In [75], a 60 GHz linearly polarized and a circularly polarized HMSIW-fed DRAs were achieved by applying a transverse rectangular slot and cross-shaped slot, respectively. The wide bandwidth, minimal gain of 5.5 dB and high radiation efficiency of above 80% indicate the high performance of DRAs at the MMW range.

The current researches on DRA mainly focus on microwave and MMW range. Inspired by the fact that DRAs demonstrate high radiation efficiency due to the absence of intrinsic conductor loss at MMW frequencies, we propose to extend the concept of DRA from radio-frequencies towards the infrared and visible parts of the spectrum, where nanoscale metallic antennas suffer from large metallic absorption resulting in low radiation efficiency. An attempt to illustrate optical DRA by using the Yagi-Uda geometry at 10.7 GHz was found in [131]. The same geometry was also numerically analyzed in [132].

A DR is typically mounted on a metal surface or a substrate with backside metallization. At radio frequencies, the metal layer can be regarded as a perfect electric conductor and acts as an electrical symmetry plane. However, metals are not perfect conductors and involve plasmonic effects at optical frequencies. As a result, the antenna scaling property is not valid and the classical skin-effect model becomes unsuitable towards the optical frequencies. Therefore, it is important to employ suitable approaches to model metal properties since the accuracy and simulation expenditure of full field simulation tools are highly dependent on the correct characteristics of materials.

The rest of this chapter is organized as follows. Section 7.2 reviews three well-known approaches for modeling metal at room temperature, i.e. the skin-effect model, modified relaxation mode, and Drude model. In Section 7.3, a scalable DRA model is built for the investigation of the scaling behaviour. The DRA model is simulated in the commercial full field simulation software HFSS. In Section 7.4, the scaling behaviour of DRAs is studied from microwave to visible spectrum. In Section 7.5, the suitable band of each material modeling approach is assessed by considering both the accuracy and computational expenditure. The field distributions, shown in Section 7.6, prove the excitation of the fundamental $HEM_{11\delta}$ mode in the cylindrical DR at optical frequencies.

This chapter investigates the fundamentals for designing optical DRAs while applying commercial electromagnetic (EM) simulation softwares into optical antenna design. The realization of optical DRA reflectarrays based on the design fundamentals will be presented in the next chapter.

7.2 Approaches for electromagnetic modeling of metal

One goal of the present study is to apply reliable commercial EM simulation software tools to optical antenna design. The standard skin-effect model for metals as used in EM simulations at microwave frequencies is only valid at low frequencies. It is essential to find the suitable EM modeling for metals at different frequencies with acceptable accuracy and low computational expenditure. In this section, three well-known approaches for modeling metal are reviewed and their accuracy and computational expenditure for the problem at hand will be examined in Section 7.5.

7.2.1 Classical skin-effect model

At low frequencies (usually below 30 GHz), only a negligible fraction of the EM wave can penetrate into metal. The electron scattering relaxation and displacement current terms can be ignored [133]. The classical skin-effect model is utilized for most purposes because of its simplicity and accuracy. The classical skin effect model surface impedance Z_0 is given by the well-known expression

$$Z_0 = \sqrt{\frac{j\omega\mu_0\mu_r}{\sigma_0}} = R_0(1+j)\,, \tag{7.1}$$

where $\omega = 2\pi f$, μ_0 is the permeability of free space, μ_r is the relative permeability of the medium, σ_0 is the intrinsic bulk conductivity at DC, and R_0 is classical skin-effect surface resistance.

7.2.2 Modified relaxation-effect model

At terahertz frequencies, the scattering relaxation has to been taken into account. Considering electron-phonon collisions, the surface impedance Z_{SR} of the modified relaxation-effect model is given by [134]

$$Z_{SR}(\omega) = \sqrt{\frac{j\omega\mu_0\mu_r}{\sigma_R + j\omega\varepsilon_0}}\,, \tag{7.2}$$

where ε_0 is the permittivity of free space. The intrinsic bulk conductivity of the metal is $\sigma_R = \frac{\sigma_0}{1+j\omega\tau}$, where τ is the phenomenological scattering relaxation time for the free electrons. τ is typically on the order of 10^{-14} s at room temperature. The displacement current term can been ignored at low frequencies (usually below 100 GHz), where Eq. (7.2) can be simplified to the classical skin-effect model in Eq. (7.1).

Figure 7.1 shows the calculated surface impedance of silver with the parameters of $\mu_0 = 4\pi \times 10^{-7}$ H/m, $\mu_r = 0.99998$, $\varepsilon_0 = 8.854187817 \times 10^{12}$ F/m, $\sigma_0 = 6.3 \times 10^7$ S/m and $\tau = 3.66 \times 10^{-14}$ s. The left and right Y axis, respectively, indicate the real and imaginary part of the silver surface impedance, i.e. the resistance and reactance.

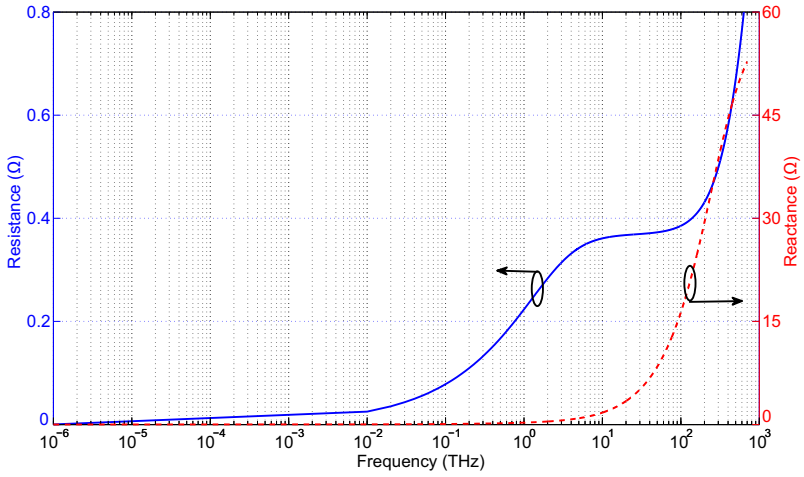

Figure 7.1. Calculated complex surface impedance of silver using the modified relaxation-effect model.

7.2.3 Drude model

As the operation frequency increases to higher frequencies and approaches the near-infrared and visible range, electric field penetration increases significantly, leading to high dissipation. This effect prohibits a straightforward scaling of structures from the microwave range. At ultraviolet frequencies and above, metal is characterized by dielectric behaviour and the penetration depth becomes larger and larger. Alkali metals such as sodium and lithium have an almost free-electron-like response and thus exhibit an ultraviolet transparency [133]. Noble metals such as gold and silver exhibit strong absorption due to the transitions between electronic bands at ultraviolet frequencies. This chapter will focus on noble metals as they are usually used in nano-technology, and in particular for fabrication of nanoantennas.

The Drude model is a classical approximation that describes a response of free electrons for materials having a spherical Fermi surface. The optical response of noble metals can be described by this means. In the Drude model, the electrons in a metal are treated as a gas. The dielectric function of the free electron gas is represented as [133]

$$\varepsilon(\omega) = \varepsilon_\infty - \frac{\omega_p^2}{\omega^2 + i\gamma\omega} \ , \tag{7.3}$$

where ε_∞ is the sum of the interband contributions (usually $1 < \varepsilon_\infty < 10$) and ω_p is the plasma frequency. The damping constant $\gamma = \gamma_1 + \beta\omega^2$ is composed of a frequency independent part γ_1 and a frequency dependent term $\beta\omega^2$. The model is valid up to the plasma frequency ω_p, which is in the ultraviolet frequency range for most metals. An extension of the model describe the behaviour above the plasma frequency is not considered here, as the ultraviolet regime is beyond the scope of this work. A detailed discussion can be found in [135].

The parameters of Drude model found in the literature may differ between different sources, as the exact properties depend on the density of the film, the grain size, and the surface roughness. The density affects the strength of the interband absorption and plasma frequency ω_p. The grain size and the surface roughness dominate the damping constant γ. The parameters for silver adopted here are $\varepsilon_\infty = 4$, $\omega_p = 1.38 \times 10^{16} s^{-1}$, $\gamma_1 = 2.73 \times 10^{13} s^{-1}$ and $\beta = 5.9 \times 10^{-18} s^{-1}$ [136]. Figure 7.2 shows the complex permittivity of silver calculated by using these parameters.

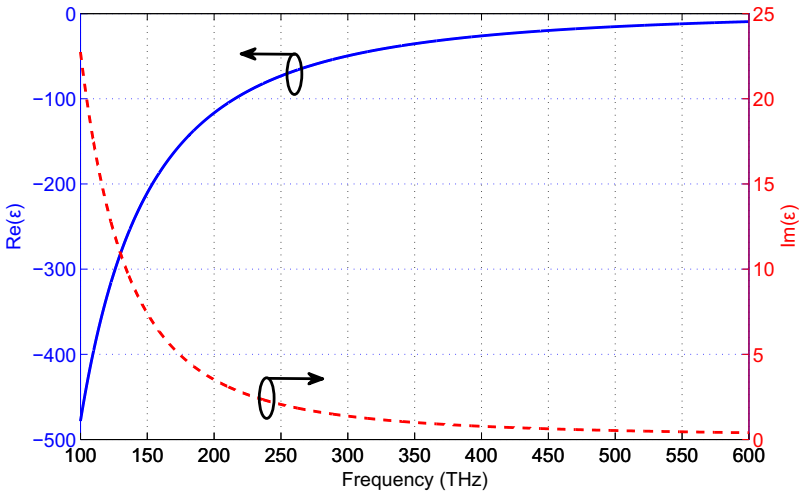

Figure 7.2. Calculated complex permittivity of silver using the Drude model.

7.3 A scalable DRA model

Generally, all EM devices can be scaled with respect to the wavelength for operation at different frequencies, provided that the material properties are constant. For the scaling of DRAs, as the operation frequency approaches infrared and visible frequencies, the straightforward scaling fails because the penetration of EM fields into the metal ground can no longer be neglected and collective oscillations resonances must be considered. Therefore, the standard engineering formulas for calculating the resonance frequency of DRs [7] are not valid in this case. Thus, numerical analysis is required to estimate the resonance frequency and study the scaling behaviour from the microwave to visible spectrum. This is investigated in the following with a generic DRA model.

The proposed scalable DRA model is illustrated in Fig. 7.3. A cylindrical DR is mounted on a silver block with a size of $1.5\lambda_0 \times 1.5\lambda_0$ and a thickness of $\lambda_0/3$. The height of the DR is fixed to $\lambda_0/10$ and the resonance is achieved by varying the diameter D of the DR. The scaling behaviour is characterized by considering the ratio of the DR diameter to the wavelength. The dimension of the DR and silver plane are expressed in wavelength as this is most appropriate for the investigation of the scaling behaviour. The lateral size of the silver plane is chosen to be larger than one wavelength to minimize edge diffraction effects while keeping the computational cost reasonable. Considering the manufacturability of optical antennas, the DR material is selected as having the same permittivity as TiO_2 (Titanium dioxide) at the frequency of operation of a red HeNe laser. The choice of this material will be elaborated in the next chapter. The DR material has then a frequency-independent anisotropic dielectric permittivity of 8.29 (in X and Y axis direction) and 6.71 (in Z axis direction) and an estimated loss tangent of 0.01 [137].

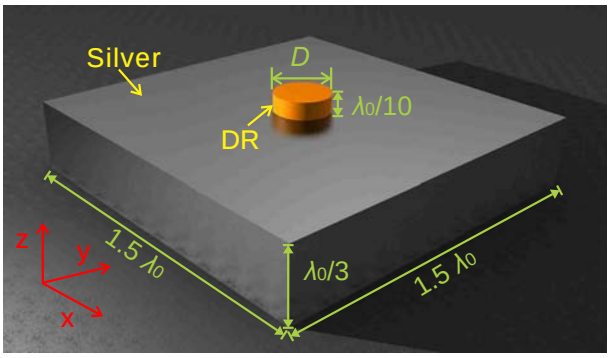

Figure 7.3. 3D sketch of the proposed scalable DRA model.

The general aim of the study is to implement the concept of nanometer-scale DRs operating in their fundamental mode as optical antennas. There are three fundamental modes, $HEM_{11\delta}$, $TM_{01\delta}$ and $TE_{01\delta}$, in a cylindrical DR. To minimize the effect from feeding components, the $HEM_{11\delta}$ is selected in this study, because it can be readily excited by a plane wave. The TiO_2 DRA model on a silver block is simulated by using HFSS, employing the radiation boundary and plane wave excitation, as shown in Fig. 7.4. In all the simulations, the electric field of the plane wave is in the X axis direction.

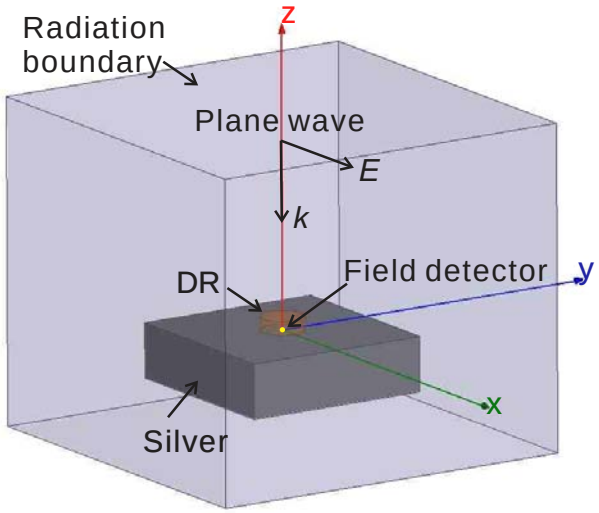

Figure 7.4. 3D HFSS model of the proposed scalable DRA model.

A DR model on a PEC is also built as a reference, by replacing the silver substrate with a PEC. The magnetic and electric field distributions of the DR-PEC model are shown in Fig. 7.5. According the the field distribution of the $HEM_{11\delta}$ mode in Fig. 7.5(a), the maximum magnetic field is located at the bottom centre of the DR, i.e. just above the silver plane. Thus, a field detector is placed at this location where the phase of the magnetic field along the Y axis is monitored, allowing to identify the resonance frequency at the maximum of the magnetic field amplitude.

7.4 DRA scaling behaviour

The operation frequency of most microwave DRs can be scaled by changing the resonator size. However, the penetration of radiation into the metal cannot be neglected in the near-infrared and visible parts of spectrum. Consequently, the antenna scaling is not applicable in these high frequency ranges. In this section, the $HEM_{11\delta}$ mode of the

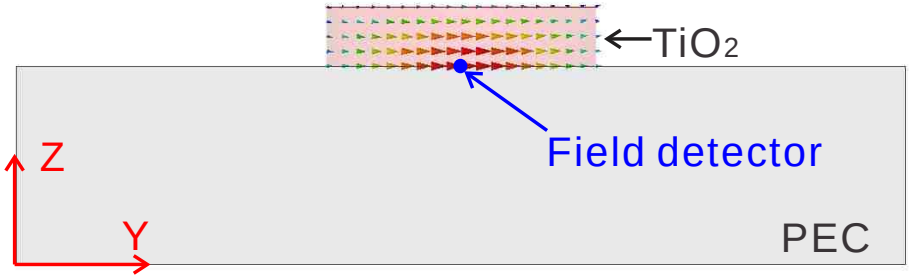

(a) H-Field distribution.

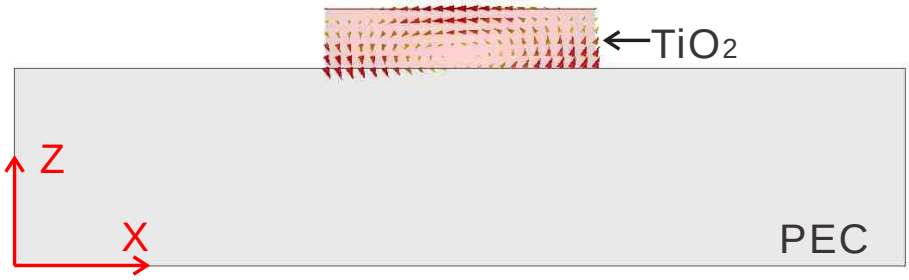

(b) E-Field distribution.

Figure 7.5. Field distribution in the cylindrical DR mounted on a PEC block.

proposed scalable cylindrical DRA model in Section 7.3 is simulated in HFSS to study the scaling behaviour.

The DR-on-PEC model is firstly simulated from microwave to visible frequencies as a reference. In Fig. 7.6, the black line indicates the expected constant relation of the ratio of the DR diameter to wavelength (D/λ_0) as a function of frequency when the PEC block is used in the scalable cylindrical DRA model.

In Fig. 7.6, the blue curve presents the resonant DR diameters obtained by replacing PEC with the frequency-dependent complex surface impedance of silver, given in Fig. 7.1. The divergence of the black and blue curves is due mainly to the increasing penetration of the field into metal. From the graph, it appears that it is inappropriate to describe silver as PEC in the frequency ranges above 1 THz.

In Fig. 7.6, the red curve shows the analyzed DR diameters when the silver permittivity values in Fig. 7.2, as calculated with the Drude model, is utilized in the HFSS simulation. The analysis is only conducted at the near-infrared and visible frequencies (i.e. from 200 to 600 THz) due the heavy computational expenditure below 200 THz, which will be explained in Section 7.5.

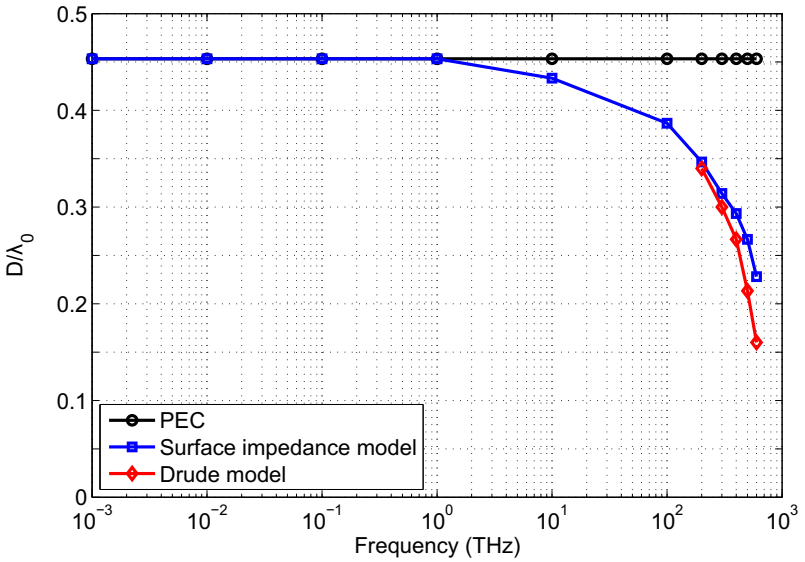

Figure 7.6. Scaling behaviour of a cylindrical DRA from microwave to visible frequencies.

The divergence of the red and blue curve indicates that it is inappropriate to apply the modified relaxation-effect model in the visible frequencies. However, the resonant DR diameters obtained using the Drude model are in good agreement with those found using the surface impedance model at near-infrared frequencies, i.e. at around 200 THz. The transition between these two models and PEC can be physically well explained by different field penetration and dispersive properties of silver at the microwave and visible frequencies. The combination of these two models to cover the full frequency range and their partial overlap in the range of common validity provides confidence in the accuracy of the results. These findings on the effect of the metal on the scaling properties of the resonance provide a practical and effective method for bringing DRA towards optical frequencies. In addition, it can be shown that the plasmonic effects have significantly reduced the DR diameters.

7.5 Computational accuracy and expenditure

The mesh-based EM simulation software, like HFSS, regard the silver block as a 2D structure, i.e. only generate mesh on the surface, when the silver is characterized by frequency-dependent complex surface impedance. This will significantly reduce the computational expenditure in the terms of CPU time and memory requirements. The

surface impedance model has acceptable accuracy with low computational expenditure below the near-infrared spectrum. However, the model is too simple to describe the penetration of EM fields into the silver block in the visible frequencies.

Using the Drude model, the mesh will be generated in the 3D silver block in EM simulation software to describe the penetration of EM fields. Generally, the field variation is rapid in materials with large negative permittivity. Consequently, a mesh-based simulation software, like HFSS, needs a fine mesh to simulate the material behaviour when volumes are discretized. The real part of the silver permittivity becomes a larger negative number as the frequency becomes lower, as shown in Fig. 7.2. Figure 7.7(a) and (b) show the generated tetrahedra by HFSS in DRA models resonance at 200 and 600 THz, respectively. The silver permittivity is $-116.5975 + j0.0301$ and $-9.3997 + j0.3951$ at 200 and 600 THz, respectively, as obtained from Fig. 7.2. In Fig. 7.7, it is obvious that the mesh density of the DR is similar. On the contrary, the metal properties being different, the automatic mesh refinement in HFSS results in a much finer mesh (relatively to the wavelength) in the silver with large negative permittivity at 200 THz. Therefore, the overall number of tetrahedra is significantly increasing when the frequency decrease towards the near-infrared spectrum, as shown in Fig. 7.8, because of the required high density in the Drude silver layer. A simulation of the scalable model at 100 THz requires more than 8 GB of memory in HFSS because of the extreme mesh refinement required, and therefore results are not given below 200 THz. The cross

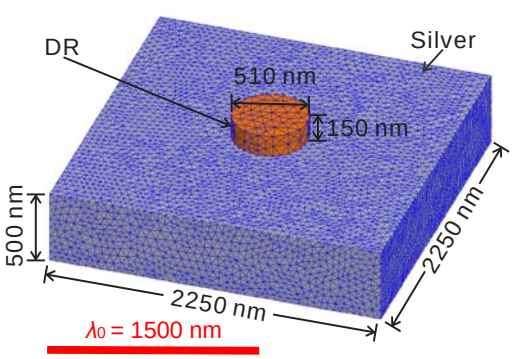

(a) Mesh plot of a DRA resonance at 200 THz.

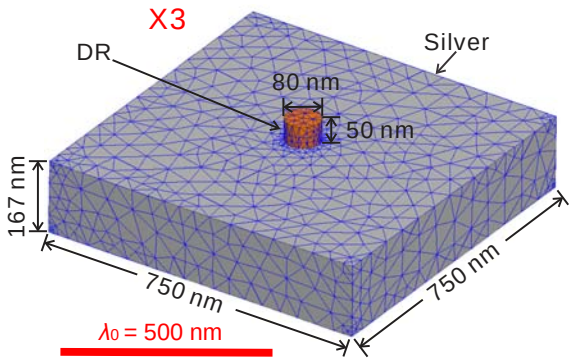

(b) Mesh plot of a DRA resonance at 600 THz. The picture is enlarged three times compared to (a).

Figure 7.7. Mesh plot of DRAs simulated in HFSS.

section view of the DRA model in Fig. 7.9 reveals that the E-field decays slower in

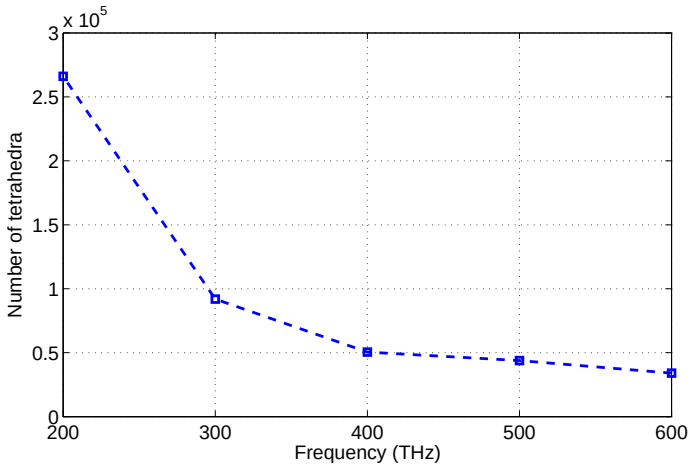

Figure 7.8. Number of generated tetrahedra for the resonant DRA models at different frequencies. The DRA models are simulated in HFSS using the Drude model for the silver layer.

the left-hand side picture Fig. 7.7(a) (with large negative permittivity) than that in the right-hand side picture Fig. 7.7(b) (with small negative permittivity). For the sake of comparison, the picture of the 600 THz DRA model are enlarged 3 times compared to the pictures at 200 THz. But it is emphasized that dimension of the silver block and height of the DR in the enlarged Fig. 7.9(b) are equal to the corresponding values in Fig. 7.9(a) since they are proportional to the wavelength. The difference in DR diameter to achieve resonance illustrates the non-trivial scaling behaviour due to the plasmonic effect.

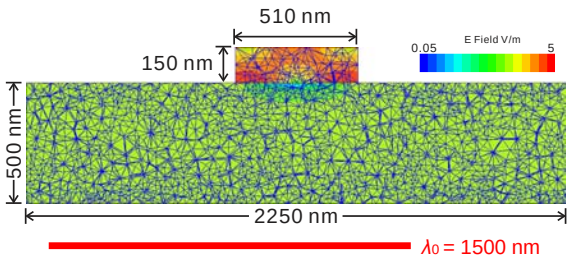

(a) A DRA model resonance at 200 THz.

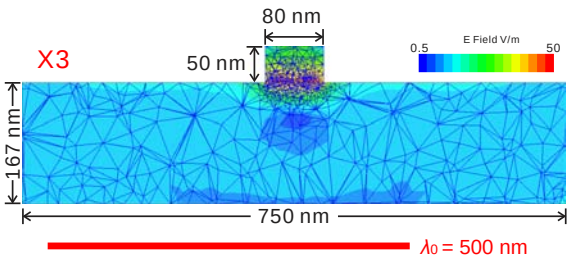

(b) A DRA model resonance at 600 THz. The picture is enlarged three times with respect to (a).

Figure 7.9. The cross section view of the E field amplitude and mesh.

7.6 Excitation of the fundamental mode at optical frequency range

The TiO_2-Silver DRA model is simulated at 500 THz to verify the excitation of the fundamental $HEM_{11\delta}$ mode in the cylindrical DR. The complex permittivity of silver at 500 THz is $-15.2956 + j0.5253$, which is obtainable from Fig. 7.2. Figure 7.10(a) illustrates a sharp resonance at approximately 500 THz with a DR height of $\lambda_0/10$ = 60 nm and a diameter of D = 128 nm. The curve in Fig 7.10(b) shows a wide range of phase variation around the resonant frequency. Figure 7.11 shows the magnetic and electric field distributions at resonance frequency. The field distributions confirm the excitation of the fundamental $HEM_{11\delta}$ mode in the cylindrical DR. Compared with field distributions in Fig. 7.5, the electric field extends into in the silver block as shown in Fig. 7.11(b) due to the plasmonic effect.

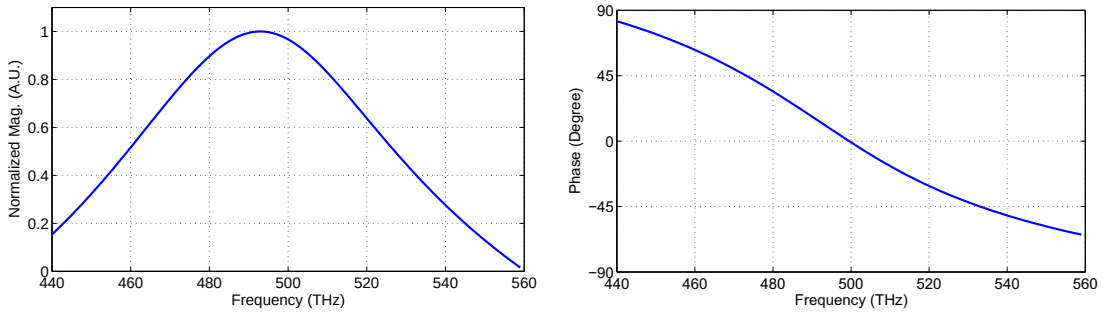

(a) Magnitude of the magnetic field.

(b) Phase of the magnetic field.

Figure 7.10. Magnitude and phase of the Y-component direction magnetic field at the probe location.

7.7 Conclusion

In this chapter, a scalable DRA model is built to study the scaling behaviour of a DRA from microwave to visible spectrum. The scaling behaviour study is a fundamental investigation for bringing the concept of DRA to the visible spectrum. Commercial EM simulation software (in the present case HFSS) is applied for optical antenna design, with particular care of using appropriate material models across the different frequency scales.

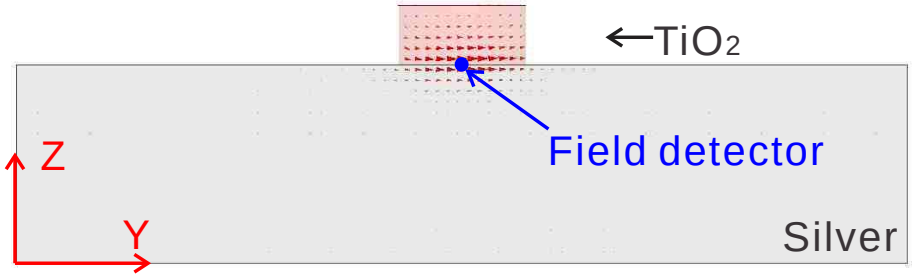

(a) H-Field distribution.

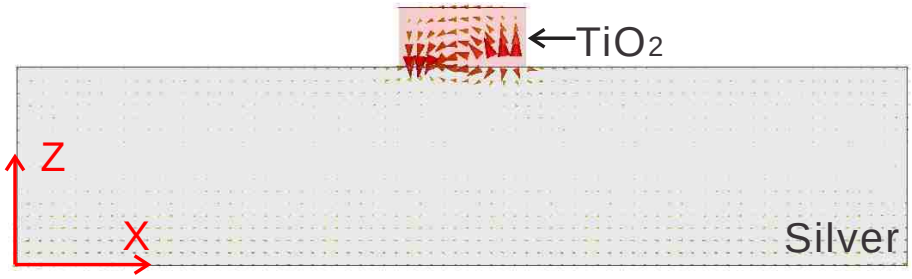

(b) E-Field distribution.

Figure 7.11. Field distributions in the cylindrical DR and silver excited by a wavelength of 500 THz incident plane wave.

Since the standard skin-effect model of metal is only valid at low frequency, the modified surface impedance model is employed to describe the silver permittivity. It has been shown that the surface impedance model has acceptable accuracy with low computational costs below the near-infrared spectrum. In contrast, the Drude model provides a more accurate description of the field penetration and dispersive properties of metal at optical frequencies. However, the large negative permittivity of silver described by Drude model leads to a fine mesh requirement and hence increases the computational cost in mesh-based EM simulations. This limits the Drude model application to near-infrared and visible frequencies. The transition and overlap of these two models validate this practical method of characterizing metal properties from microwave to optical frequencies.

The field distributions confirm the excitation of the fundamental $HEM_{11\delta}$ mode in the cylindrical DR at 500 THz. Although the excited $HEM_{11\delta}$ mode for the DR in the optical frequency range has a similar field distribution as its counterpart in the microwave frequency range, the electric field extends into in the silver block due to the plasmonic

effect and thus significantly reduces the DR size. Based on these results, reflectarrays of optical dielectric resonator nano-antennas are designed in the next chapter.

Chapter 8

Optical reflectarray of dielectric resonator nano-antennas

CONVENTIONAL plasmonic nanoantennas suffer significant energy dissipation introduced by Drude metals in the optical frequency range. To overcome this limitation, the proposed concept of optical dielectric resonator antenna (DRA) is implemented in this chapter and validated through a realization of optical DRA reflectarrays. The manipulation of light with manufactured dielectric resonator nano-antenna reflectarrays is demonstrated through deflection of a beam at various angles off specular direction.

8.1 Introduction

The concept of optical antenna describes resonant devices able to convert propagating radiation into localized energy and vice versa, as inspired by antennas commonly encountered at radio frequencies. Stimulated by advanced nanofabrication techniques, optical antennas provide an effective method to concentrate and manipulate light at subwavelength scales. They have attracted applications in many fields, including light-emitting devices, sensors, on-chip communications, optical components, photovoltaics and spectroscopy [138].

Driven by these applications, the research on optical antennas has become one of the active fields in physical optics. The optical antenna research to date mostly focuses on resonant metallic nanostructures [138, 139]. To enhance the antenna performance, well-known microwave antenna shapes like dipole [140, 141], monopole [142], Yagi-Uda [143, 144], spiral [145], patch [146] and bow-tie [147] have been recently successfully realised at optical frequencies. However, the plasmonic effect adversely affects the radiation efficiency of optical antennas because of the high ohmic loss at optical frequencies [133].

In the previous chapter, the concept of optical dielectric resonator antenna (DRA) has been proposed and the simulation result of a 500 THz DRA has confirmed the excitation of the fundamental $HEM_{11\delta}$ mode in a cylindrical dielectric resonator (DR). Furthermore, the scaling behaviour of DRA on a silver plane has been examined from microwave to visible frequencies. Based on these study and analysis, the reflectarray principle [148] is utilized to experimentally demonstrate the performance of optical DRAs. The array principle has been successfully employed for various metallic nanoantennas study [149–152]. The reflectarray configuration eliminates the need for integrated feeding components and thus is suitable for studying the fundamental optical DRA properties.

Several variations of optical DRA reflectarrays for operation at 633 nm visible red light are designed and fabricated in this study. The proposed optical DRA reflectarray provides a platform for indirectly evaluating the function of optical DRs through observation of a predefined far-field beam angular deflection. The deflection angle for the reflected beam is manipulated by using a periodic arrangement of cylindrical DRs subarrays, with various diameters appropriately selected around the dimension of the resonant fundamental $HEM_{11\delta}$ mode.

The rest of this chapter is structured as follows. The detailed design procedure for DRA reflectarray with 4, 6 and 9-element subarrays is presented in Section 8.2. The nanofabrication process is briefly described in Section 8.3. The measurement setup and results are shown in Section 8.4. The optical properties of silver is measured in Section 8.5. Based on the measured silver properties, the improved design and its measurement results are provided in Section 8.6 and 8.7, respectively. Section 8.8 investigates the dissipation loss of DRs at optical frequencies. A grating reflector is simulated in Section 8.9 to demonstrate that beam shaping cannot be achieved without a resonance mechanism within the optical DRs.

8.2 Optical DRA reflectarray design

The reflectarray is a type of antenna that combines advantages of reflector antennas and phased arrays [148]. A reflectarray is usually manufactured on a planar substrate and offers beam shaping as a phased array. The design and manufacture cost of a planar reflectarray is much less than a parabolic reflector antenna, which has high tolerance requirement on the reflecting surface. On the other hand, the feeding mechanism of a reflectarray is similar to that of a reflector antenna, which eliminates the complex feeding network used in phased arrays.

To the best of our knowledge, the current research of dielectric resonator reflectarray is restricted to the microwave frequency range. In some designs, a variable phase shift is achieved by varying the dimension of the DRs [153–155]. Jamaluddin et al. [156] proposed a DRA reflectarray composed of strip-loaded DRs to achieve dual-band or reconfigurable operation. The element reflection phase is controlled by changing the length of the strip, instead of the size of the DR itself. In further publications, aperture coupled DRA reflectarrays are introduced in order to achieve a wide bandwidth of operation, where a full 360° phase shift is obtained by varying the length of the stub-transmission line [157] or the length of slot [158]. Most of these concepts are only proposed through simulated results performed using commercial full field simulation tools, such as HFSS and CST. Measured results are provided in [155, 156] with good agreement with simulation results and show the high performance of DRA reflectarrays.

8.2.1 Design principle

Due to the lack of true nanoscale light sources and guiding channels, the reflectarray configuration offers an alternative indirect method to study the fundamental optical DRA property. By combining multiple nanoscale DRAs possessing different geometries in an array, it is feasible to reveal the response of DRAs by observing the corresponding far-field response of the reflectarray. In this study, a type of reflectarray structure is designed to impart a progressive phase shift in order to deflect the beam to a predefined deflection angle θ relative to specular reflection. The deflection angle θ can be calculated from [94],

$$\sin\theta = \frac{\phi}{kd}, \tag{8.1}$$

where $k = 2\pi/\lambda_0$, and λ_0 is the free space wavelength, d is the distance between the centre of two adjacent elements. The progressive phase shift ϕ is achieved by varying the diameter of the DR to slightly detune it from the resonance. The proposed reflectarray is designed to work at 474 THz (He-Ne lasers red light, 633 nm, 1.96 eV).

Based on manufacturability and functionality, the DR material is selected as TiO_2 (Titanium dioxide) with frequency-independent dielectric permittivity of 8.29 (in X and Y axis direction) and 6.71 (in Z axis direction) and an estimated loss tangent of 0.01 [137]. These material properties have been used in the optical model investigated in Chapter 7. The uncertainty of the loss tangent will not affect the resonance frequency of DRs and only affect the dissipation loss of DRs, which will be investigated in Section 8.8.

In the optical frequencies, the field penetration in the metal has to be taken into account and the classical skin-effect model provided by default in simulation software tools is not valid. The complex silver permittivity is calculated by using Drude model and exported to HFSS. In the simulation, the permittivity of the silver is $-17.47 + j0.57$ at 474 THz, which is obtainable from Fig. 7.5 in Chapter 7.

8.2.2 TiO_2-Silver DR array model

In the array configuration, the coupling between DRs shifts the resonance frequency of DRs from that of a single DR element. Based on the scalable DRA model in Chapter 7, a TiO_2-Silver DR array model is built to study the phase and magnitude responses of a uniform DR array as a function of the DR diameter. The array model is simulated in HFSS, employing Master & Slave boundaries and Floquet port excitation, as shown

in Fig. 8.1. A cylindrical DR with the diameter of D and height of H is located at the centre of a square silver block with the cell size of d and height of h. The cell size of d is equal to the distance between the centre of two adjacent DRs.

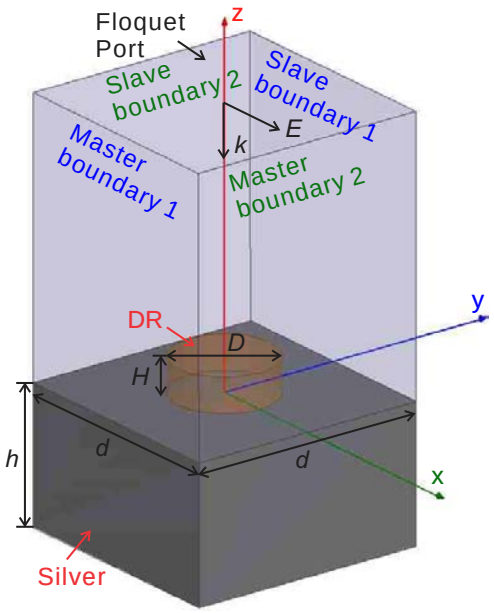

Figure 8.1. 3D HFSS model of the TiO_2-Silver DR array model.

Distance between DR centers

The simulation results in Fig. 8.2 show that the phase variation can cover almost a full 360° phase cycle, when the diameter of the DR D is varied. The three different curves in the two graphs of Fig. 8.2 also clearly indicates that the distance between the DR centers affects the coupling between DRs, which can shift the resonant frequency and influence absorption of the reflectarray structure. The strongest absorption of occurs close to the resonance frequency.

The distance between the DR centers is selected on a basis of a trade-off between different performance factors, together with the accuracy of the employed nanofabrication technique. Figure 8.2(a). shows that a small distance between DR centre leads to phase curve with less steep slope around the resonance. It means that the phase is less sensitive to a change in the diameter, resulting in an increased robustness of the design to fabrication tolerances. However, a reduction in the distance between cylindrical DR decrease the overall phase range available to the design of reflectarrays. Furthermore, it increases the chance of neighbor DRs to become merged during the fabrication process.

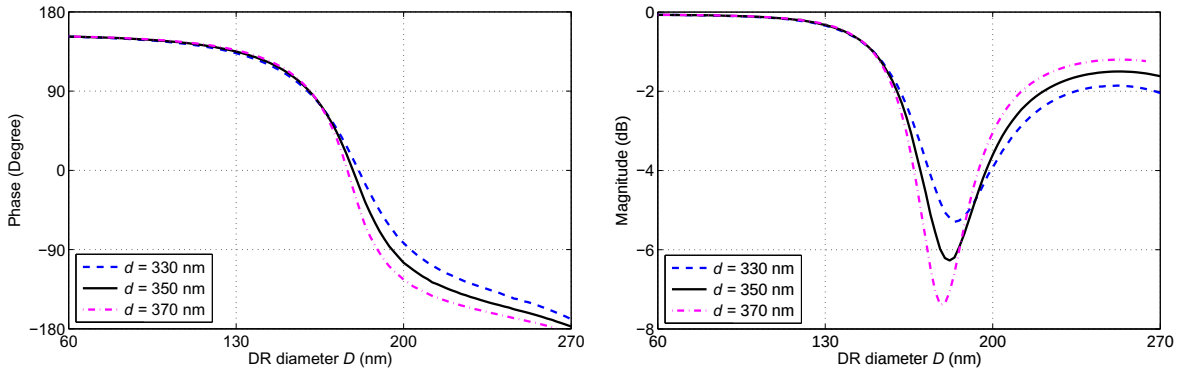

(a) Phase responses. (b) Magnitude responses.

Figure 8.2. Phase and magnitude variation of DR diameter with different distance between DR centre at 474 THz.

DR height

Variations of the DR height has a similar effect as varying the distance between DR centre, as shown in Fig. 8.3. A low DR height design results in a flatter phase curve compared to a tall DR, and hence tolerance requirements are relaxed. A drawback is that lowering the DR height requires a larger DR diameters to keep the resonance frequency constant, which increases the chance of merged neighbor DRs in the nanofabrication process. On the contrary, high DR height gives more space between DRs but leads to a sharp phase change around the resonance frequency, which increases the diameter tolerance requirement.

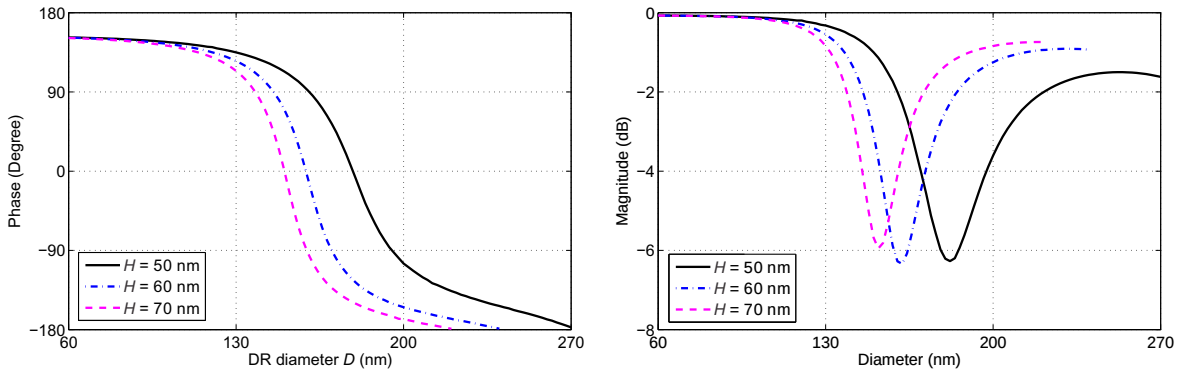

(a) Phase responses. (b) Magnitude responses.

Figure 8.3. Phase and magnitude variation of DR diameter with different DR height at 474 THz.

Table 8.1. DR diameters of 6-element subarray. The calculated angle of deflection is 17.5°

Phase (degree)	150	90	30	-30	-90	-150
Diameter (nm)	82	165	174	183	195	238

8.2.3 Six-element DRA reflectarray

By considering the performance and fabrication feasibility, the distance between DR centre of 350 nm and the height of 50 nm are selected. In the first design, a 60° progressive phase shift subarray is formed by 6 DR elements to provide a 360° phase ramp. The 6-element subarray is periodically patterned on a silver layer to form a 6-element DRA reflectarray, as shown in Fig. 8.4.

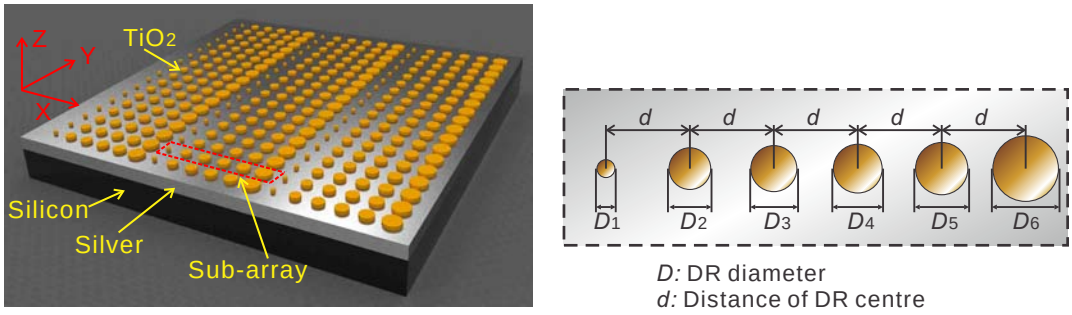

(a) 3D view.

(b) Top view of one subarray.

Figure 8.4. Partial view of 6-element DRA reflectarray.

The selected diameters of the 6 DR elements subarray are indicated with red circles in Fig 8.5. The DR diameters and corresponding phase are also tabulated in Table 8.1. The strongest absorption occurs on the resonance and amounts to -6.2 dB. According to the Eq. 8.1, the reflectarray should exhibit a deflection angle of 17.5°, if excited with a normal incident plane wave. The reversed design procedure is also valid, i.e. given a desired deflection angle, the distance between DR centre and progress phase shift can be calculated from the Eq. (8.1).

The DRA reflectarray is fabricated on a silver-coated silicon wafer with a thickness of silver of 200 nm. The silicon layer has negligible effect on the results, as shown in Fig. 8.6, since the silver layer is thick enough to block all incident radiation. Thus, the silicon layer can be neglected in the simulation. The numerical result in Fig. 8.7 demonstrates that the deflection angle is 17.5°, in good agreement with the value predicted from calculation using Eq. (8.1). It is worth to emphasize that the phase curve in

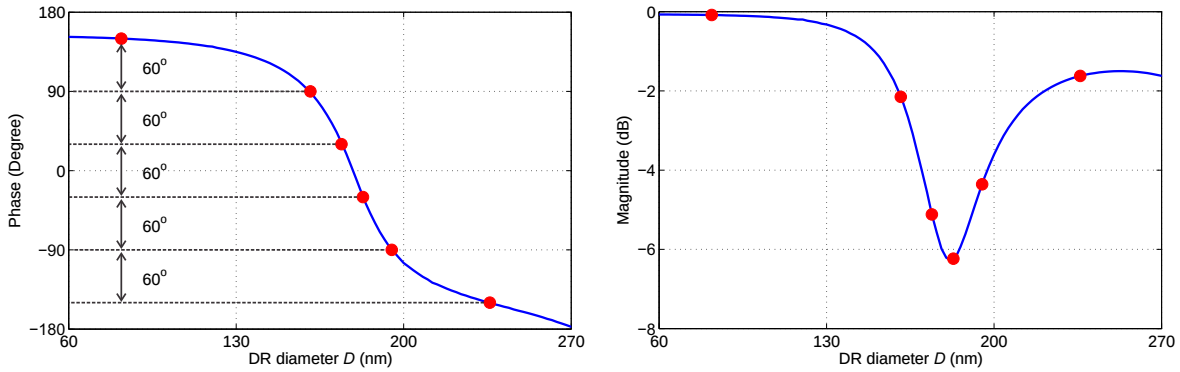

(a) Phase responses

(b) Magnitude responses

Figure 8.5. Numerically resolved phase and magnitude response of DRs with height of 50 nm at 474 THz. The distance between DR centre is 350 nm. The red circles indicate the selected cylindrical diameters for 6-element DRA reflectarray

Fig. 8.5(a) is obtained from an infinite uniform array. However, in the actual reflectarray design, the DR diameter is only identical in the Y axis direction and varies in the X axis direction to form the progressive phase change. For these non-uniform arrays, a difference in the diameter of adjacent DRs influences the inter-element coupling between DRs. This introduces, as a result, a slight phase offset for each DR, compared to the phase obtained in an infinite uniform array. Thus, the ideal progressive phase shift is perturbed, and the performance of the reflectarray is slightly degraded, particularly when the polarization of incident wave is in the Y axial direction (TM polarized wave), as shown in Fig. 8.8.

8.2.4 Four- and nine-element DRA reflectarray

In the first batch of samples, the 4 and 9-element DRA reflectarrays are also designed to achieve different beam deflection angles. To provide a 360° phase ramp, these two configurations have the progressive phase change of 90° and 40°, respectively. Given the cell size of 350 nm, the calculated deflection angles of 4 and 9-element reflectarrays are 27° and 11.6°, respectively. Since the design of the 4, 6 and 6-element DRA reflectarray follows the same procedure, only the design process of the 6-element DRA reflectarray was discussed in detail in Section 8.2.3. The 4 and 9-element arrangements are chosen for convenience because they are round numbers when dividing a full cycle of 360°. To achieve the desired angle, the number of elements in one subarray and

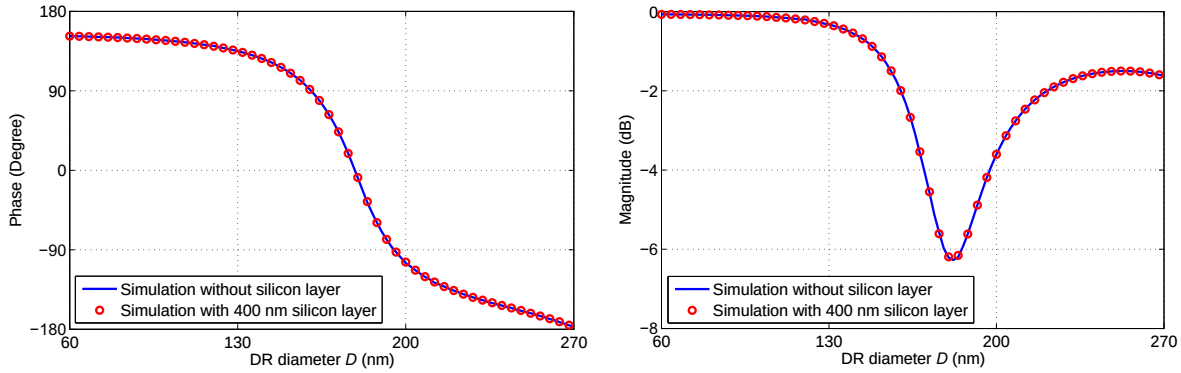

(a) Phase responses (b) Magnitude responses

Figure 8.6. Numerically resolved phase and magnitude response of DRs with and without silicon layer at 474 THz.

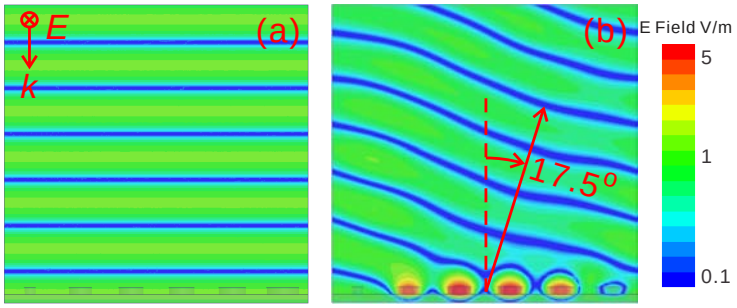

Figure 8.7. Incident (a) and scattered (b) electric fields of 6-element subarray DRA reflectarray for the TE polarized wave.

distance between each element will be chosen based on the Eq. (8.1). It is worthwhile to remark that if the elements are more than 9, the space between the largest and the second largest element is too small. They might merge during the fabrication process.

The diameters of DRs of 4 and 9-element reflectarrays are tabulated in Table 8.2 and 8.3, respectively. The simulation results indicate that the angles of the scattered field for the 4 and 9-element reflectarrays are 27.0° and 11.6° with respect to the TE polarized incident wave, which is normal to the surface, as shown in Fig. 8.9 and Fig. 8.10. For the TE polarized incident wave, the 9-element reflectarray has a better performance than 4-element reflectarray because of the small step of the progressive phase shift. Compared to the 9-element reflectarray, the 4-element reflectarray has a large difference in the diameters of adjacent DRs. Therefore, the coupling between adjacent DR differs from the coupling in a uniform array in a more pronounced way. This can affect the performance significantly, as observed for the TM polarized incident wave in

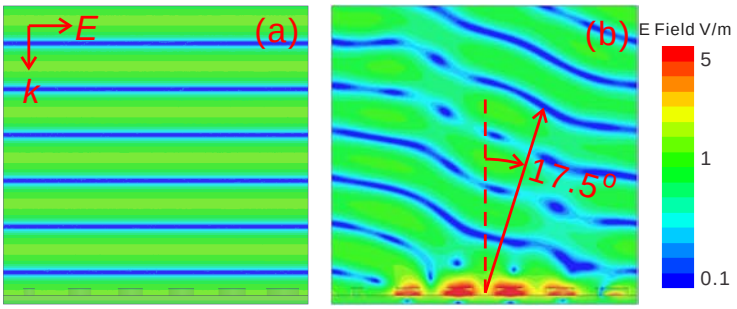

Figure 8.8. Incident (a) and scattered (b) electric fields of 6-element subarray DRA reflectarray for the TM polarized wave.

Table 8.2. DR diameters of 4-element subarray. The calculated angle of deflection is 27.0°

Phase (degree)	150	60	-30	-120
Diameter (nm)	82	169	183	208

Fig. 8.9(b). On the contrary, small adjacent DR size difference makes the 9-cell reflectarray work satisfactorily for both the TE and TM polarized incident waves.

8.3 Fabrication

Several prototypes of optical DRA reflectarrays have been fabricated in the Functional Materials and Microsystems Research Group, School of Electrical and Computer Engineering, RMIT University. Fig. 8.11 presents a schematic of the multi-stage nanofabrication process. The fabrication process is briefly described as follows:

1. A 200 nm silver layer is deposited on a silicon (100) wafer with a thickness of 390±16 μm by electron beam evaporation following pumpdown to a base pressure of 1×10^{-7} Torr.

2. High resolution electron beam resist-Poly (methyl methacrylate) or PMMA is spin-coated on the silver.

3. The PMMA resist layer of thickness of 200 nm is patterned by electron-beam direct writing in a field emission gun scanning electron microscope.

Table 8.3. DR diameters of 9-element subarray. The calculated angle of deflection is 11.6°

Phase (degree)	150	110	70	30	-10	-50	-90	-130	-170
Diameter (nm)	82	152	166	174	180	186	195	215	262

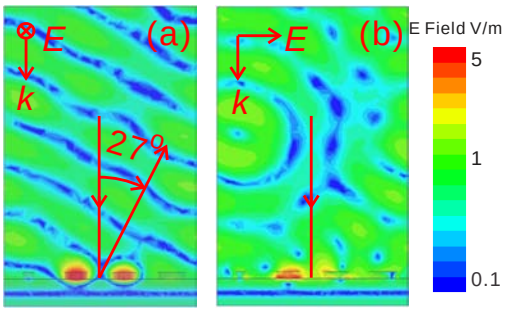

Figure 8.9. Scattered electric fields of 4 element DRA reflectarray for the TE (a) and TM (b) polarized normal incident wave.

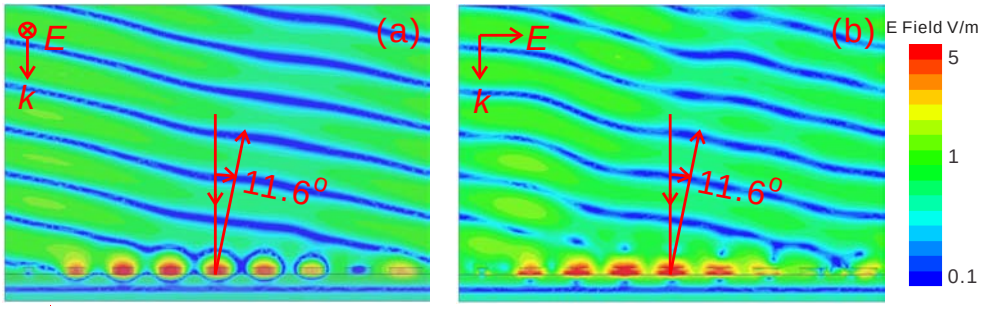

Figure 8.10. Scattered electric fields of 9 element DRA reflectarray for the TE (a) and TM (b) polarized normal incident wave.

4. The dielectric TiO_2 film of 50 nm thickness is deposited at room temperature using electron beam evaporation after attaining a base pressure of 1×10^{-7} Torr.

5. The final nanoscale structures is obtained by dissolving the sacrificial PMMA layer in acetone with ultrasonic agitation. The TiO_2 nanocylinders are annealed for two hours at 600°C in a vacuum furnace, which was pumped down to a pressure of 1×10^{-5} Torr.

The 4, 6 and 9-element DRA reflectarrays are fabricated on the same silicon wafer, as shown in Fig. 8.12. Four areas have the same reflectarray layout for redundancy. Each area contains three arrays of 4, 6 and 9-element reflectarrays, as shown in the zoomed-in picture of Fig. 8.12(c). Each array has an area of 40×40 μm^2, which corresponds to 114×114 resonators. The picture is taken by a Canon CCD camera under flashlight. Since the flashlight is white light containing all visible components, a color difference in the 4, 6 and 9-element DRA reflectarrays is caused by the different absorption and frequency dependent scattering of the reflectarrays.

Figure 8.13 shows scanning electron micrographs of partial reflectarrays. The designed and actual DR diameters and the corresponding phases are plotted in Fig. 8.14 for the

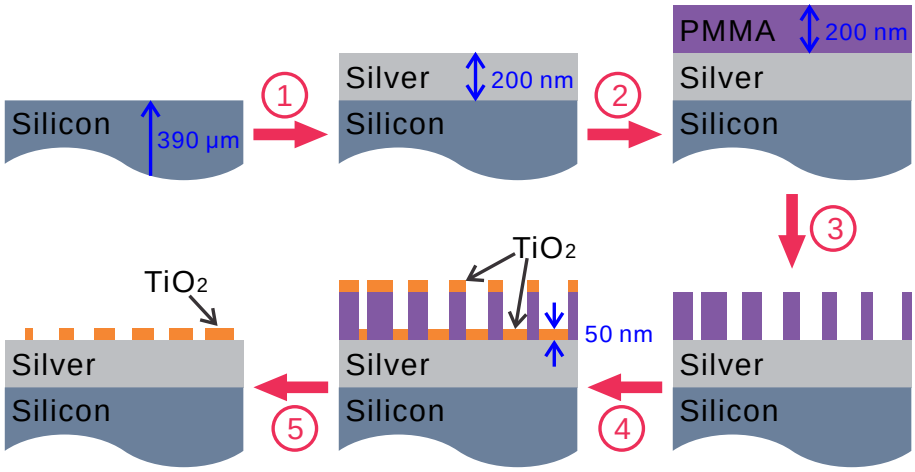

Figure 8.11. Schematic of the fabrication sequence for the optical DRA reflectarray.

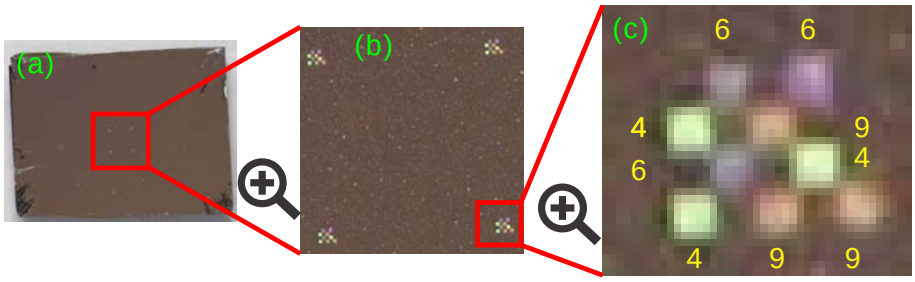

Figure 8.12. (a) Photo of fabricated DRA reflectarrays; (b) Zoomed in picture of 4 areas with the same reflectarray layout. (c) Zoomed in picture of one area. The numbers 4, 6 and 9 denote 4, 6 and 9-element DRA reflectarrays.

first fabrication run. The imperfect fabrication leads to the inaccurate DR diameters and hence offsets the corresponding phase. Figure 8.14 also reveals that the DR diameter becomes critical around the resonance. Even a small diameter difference results in a large phase offset.

8.4 First prototypes measurement and discussion

The reflection characteristics of the sample are measured under illumination by a Newport R-31007 linear polarised red HeNe laser with a wavelength of 633 nm. A microscope objective lens with a focal length of 16.5 mm focuses the beam to a diameter of less than 40 µm. To facilitate the measurement of the specular reflection and deflection, the beam is incident at an angle $\alpha = 30^\circ$ with respect to the surface normal, as shown in Fig. 8.15. A CCD camera is used for detection. It is mounted at 60 mm away from

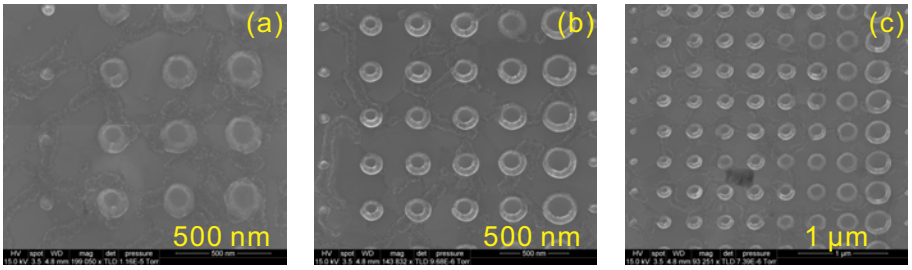

Figure 8.13. Scanning electron micrograph revealing an area on the fabricated 4, 6 and 9-element reflectarrays.

the reflectarray and positioned at an angle normal to the angle bisecting the specular reflection angle and the deflection angle θ.

Figure 8.16 shows the measured beam patterns recorded by a Canon CCD camera for both the TE and TM polarised incident waves. The specular reflection and the deflection are both clearly observed. The specular reflection component is attributed to the imperfection of the DRs, which alters the progressive phase shift and hence introduces power in the undesired spatial harmonics (also called grating lobes or Floquet modes). For the TE polarised incident wave, the ratios of the deflected to reflected beam power, recorded by a Thorlabs TM100D power meter, are 1.63, 3.24 and 3.10 for 4, 6 and 9-element arrays, respectively. As we discussed before, the performance of the reflectarray is decreased for the TM polarized incident wave. In this case, the ratios of deflected to reflected beam power are 0.50, 0.41 and 0.38 for 4, 6 and 9-element reflectarray, respectively. The second spatial harmonic is also observed from the deflected beam of the 9-element reflectarray. For both the TE and TM polarized incident waves, the measured deflected beam angles of 4, 6 and 9-element array are 27.5°, 17.8° and 11.2°, respectively. These values are very close to the theoretical expectation of 27.0°, 17.5° and 11.6° given in Eq.(8.1).

As the aperture of detector of the power meter is much larger than the reflected and deflected beam size in the previous measurement setup, the detector collects some scattered field arising from imperfections and undesired inhomogeneities in the fabricated samples. Therefore, as alternative measurement method, a Thorlabs LC100 CCD linear camera is employed to record the reflected and deflected beams of the 6-element reflectarray. This gives more information on the beam shape and allows to eliminate the effect from the scattered energy.

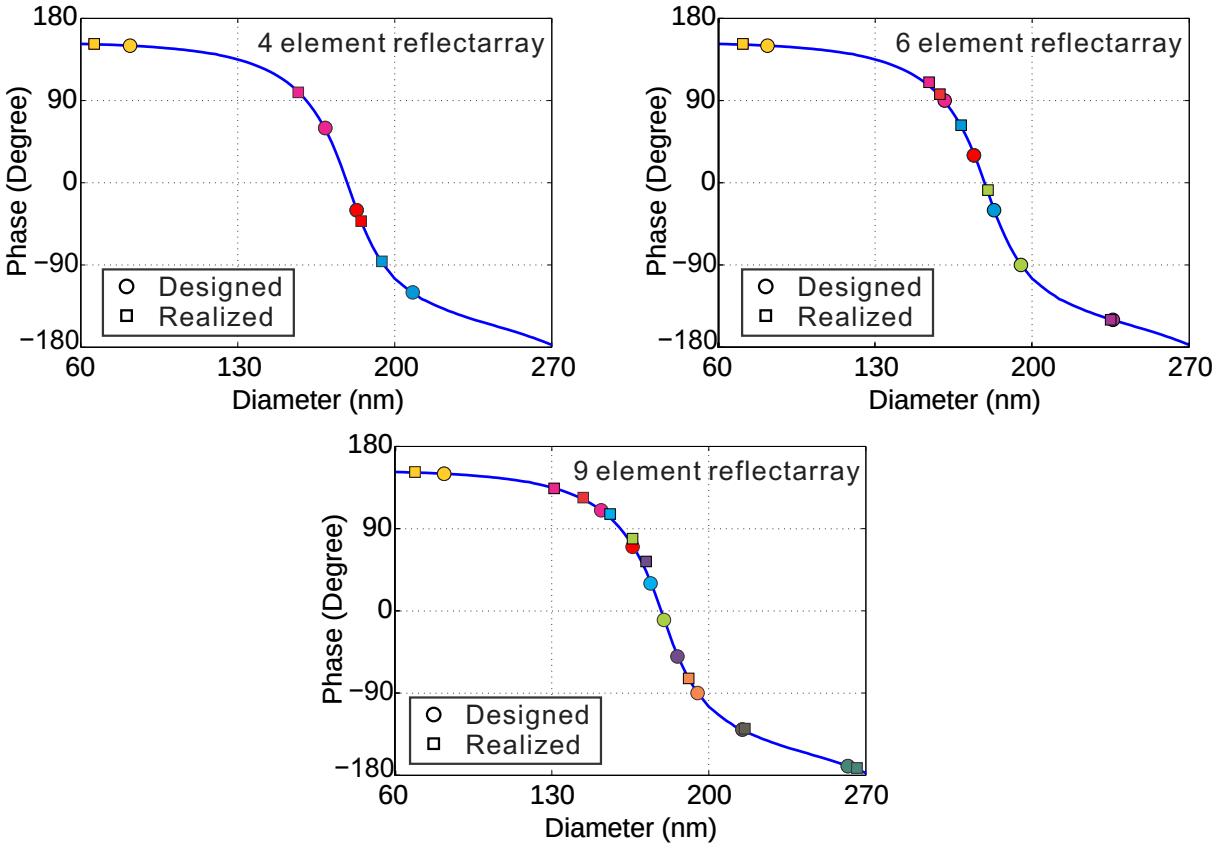

Figure 8.14. Designed and realized DR diameters of 4, 6 and 9-element reflectarrays. The different colors indicate different DR element

The linear camera incorporates a 2048 pixel CCD array with 14 μm between each pixel, thus offering a scanning length of 28.672 mm. The exported data from the camera consists of a 2×2048 matrix, with the first row listing the pixel number (denoting X axis direction) and the second row giving the measured power intensity of each pixel (denoting Z axis direction). In our measurements, the camera is attached on a translation stage moving vertically, i.e. along the Y axis direction. The data from the linear camera is recorded at every 100 μm movement of the translation stage.

The data is imported into Matlab and used to generate a 3D projected pattern, as shown in Fig. 8.17. The length scale in the X axis can be transformed to the angle scale based on simple geometry, taking into account the distance between the pixels on the CCD array and the reflectarray. The deflected beam exhibits a nearly Gaussian beam shape and exhibits a stronger power than the reflected beam. The 2D radiation pattern, shown in Fig. 8.18, is obtained from the data set with the strongest power of reflection and deflection recorded by the linear camera, i.e. the data set going through the centers of

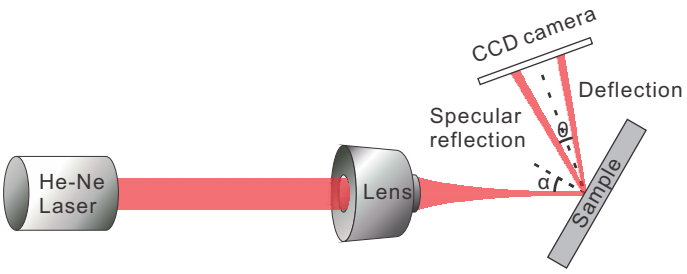

Figure 8.15. Experiment setup.

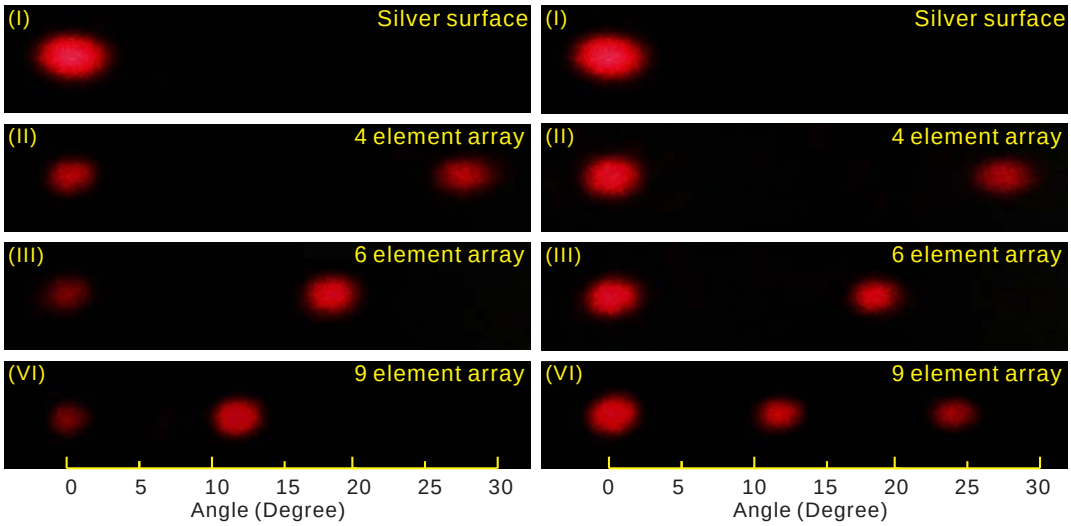

(a) TE polarized incident wave. (b) TM polarized incident wave.

Figure 8.16. Beam reflection patterns obtained from a CCD camera. Angle of 0° denotes the direction of the specular reflection.

the two observed beam, at $Y = 0$ in Fig. 8.17. The radiation pattern indicates that the angle θ between specular reflection and deflection is 17.5° as expected.

Based on the array theory [94], the beam reflection pattern can be also calculated by using element phases obtained from the actual DR diameters of the 6-element reflectarray. In the computation, an incident Gaussian beam with a diameter of 40 μm is deflected and projected on a screen with a distance of 60 mm from the reflectarray. The calculated beam pattern shows a deflected beam at about 17.5°, as clearly visible in Fig 8.19 (a). The spatial harmonic, resulting from the tolerances in the DR diameters, is clearly identified from the analytical estimation.

For comparison, the corresponding measured beam pattern recorded by using the linear camera is shown in Fig. 8.19(b). By integrating the power only around the main

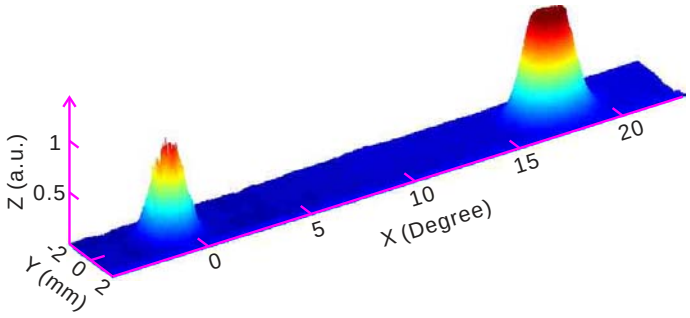

Figure 8.17. 3D representation of the beam shapes for the 6-element reflectarray measured by the Thorlabs LC100 CCD linear camera. Angle of 0° denotes the direction of the specular reflection.

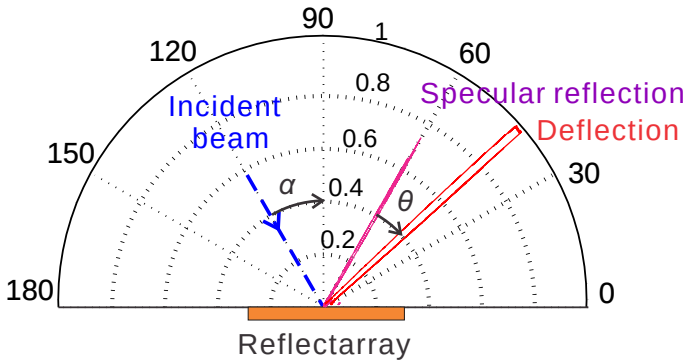

Figure 8.18. Normalized radiation pattern of 6 element reflectarray.

beams, and thus eliminating the scattered field energy, the ratio of the deflected to reflected beam power is estimated to be 3.43, compared with 3.57 from the array theory calculation. The good agreement among the numerical simulation, the array theory analysis and the measurement unambiguously demonstrates the resonance of the DRs and the capability of beam deflection of the proposed optical DRA reflectarray.

8.5 Silver properties measurement

The silver permittivity is highly dependent on the manufacturing process, which can result in different silver densities, grain sizes, surface roughness. The silver permittivity used in designing the first prototype is adopted from [136]. In the case that the permittivity does not match the actual value, the targeted progressive phase shift is not attainable in the experiment, and thus the power of the undesired specular reflection is increased. To characterize the optical properties of silver, a 200 nm thick silver layer is deposited on a silicon wafer by using the same procedure as for the first sample. Characterization of the deposited silver is carried out through ellipsometry.

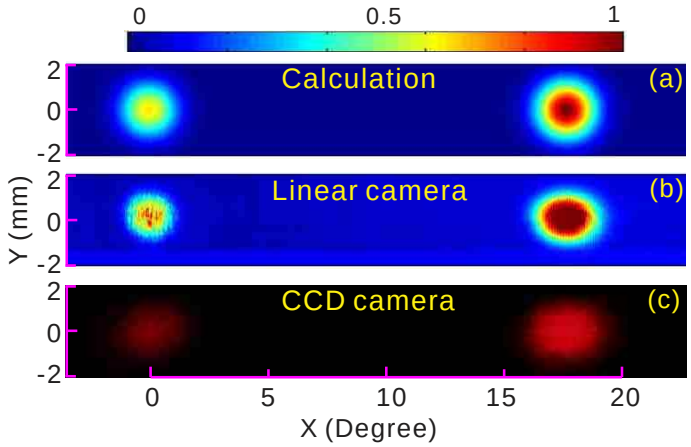

Figure 8.19. Normalized beam reflection pattern of 6 element reflectarray. Angle of 0° denotes the direction of the specular reflection.

The measured n and κ of thin silver layer at a wavelength of 633 nm are 0.12312 and 4.00819, respectively. This corresponds to the silver permittivity of $-16.05 + j0.99$. The real part of the measured silver permittivity compares favorably with the real part of $-17.47 + j0.57$ used in the first design. The variation of the real part can be attributed to a difference in the density of the silver film obtained from different fabrication procedures. A comparison of the simulated phase and magnitude responses of the resonators using different values of the silver permittivity is shown in Fig. 8.20. These graphs indicate that varying the real part of silver permittivity will shift the resonance frequency of the DRs and change the magnitude of the reflected beam. On the other hand, a large difference in the imaginary part of the permittivity used in the first design (0.57) and the measured silver permittivity (0.99) results from the scattering from the rough surface of the deposited silver, which is manifested as a power reduction in the specular reflection in the measurement. The imaginary part has a little effect on the phase responses but changes markedly the magnitude responses (i.e. the reflection coefficient), indicating a variation in the amount of loss in the silver.

8.6 Improved design of optical DRA reflectarray

On that basis, in a second design evolved from the first prototypes, the real part of the silver permittivity is taken from the measured value of -16.05. The imaginary part of the silver permittivity kept unchanged (0.57) to avoid using the exaggerated silver loss and also because it does not affect the resonance frequency.

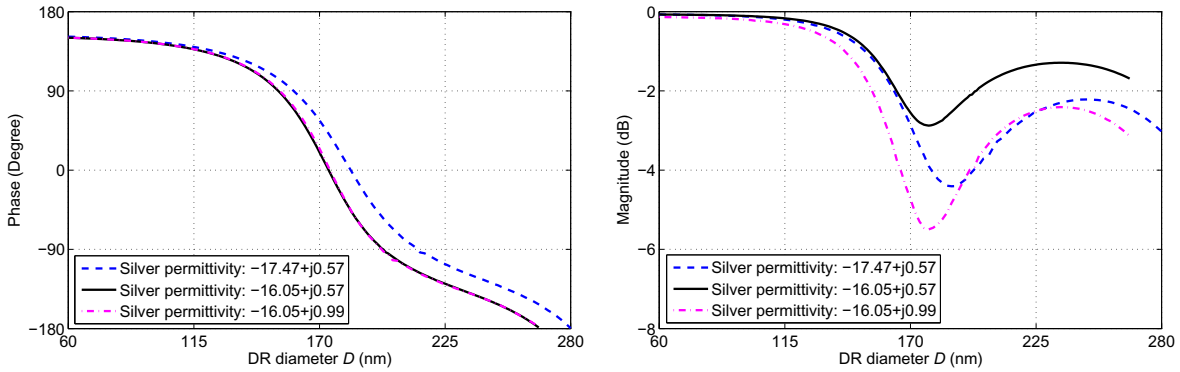

(a) Phase responses

(b) Magnitude responses

Figure 8.20. Numerically resolved phase and magnitude response of DRs by using different silver permittivity at 474 THz.

Only 6 and 9-element reflectarrays are fabricated in the second set of samples since they have demonstrated better performance than the 4-element reflectarray in the first set of samples. As discussed in the Section 8.2.2, a small unit cell size will result in an increased robustness of the design, but, will raise the chance of merging adjacent DRs during fabrication. Considering both robustness design and fabrication capability, the distance between DR centre of 6 and 9-element reflectarrays are chosen as 310 and 320 nm, respectively.

The second set of samples was fabricated by using the same materials and following the same procedure as the first set of samples. Figure 8.21 shows the DR diameters and the distance between DR centre of the 6 and 9-element reflectarrays, measured by scanning electron microscope. The inaccuracies in the fabricated arrays introduce scattering noise and increase the amount of power in the specular reflection. The comparison of the designed and actual DR diameters and phase of the 6 and 9-element reflectarrays is shown in Fig 8.22. Compared with the results achieved in manufacture of the first sample, the realized DR diameters for the second set of samples are closer to the desired values. Particularly, the accuracy of the DRs close to the resonance is improved. Hence, the reflectarray performance is expected to be improved.

8.7 Second prototypes measurement and discussion

The second sets of reflectarrays is measured by using the same setup as described in Section 8.4. Figure 8.23 demonstrates the beam deflection off the main specular angle

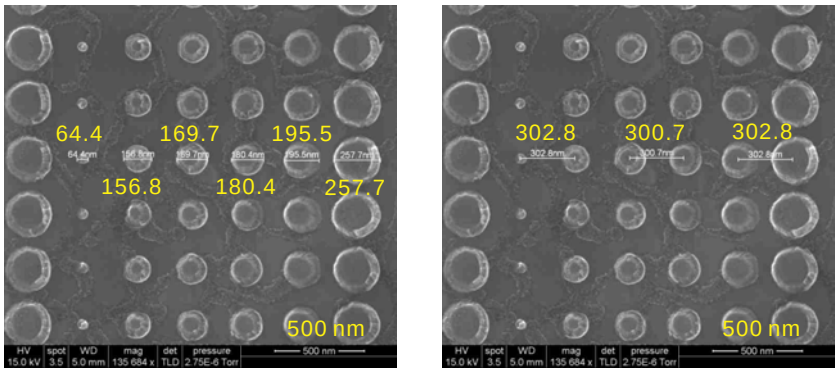

(a) 6 element reflectarray

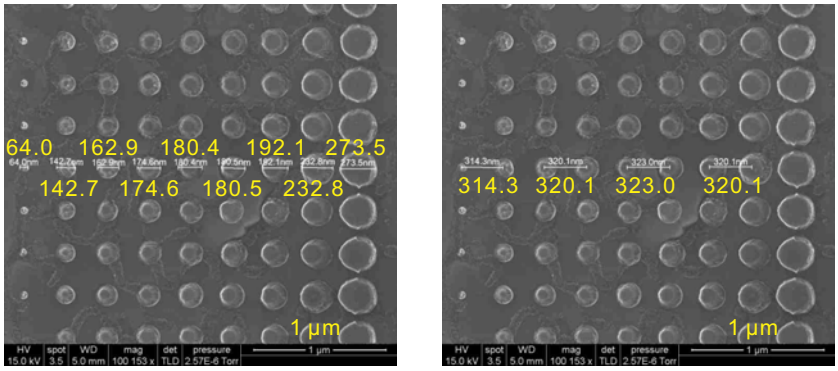

(b) 9 element reflectarray

Figure 8.21. Scanning electron micrograph revealing an area on the fabricated 6 and 9 element reflectarrays.

by the expected 19.9° for the the 6-element and by 12.7° for the 9-element DRA reflectarrays, when illuminated by a TE polarized incident wave. The ratios of power in the deflected to reflected beam measured with the power meter amounts to 3.74 for the 6-element reflectarray and to 3.32 for the 9-element reflectarray. Figure 8.24 compares the beam reflection patterns obtained from the array theory based on realized DR diameters, the linear camera and the CCD camera. The performance improvement in the second sets of arrays can be clearly observed by comparing these results to those in Fig. 8.19. Based on the linear camera measurement, the ratio of deflected to reflected beam power of the 6-element reflectarray is improved from 3.57 to 4.42. The expected deflected beam angle of 19.9° is clearly illustrated in the radiation pattern measurement, as shown in Fig. 8.25.

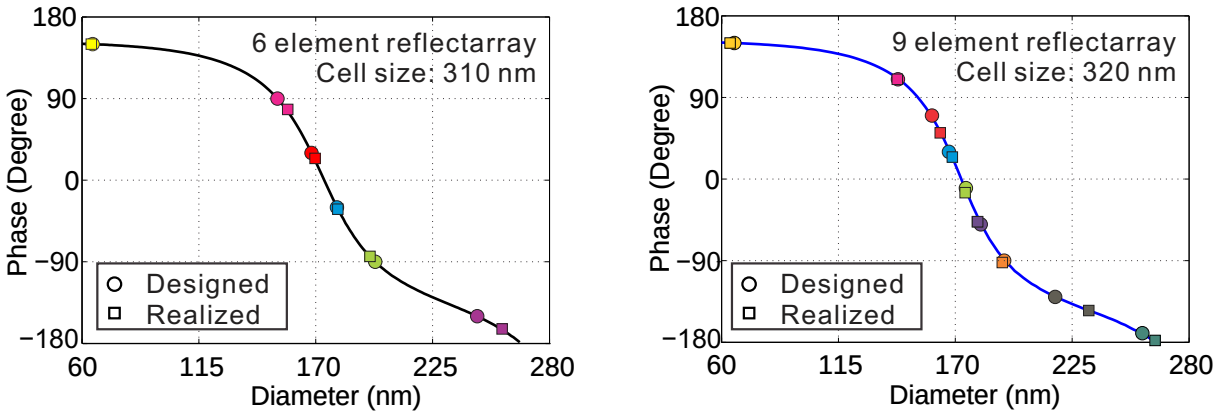

Figure 8.22. Designed and realized DR diameters of 6 and 9 element reflectarray.

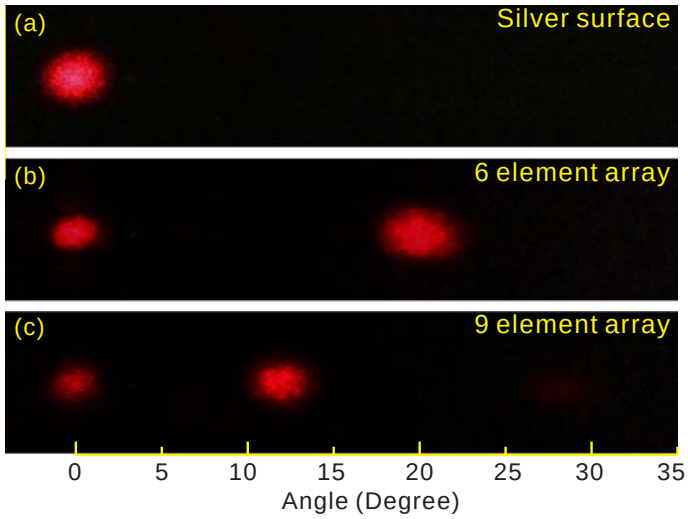

Figure 8.23. CCD imaging of beam reflection patterns excited by TE polarized incident wave.

8.8 Dissipation loss in optical DRs

The proposed array structure eliminates the loss from feeding components, such as sources and guiding channels and thus minimizes the complexity. This makes the approach suitable for studying the dissipation loss in DRs. A uniform DRA reflectarray is designed and fabricated as a platform to investigate the dissipation loss of DRs at optical frequencies. A uniform array with DR centre distance of 350 nm and DR diameter of 180 nm is chosen to study the efficiency of DRs through simulation and measurement.

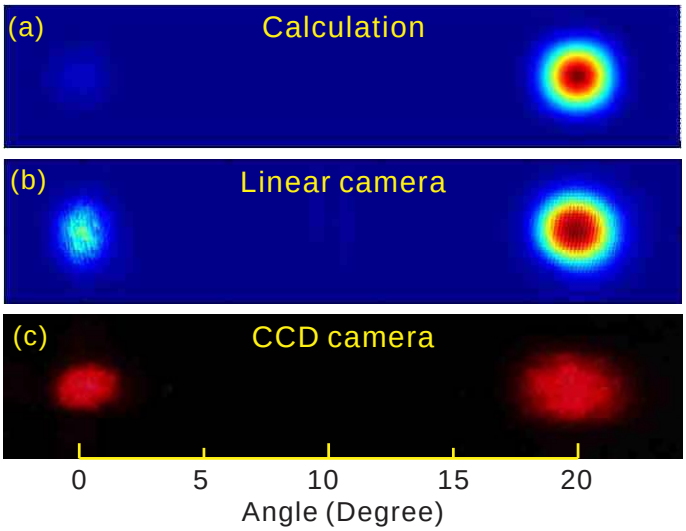

Figure 8.24. The beam reflection patterns obtained from array theory calculation (a), the linear camera (b) and CCD camera (c).

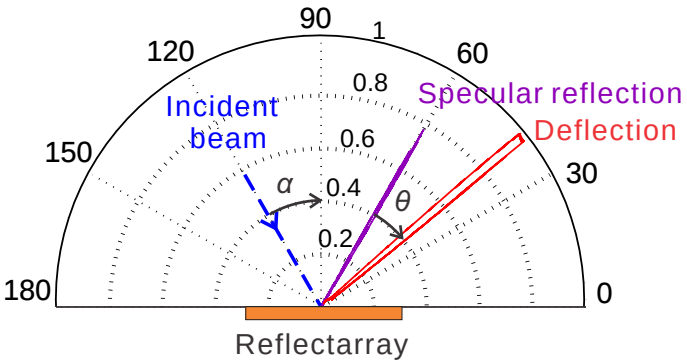

Figure 8.25. Measured radiation pattern of 6 element reflectarray in the second sample.

8.8.1 Simulation

Figure 8.26 shows the phase and magnitude responses of the uniform reflectarray obtained from simulation for different values of the dielectric loss tangent of TiO_2. The phase and magnitude responses from the bare silver surface is also simulated and presented in the same figure as a reference. The phase of the reflected beam from the silver surface is 180° at low frequencies when the dissipation loss in the silver is negligible. Figure 8.26(a) indicates that the phase of the reflected beam becomes 152° at 474 THz due to the surface plasmonic effect. The phase of the resonant DR is also shifted from 0° to -36°, where the strongest absorption occurs, as shown in Fig 8.26(b). Figure 8.26 also clearly reveals that the dielectric loss tangent does not affect the resonance frequency and only changes the magnitude of the reflection.

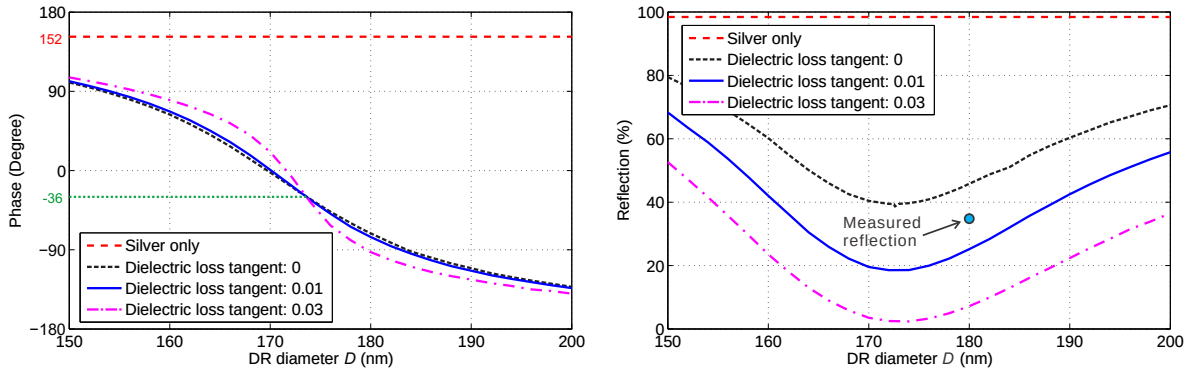

(a) Phase responses

(b) Magnitude responses

Figure 8.26. Numerically resolved phase and magnitude response of of silver and uniform DRA array with different dielectric loss tangent at 474 THz.

The simulated reflection of silver in Fig. 8.26(b) shows that 98.5% power is reflected and the small loss results from the dissipation in the silver. The 45.8% reflection from the uniform array with a hypothetical lossless TiO_2 indicates that the remaining 52.7% has to be coupled to surface plasmon polaritons (SPPs), and then dissipated along the silver surface. The reflection from the uniform array decreases to 25.2% and 7.2% with the dielectric loss tangent increasing to 0.01 and 0.03 respectively. From those number, it is estimated that 20.6% of the incident power can be attributed to dissipation in the DRs with the dielectric loss tangent of 0.01.

8.8.2 Measurement

The efficiency of the uniform DRA array is experimentally observed from a fabricated sample using the same materials and fabrication procedure as described in Section 8.3. In Fig. 8.27, the scanning electron micrograph shows the cylindrical resonators with diameters of around 180 nm and a periodicity of 350 nm. Figure 8.28 depicts the method for measuring the reflected power from the silver surface and the uniform array. The power in the red rectangle is obtained by summing the power in an array of 4×5 squares (shown in blue), each with size of 8×8 mm^2. The power in the red and yellow rectangle area is assumed to be equal because of the random distribution of the diffraction from the imperfect silver surface and the phase noise, resulting from the DR fabrication imperfection. Since a part of the reflected power is blocked by the lens in

the yellow rectangle, the total reflected power is calculated by doubling the power in the red rectangle.

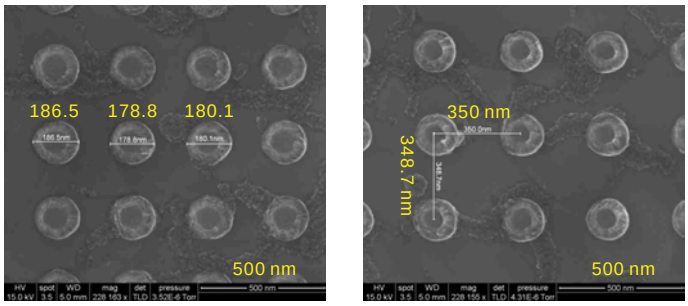

Figure 8.27. Scanning electron micrograph revealing an area on the fabricated uniform DRA array.

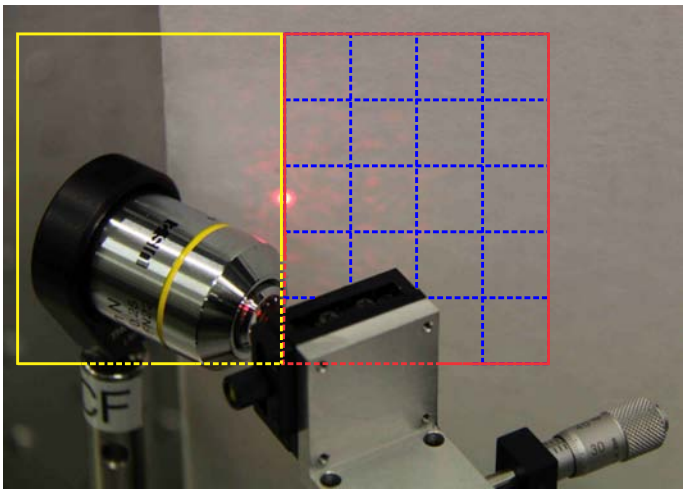

Figure 8.28. Reflection power from uniform array measurement.

With an incident beam power of 1130 μW, the reflected power from the bare silver surface and uniform array are 884.89 μW and 306.97 μW, respectively. In other words, 78.3% of the power is reflected from the silver surface and 34.7% of the power from the uniform array. The difference between the simulated and measured reflection power from the silver surface is attributed to the surface roughness. This measured reflection from the uniform array 34.7% is close the simulated result obtained with assumption of a dielectric loss tangent equal to around 0.01. This agreement between the simulation and measurement confirms the validity of the chosen value of 0.01 for the dielectric loss tangent of TiO_2. The loss of the uniform array mostly results from coupling to SPPs (47.6%) and phase noise (21.7%). Those results reveal that at most 20% of the lost power can be attributed to dissipation in the DRs. Therefore, the DR intrinsic efficiency is around 80% at optical frequencies. Based on this estimation, it is concluded that

the optical DRA has higher efficiency than the plasmonic antennas, such as estimated in [159]. To the best of our knowledge, the experimental data on efficiency of plasmonic antennas are not found in the literature.

8.9 Comparison with grating reflector

A dielectric grating reflector is simulated in this section to verify that the measured beam shaping cannot be achieved without the resonance mechanism on a relatively flat structure. A reflector with equivalent effective refractive index as TiO_2, as shown in Fig. 8.29, is composed of six elongated strips in one subarray. Each strip is made of the same volume of TiO_2 as the proposed 6-element DRA reflectarray in each cell, i.e. the height of a strip is given as

$$h_i = 50\pi \times (D_i/2)^2/310^2, \tag{8.2}$$

where D_i denotes the DR diameter and i=1, 2, ..., 6 indicates the element number. The resulting height of the strips varies from 1.78, 9.69, 11.81, 13.24, 15.22 to 23.93 nm in one subarray. The simulated scattered field from the grating reflector is shown in Fig. 8.30 for the normally incident TE and TM polarized waves. Without the resonance mechanism, the grating structure does not exhibit any noticeable deflection to a specific angle. This clearly proves that the experimentally demonstrated deflection arises from resonant behaviour of the TiO_2 cylindrical resonators.

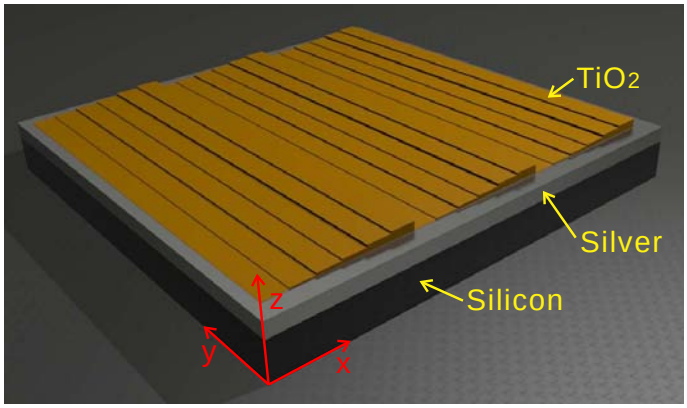

Figure 8.29. Grating reflector with the same TiO_2 volume as DRA reflectarray.

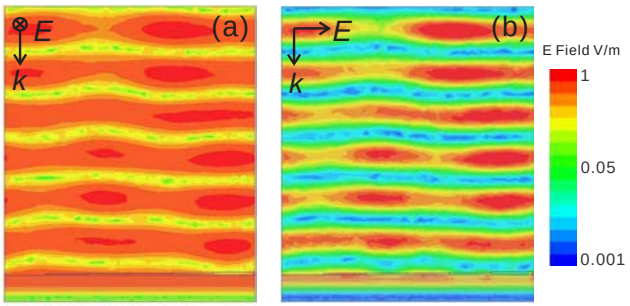

Figure 8.30. Scattered electric fields of grating reflector for the TE (a) and TM (b) normally polarized incident waves.

8.10 Conclusion

In this chapter, DRA reflectarrays have been introduced both through simulation and experiments to demonstrate the concept of optical DRAs. The proposed reflectarray is a periodic structure with capacity of manipulating an optical beam, e.g. by introducing deflection to a predefined angle. Although the zeroth-order spatial harmonic specular reflection is observed in the measurement due to the fabrication imperfection, the power ratio of the deflected beam to the spatial reflection amounts to 4.42, demonstrating the expected operation of the reflectarray. The measured deflected beam angle is in nearly perfect agreement with the prediction from simulation and array theory calculation. A uniform DRA array has been fabricated as a platform to study the efficiency of DRAs at optical frequencies. Both the simulation and measurement results indicate that less than 20% of the power loss can be attributed to the dissipation in the DRs. These results strongly support the concept of optical DRA, as emerging opportunity for realising nanophotonic applications.

Chapter 9

Conclusion and future work

THIS chapter concludes the thesis by first reviewing and summarizing the most important results and findings of each chapter. Four high performance microwave dielectric resonator antennas (DRAs) are proposed, designed and experimentally validated in this PhD research. As another aspect of the research, the DRA concept is extended from microwave to the the visible spectrum. The fundamentals for designing optical DRAs are investigated and then validated by optical nano-DRAs reflectarrays. The chapter then considers possible future research on DRAs, both as microwave and optical antenna with attractive characteristics. The proposed optical DRA concept opens a number of research directions along the path to optical DRAs and optical DR waveguide.

9.1 Conclusion

The research work in this thesis includes two major aspects related to the dielectric resonator antennas (DRAs): The first part of the thesis describes multifunction and diversity DRA implemented using a single dielectric resonator (DR), while the second part of the thesis extends DRA research from microwave to the visible spectrum. These two aspects are respectively based on two attractive features of DRAs,

- Various resonant modes can exist in a DR volume and each mode is related to different radiation characteristics. The orthogonality of field distribution for the fundamental modes builds the basis for realization of low coupling multi-mode design. The resonance frequency and bandwidth of selected orthogonal modes can be designed to satisfy the desired requirements by optimizing the DR geometry and the configuration of the feeding network.
- The high radiation efficiency of DRA has been experimentally proved in the millimeter wave (MMW) frequency region due to the absence of the inherent conductor losses in DR. This motivates further scaling towards optical frequencies, and suggests favorable performance when compared to metallic optical antennas.

Apart from these two features, other advantages of DRAs, including small size, light weight, low cost, coupling to most transmission lines and design flexibility, allow for a wide range of designs to satisfy specified requirements.

In light of these features, various DRAs have been proposed in the literature with enhanced performance in terms of bandwidth, gain, radiation efficiency and functionality. It is noted that a deep and thoughtful understanding of resonance frequency, excited modes, impedance bandwidth and radiation characteristics is generally required to create novel advanced designs. As basis for this understanding, the canonical DRA geometries, including hemisphere, rectangle and cylinder, are the fundamental building blocks for all other advanced DRA geometries. Thus, the near fields and the radiation characteristics of fundamental modes, their corresponding resonance frequencies and Q-factors as well as the feeding methods of canonical DRA geometries are firstly examined in Chapter 2.

Based on the study in Chapter 2, four microwave DRAs are proposed, designed and experimentally validated in the first part of the thesis, including Chapter 3, 4, 5 and 6.

1. Chapter 3 proposes a high-permittivity cross-shaped DRA for circularly polarized applications. The cross-shaped DR is composed of two same-size notched rectangular thin slices of dielectric ceramic with 1 mm thickness and high relative permittivity of $\varepsilon_r = 50$. Numerical simulations show that the effective relative permittivity of this thin high-permittivity cross is equal to 42.6 due to the fact that field is extending into the air outside of the DR.

   In the two crossed equal-length arms of the DR, the TE_{111} modes are excited by two orthogonal microstrip lines with 90° phase difference to generate circular polarization. The combination of high-permittivity material for the DRA and of a quadrature feed results in a compact design with an impedance bandwidth of 21% and a broadside circularly polarized bandwidth of 13.2%.

   The simple antenna configuration and feeding mechanism make this design easily scalable to other frequency bands or extendable towards multifunction designs. In an evolution of the design, a ground plane is placed between the DR and the feeding network to reduce the impact from the feeding network on the radiation pattern.

2. Chapter 4 extends the circularly polarized DRA, proposed in Chapter 3, to a multifunction and diversity DRA with separately fed broadside circularly polarized radiation pattern (Port 1) and omnidirectional linearly polarized radiation pattern (Port 2). The circularly polarized and linearly polarized radiation patterns are achieved in an overlapping frequency band by exciting the TE_{111} and Quasi-TM_{111} modes, respectively.

   The coupling between these two modes is theoretically zero due to their orthogonal field distribution. However, an asymmetric feeding method can disturb the field distribution in the DR and thus increase the mutual coupling between these two modes. The asymmetric field distribution can be corrected by using either an asymmetric DR structure or a symmetrized feeding method. Using either of these two methods, the simulated coupling coefficient can be reduced to less than -15 dB. The symmetrized feeding method proved superior, and a prototype is fabricated by using a sequential rotation technique. The measured mutual coupling is below -30 dB throughout the circularly polarized band.

   The measured impedance bandwidth of the circularly polarized port is 13.5% and its measured 3 dB axial ratio (AR) bandwidth extends from 4.52 to 4.84 GHz. This yields an overlap of the AR and impedance bandwidth of 6.8%. Through the

optimization of the feeding probe of the linearly polarized port, its impedance bandwidth is increased to 38.5% while overlapping with the impedance bandwidth of the circularly polarized port. The simulated and measured radiation patterns of Port 1 show broadside left-hand circularly polarized radiation patterns with more than 60° usable circularly polarized angle. Vertically polarized monopole-type radiation patterns with low cross-polarization are obtained in Port 2. The mean effective gain and envelope correlation coefficient are calculated from S-Parameters to evaluate the diversity performance of the proposed antenna. Both simulated and measured results demonstrate good diversity antenna performance with low inter-port mutual coupling, high port mean effective gain and low envelope correlation coefficient.

3. In Chapter 5, a horizontally polarized cylindrical DRA is designed by exciting the $TE_{01\delta}$ mode. Due to the inherent high Q-factor of this mode, it has been only used in filter applications before. The issue of narrow bandwidth is solved by adding an air gap to the geometry and optimizing the feeding scheme. The air gap is introduced between the cylindrical DR and the ground plane to lower the effective permittivity of the DR and increase its distance from the ground plane, which otherwise would inhibit the mode. A balanced coupling method consisting of two arc-shaped microstrip lines on each side of the DR is utilized to provide effective excitation of the $TE_{01\delta}$ mode. The feeding lines are optimized to enhance the bandwidth and the resulting best design has been validated through measurements. A 5.6% bandwidth with omnidirectional horizontally polarized radiation has been demonstrated experimentally.

4. Chapter 6 presents a multifunction and diversity annular cylindrical DRA realizing simultaneously omnidirectional horizontally and vertically polarized radiation patterns. The horizontally polarized (Port 1) and vertically polarized (Port 2) radiation patterns are achieved by exciting the $TE_{01\delta}$ and $TM_{01\delta}$ modes, respectively. Compared to the design in Chapter 5, the impedance bandwidth of Port 1 is further increased from 5.6% to 7.4% by employing two forked groups of four radially arranged microstrip feeding lines with two different lengths. To realize multifunction and diversity operation, the impedance bandwidth of the $TM_{01\delta}$ mode is increased to overlap with the operating band of the $TE_{01\delta}$ mode, with minimal coupling between the two orthogonal modes. Both simulated and measured results demonstrate good diversity antenna performance.

Another goal of the thesis is extending DRA research from microwave to the visible spectrum. After the investigation of fundamentals for designing optical DRAs in Chapter 7, optical DRA reflectarrays are designed and measured in Chapter 8.

1. In Chapter 7, the research on DRAs is extended from microwave to the visible spectrum, towards the realization of optical dielectric resonator nano-antennas. The efficiency of conventional resonant metallic antennas decreases significantly with increasing frequency due to the dissipation loss in metal. Considering the absence of inherent conductor losses of DRA and the availability of high permittivity dielectric materials at optical frequencies, we propose the concept of optical DRA with enhanced efficiency.

   Since most of DRAs are composed of a DR mounted on a metal surface, the research starts with a scalable DRA model employing appropriate metal models to describe the silver complex permittivity in different spectral regions, including the modified relaxation-effect model and the Drude model. The scalable DRA model is built and simulated in the commercial EM simulation software HFSS with rising frequencies from microwave to visible spectrum. Through the DRA scaling behaviour study, it is shown that the surface impedance model has acceptable accuracy with low computational costs below the near-infrared spectrum. In contrast, the Drude model provides a more accurate description of the field penetration and dispersive properties of metal at optical frequencies. However, the large negative permittivity of silver described by the Drude model leads to a fine mesh requirement and hence increases the computational cost in mesh-based EM simulations. This limits the Drude model application to near-infrared and visible frequencies.

   Based on this scaling study, the field distributions confirm the possible excitation of the fundamental $HEM_{11\delta}$ mode in the cylindrical DR at 500 THz. However, although the excited $HEM_{11\delta}$ mode for the DR in the optical frequency range has a similar field distribution as its counterpart in the microwave frequency range, the electric field extends markedly into the silver ground plane due to the plasmonic effect, which thus significantly reduces the DR size.

2. In Chapter 8, the optical DRA concept has been indirectly evaluated through simulation and experiments of various implementations of DRA reflectarrays. The reflectarray configuration eliminates the need for integrated feeding components

and thus is suitable for the studying of fundamental optical DRA property. The proposed reflectarray is a periodic structure with the capacity of manipulating the reflected beam to a predefined deflection angle. The angle deflection for the reflected beam is manipulated by using a periodic arrangement of cylindrical DRs sub-arrays, with varying diameters appropriately selected around the dimension of the resonant fundamental $HEM_{11\delta}$ mode. Although the zeroth-order spatial harmonic specular reflection is observed in the measurement due to the fabrication imperfection, the power ratio of the deflected beam to the spatial reflection amounts to 4.42, demonstrating the expected operation of the reflectarray.

The resonance mechanism of the reflectarray is confirmed through a comparison with a dielectric grating structure using the same volume amount of dielectric material as the DRA reflectarray. The simulated reflected E field from this dielectric grating reflector verifies that the measured beam shaping cannot be achieved without the resonance mechanism on a relatively flat structure. Furthermore, the simulation and measurement results of a uniform array reveal that only 20% of the lost power can be attributed to dissipation in the DRs.

9.2 Future work

Today's highly integrated electronic wireless communication devices not only leaves limit space for antenna but also demands more functionality from antenna. It is essential to realize multifunction and diversity scheme in a single antenna. The thesis has only focused on using the fundamental modes to realize multifunction and diversity DRA in a single DR. Higher-order modes of DRs have been intensively investigated by other groups, e.g. Prof. Leung's group from the City University of Hong Kong. Wideband DRAs, dual-band DRAs, MMW DRAs, and high-gain DRAs have been realized by using higher order modes or the combination of higher order modes and fundamental modes. It would be interesting to realize multifunction and diversity DRA with the combination of higher order and fundamental modes to achieve wider bandwidth, dual-band or higher gains.

The demand for high speed wireless communications, together with unlicensed spectrum around at MMW frequencies, has led to increasing research and application in the sub-millimeter and millimeter wave ranges. However, the efficiency of the conventional metallic antenna deteriorates at higher frequencies. Considering the absence

of inherent conductor losses, DRAs are the best choices among the current existing antennas for applications requiring a high radiation efficiency. Therefore, another direction would be to explore DRAs on the spectrum higher than GHz.

Terahertz and infrared spectrum have attracted enormous attention in recent years. Various applications with a potentially large impact have been identified, particularly in the area of imaging, sensing and biomedicine. Due to the absence of inherent conductor losses, DRAs are suitable for applications with high efficiency requirement at these frequencies. The proposed scaling DRA model, together with the practical method of characterizing metal properties, can easily be adapted and implemented to THz and infrared DRA design. Stimulated by advanced fabrication techniques, it can be expected that an increasing number of THz and infrared DRAs with high efficiency will be emerging in the near future.

The work in this thesis has demonstrated a first (to the best of our knowledge) experimental realization of optical dielectric resonator nano-antennas. This represents a first step towards optical DRAs with enhanced efficiencies and functionalities. The research opens a number of directions that could provide the next steps along the path to optical DRAs and optical DR waveguide, further enabled by the progress of nanofabrication techniques. Some of the possible research directions are the following.

- This thesis has only discussed cylindrical DRs made of TiO_2. However, a wide range of dielectric material, geometries and corresponding modes exist and need to be explored, in terms of suitabilities of material properties, manufacturability and stability.

- The dimension of optical antenna is the order of nanometer and this requires fabrication accuracies down to a few nanometers. This remains quite challenge for the current nanofabrication techniques. A millimeter wave rectangular DRA proposed by Leung's group shows that using a higher order mode can significantly increase DR size, which makes the design more tolerant of fabrication [130]. Thus, it is worth to investigate optical nano-scale DRAs using higher-order modes in order to have more robust design.

- The fabricated optical reflectarray has the capacity of deflecting beam to a predefined deflection angle. Further investigation needs to be carried out to obtain more functions including, focusing, diverging and diffracting.

- The measured reflection from the fabricated uniform array shows nearly half power is coupled to surface plasmon polaritons (SPPs) and less than 20% of the power loss can be attributed to the dissipation in the DRs. Thus, it is feasible to realize a all dielectric optical antenna with high efficiency by replacing the metal substrate with low permittivity dielectric material, or a dielectric mirror.

- The proposed optical reflectarray structure can be exploited to control coupling between DR and metal, with excitation of surface plasmons. With the low coupling between DR and metal, high quality reflector can be designed. On the other hand, high coupling between the DRs and the metal makes it feasible to produce DR waveguides or optical absorbers. One important implication could be in solar panels. However, this path will require further research and fundamental breakthroughs including better understanding of metal behaviour and coupling between DRs.

- Due to the lack of true nanoscale light sources and efficient transmission line (waveguide), the reflectarray is excited by a laser in this thesis. The future optical DRA will not only consider the radiating part but also the source and feeding schemes.

The results in this thesis emphasize the attractive features of DRAs in the applications requiring wider bandwidth and/or higher radiation efficiency in the frequencies above GHz.

Bibliography

[1] R. D. Richtmyer, "Dielectric resonators," *J. Appl. Phys.*, vol. 10, pp. 391–398, 1939.

[2] A. Okaya and L. Barash, "The dielectric microwave resonator," *Proceedings of the IRE*, vol. 50, no. 10, pp. 2081–2092, Oct. 1962.

[3] J. Van Bladel, "On the resonances of a dielectric resonator of very high permittivity," *IEEE Trans. Microw. Theory Tech.*, vol. 23, no. 2, pp. 199–208, Feb. 1975.

[4] ——, "The excitation of dielectric resonators of very high permittivity," *IEEE Trans. Microw. Theory Tech.*, vol. 23, no. 2, pp. 208–217, Feb. 1975.

[5] S. Long, M. McAllister, and L. Shen, "The resonant cylindrical dielectric cavity antenna," *IEEE Trans. Antennas Propag.*, vol. 31, no. 3, pp. 406–412, May 1983.

[6] A. Petosa, A. Ittipiboon, Y. Antar, D. Roscoe, and M. Cuhaci, "Recent advances in dielectric-resonator antenna technology," *IEEE Antennas Propag. Mag.*, vol. 40, no. 3, pp. 35–48, 1998.

[7] K. M. Luk and K. W. Leung, *Dielectric Resonator Antennas*. Research Studies Press LTD. England, 2003.

[8] G. Almpanis, C. Fumeaux, and R. Vahldieck, "The trapezoidal dielectric resonator antenna," *IEEE Trans. Antennas Propag.*, vol. 56, no. 9, pp. 2810–2816, Sep. 2008.

[9] E. H. Lim and K. W. Leung, "Novel application of the hollow dielectric resonator antenna as a packaging cover," *IEEE Trans. Antennas Propag.*, vol. 54, no. 2, pp. 484–487, Feb. 2006.

[10] K. W. Leung, E. H. Lim, and X. S. Fang, "Dielectric resonator antennas: From the basic to the aesthetic," *Proceedings of the IEEE*, vol. 100, no. 7, pp. 2181–2193, Jul. 2012.

[11] Q. Lai, G. Almpanis, C. Fumeaux, H. Benedickter, and R. Vahldieck, "Comparison of the radiation efficiency for the dielectric resonator antenna and the microstrip antenna at Ka band," *IEEE Trans. Antennas Propag.*, vol. 56, no. 11, pp. 3589–3592, 2008.

[12] S.-L. Yang, K. M. Luk, H.-W. Lai, A. A. Kishk, and K.-F. Lee, "A dual-polarized antenna with pattern diversity," *IEEE Antennas Propag. Mag.*, vol. 50, no. 6, pp. 71–79, Dec. 2008.

[13] V. Plicanic, B. K. Lau, A. Derneryd, and Z. Ying, "Actual diversity performance of a multiband diversity antenna with hand and head effects," *IEEE Trans. Antennas Propag.*, vol. 57, no. 5, pp. 1547–1556, May 2009.

[14] A. Chebihi, C. Luxey, A. Diallo, P. Le Thuc, and R. Staraj, "A novel isolation technique for closely spaced PIFAs for UMTS mobile phones," *IEEE Antennas Wireless Propag. Lett.*, vol. 7, pp. 665–668, 2008.

[15] A. Diallo, C. Luxey, P. Le Thuc, R. Staraj, and G. Kossiavas, "Study and reduction of the mutual coupling between two mobile phone PIFAs operating in the DCS1800 and UMTS bands," *IEEE Trans. Antennas Propag.*, vol. 54, no. 11, pp. 3063–3074, Nov. 2006.

[16] E. H. Lim and K. W. Leung, "Use of the dielectric resonator antenna as a filter element," *IEEE Trans. Antennas Propag.*, vol. 56, no. 1, pp. 5–10, Jan. 2008.

[17] M. N. Jazi and T. A. Denidni, "Design and implementation of an ultrawideband hybrid skirt monopole dielectric resonator antenna," *Antennas Wireless Propag. Lett.*, vol. 7, pp. 493–496, 2008.

[18] L. K. Hady, A. A. Kishk, and D. Kajfez, "Dielectric resonator antenna utilization as a direction finder," in *Antennas and Propagation Society International Symposium, 2009. APSURSI '09. IEEE*, Jun. 2009, pp. 1–4.

[19] ——, "Dual-band compact DRA with circular and monopole-like linear polarizations as a concept for GPS and WLAN applications," *IEEE Trans. Antennas Propag.*, vol. 57, no. 9, pp. 2591–2598, 2009.

[20] L. Zou and C. Fumeaux, "High-permittivity cross-shaped dielectric resonator antenna for circular polarization," in *Int. Conf. Electromagn. Adv. App.*, Sep. 2010, pp. 1–4.

[21] ——, "Cross-shaped dielectric resonator antenna for circular polarization with symmetric radiation patterns," in *Twelfth Australian Symposium on Antennas*, Feb. 2011.

[22] ——, "A cross-shaped dielectric resonator antenna for multifunction and polarization diversity applications," *IEEE Antennas Wireless Propag. Lett.*, vol. 10, pp. 742–745, Jul. 2011.

[23] ——, "Mutual coupling reduction in a multi-mode multi-function dielectric resonator antenna," in *International Symposium on Antennas and Propagation (APS)*, Jul. 2012.

[24] ——, "Horizontally polarized omnidirectional dielectric resonator antenna," in *Asia-Pacific Microwave Conference (APMC), 2011*, Dec. 2011, pp. 849–852.

[25] L. Zou, D. Abbott, and C. Fumeaux, "Omnidirectional cylindrical dielectric resonator antenna with dual polarization," *IEEE Antennas Wireless Propag. Lett.*, vol. 11, pp. 515–518, 2012.

[26] L. Zou, W. Withayachumnankul, C. Shah, A. Mitchell, M. Bhaskaran, S. Sriram, and C. Fumeaux, "Dielectric resonator nanoantennas at visible frequencies," *Opt. Express*, vol. 21, no. 1, pp. 1344–1352, Jan. 2013.

[27] ——, "Optical reflectarray based on dielectric resonator antennas," in *Australian Nanotechnology Network (ANN) 2012 Early Career Symposium*, Dec. 2012.

[28] ——, "Optical dielectric resonator antennna reflectrray," in *Thirteeth Australian Symposium on Antennas*, Feb. 2013.

[29] D. Guha and Y. Antar, "New half-hemispherical dielectric resonator antenna for broadband monopole-type radiation," *IEEE Trans. Antennas Propag.*, vol. 54, no. 12, pp. 3621–3628, Dec. 2006.

[30] A. Ittipiboon, D. Roscoe, R. K. Mongia, and M. Cuhaci, "A circularly polarized dielectric guide antenna with a single slot feed," in *Proceedings of the Symposium on Antenna Technology and Applied Electromagnetics ANTEM-94*, Ottawa, Canada, 1994, pp. 427–430.

[31] M. Lapierre, Y. Antar, A. Ittipiboon, and A. Petosa, "Ultra wideband monopole/dielectric resonator antenna," *IEEE Microw. Wireless Compon. Lett.*, vol. 15, no. 1, pp. 7–9, Jan. 2005.

[32] G. Almpanis, C. Fumeaux, J. Fröhlich, and R. Vahldieck, "A truncated conical dielectric resonator antenna for body-area network applications," *IEEE Antennas Wireless Propag. Lett.*, vol. 8, pp. 279–282, Sep. 2009.

[33] K. W. Leung and K. K. So, "Theory and experiment of the wideband two-layer hemispherical dielectric resonator antenna," *IEEE Trans. Antennas Propag.*, vol. 57, no. 4, pp. 1280–1284, Apr. 2009.

[34] K.-L. Wong, N.-C. Chen, and H.-T. Chen, "Analysis of a hemispherical dielectric resonator antenna with an airgap," *IEEE Microw. and Guided Wave Lett.*, vol. 3, no. 10, pp. 355–357, Oct. 1993.

[35] K. W. Leung, X. Fang, Y. Pan, E. Lim, K. M. Luk, and H. Chan, "Dualfunction radiating glass for antennas and light covers- part ii: Dualband glass dielectric resonator antennas," *IEEE Trans. Antennas Propag.*, vol. PP, no. 99, p. 1, 2012.

[36] A. Petosa, *Dielectric Resonator Antenna Handbook*. Artech House, 2007.

[37] R. Collin, *Foundation for Microwave Engineering*. McGraw-Hill, 1996.

[38] R. K. Mongia and P. Bhartia, "Dielectric resonator antennas - a review and general design relations for resonant frequency and bandwidth," *International Journal of Microwave and Millimeter-wave Computer-aided Engineering*, vol. 4, no. 3, pp. 230–247, 1994.

[39] D. Pozar, *Microwave Engineering*, 3rd ed. Wiley, 2005.

[40] R. K. Mongia and A. Ittipiboon, "Theoretical and experimental investigations on rectangular dielectric resonator antennas," *IEEE Trans. Antennas Propag.*, vol. 45, no. 9, pp. 1348–1356, 1997.

[41] R. Harrington, *Time Harmonic Electronmagnetic Fields*. York: McGraw-Hill, 1961.

[42] E. Marcatili, "Dielectric rectangular waveguide and directional coupler for integrated optics," *Bell Syst. Tech. J.*, vol. 48, pp. 2071–2102, 1969.

[43] R. Collin and F. Zucker, *Antenna Theory: Part 1,*. McGraw-Hill, 1969.

[44] A. Al-Zoubi and A. Kishk, "Wide band strip-fed rectangular dielectric resonator antenna," in *3rd European Conference on Antennas and Propagation*, Mar. 2009, pp. 2379–2382.

[45] X.-L. Liang and T. Denidni, "H-shaped dielectric resonator antenna for wideband applications," *IEEE Antennas Wireless Propag. Lett.*, vol. 7, pp. 163–166, 2008.

[46] ——, "Cross-T-shaped dielectric resonator antenna for wideband applications," *Electron. Lett.*, vol. 44, no. 20, pp. 1176–1177, Sep. 2008.

[47] L.-N. Zhang, S.-S. Zhong, and S.-Q. Xu, "Broadband U-shaped dielectric resonator antenna with elliptical patch feed," *Electron. Lett.*, vol. 44, no. 16, pp. 947–949, Jul. 2008.

[48] X.-L. Liang, T. Denidni, and L.-N. Zhang, "Wideband L-shaped dielectric resonator antenna with a conformal inverted-trapezoidal patch feed," *IEEE Trans. Antennas Propag.*, vol. 57, no. 1, pp. 271–274, Jan. 2009.

[49] K. W. Leung, K. Y. A. Lai, K. M. Luk, and D. Lin, "Input impedance of aperture coupled hemispherical dielectric resonator antenna," *Electron. Lett.*, vol. 29, no. 13, pp. 1165–1167, Jun. 1993.

[50] K. W. Leung, K. M. Luk, K. Y. A. Lai, and D. Lin, "Theory and experiment of an aperture-coupled hemispherical dielectric resonator antenna," *IEEE Trans. Antennas Propag.*, vol. 43, no. 11, pp. 1192–1198, Nov. 1995.

[51] K. W. Leung and K. So, "Rectangular waveguide excitation of dielectric resonator antenna," *IEEE Trans. Antennas Propag.*, vol. 51, no. 9, pp. 2477–2481, Sep. 2003.

[52] G. Almpanis, C. Fumeaux, and R. Vahldieck, "Double-bowtie-slot-coupled DRA for enhanced bandwidth," in *Proc. 22nd Annual Review of Progress in Applied Computational Electromagnetics, ACES*, Mar. 2006, pp. 812–818.

[53] C.-Y. Huang, J.-Y. Wu, and K.-L. Wong, "Cross-slot-coupled microstrip antenna and dielectric resonator antenna for circular polarization," *IEEE Trans. Antennas Propag.*, vol. 47, no. 4, pp. 605–609, Apr. 1999.

[54] G. Almpanis, C. Fumeaux, and R. Vahldieck, "Offset cross-slot-coupled dielectric resonator antenna for circular polarization," *IEEE Microwave Wireless Compon. Lett.*, vol. 16, no. 8, pp. 461–463, 2006.

[55] K. Gupta, R. Garg, and I. Bahl, *Microstrip Lines and Slotlines*. Artech House, Inc., 1979.

[56] J.-Y. Wu, C.-Y. Huang, and K.-L. Wong, "Low-profile, very-high-permittivity dielectric resonator antenna excited by a coplanar waveguide," *Microw. Opt. Technol. Lett.*, vol. 22, no. 2, pp. 96–97, 1999.

[57] S. Deng, C. Tsai, C. Chiu, and S. Chang, "CPW-fed rectangular ceramic dielectric resonator antennas with high profile," in *IEEE Antennas and Propagation Society International Symposium, 2004.*, vol. 1, Jun. 2004, pp. 1098–1101.

[58] R. Kranenburg, S. Long, and J. Williams, "Coplanar waveguide excitation of dielectric resonator antennas," *IEEE Trans. Antennas Propag.*, vol. 39, no. 1, pp. 119–122, Jan. 1991.

[59] B. Ghosh, Y. Antar, A. Petosa, and A. Ittipiboon, "Feed configurations of CPW fed DRA," in *IEEE Antennas and Propagation Society International Symposium, 2004.*, vol. 2, Jun. 2004, pp. 1347–1350.

[60] B. Ghosh, Y. M. Antar, A. Petosa, and A. Ittipiboon, "CPW feed to rectangular DRA," *Microw. Opt. Technol. Lett.*, vol. 45, no. 3, pp. 210–216, 2005.

[61] M. Al Salameh, Y. Antar, and G. Seguin, "Coplanar-waveguide-fed slot-coupled rectangular dielectric resonator antenna," *IEEE Trans. Antennas Propag.*, vol. 50, no. 10, pp. 1415–1419, Oct. 2002.

[62] Y. Gao, B.-L. Ooi, W.-B. Ewe, and A. Popov, "A compact wideband hybrid dielectric resonator antenna," *IEEE Microw. Wireless Compon. Lett.*, vol. 16, no. 4, pp. 227–229, Apr. 2006.

[63] K. Wu, D. Deslandes, and Y. Cassivi, "The substrate integrated circuits - a new concept for high-frequency electronics and optoelectronics," in *6th Int. Conf. on Telecommunications in Modem Satellite, Cable and Broadcasing Service, TELSIKS 2003*, vol. 1, Oct. 2003.

[64] F. Xu and K. Wu, "Guided-wave and leakage characteristics of substrate integrated waveguide," *IEEE Trans. Microw. Theory Techn.*, vol. 53, no. 1, pp. 66–73, Jan. 2005.

[65] Y. Dong and T. Itoh, "Miniaturized substrate integrated waveguide slot antennas based on negative order resonance," *IEEE Trans. Antennas Propag.*, vol. 58, no. 12, pp. 3856–3864, Dec. 2010.

[66] G. Q. Luo, Z. F. Hu, W. J. Li, X. H. Zhang, L. L. Sun, and J. F. Zheng, "Bandwidth-enhanced low-profile cavity-backed slot antenna by using hybrid SIW cavity modes," *IEEE Trans. Antennas Propag.*, vol. 60, no. 4, pp. 1698–1704, Apr. 2012.

[67] Y. Zhang, Z. N. Chen, X. Qing, and W. Hong, "Wideband millimeter-wave substrate integrated waveguide slotted narrow-wall fed cavity antennas," *IEEE Trans. Antennas Propag.*, vol. 59, no. 5, pp. 1488–1496, May 2011.

[68] Y. Yusuf and X. Gong, "Compact low-loss integration of high-Q 3-D filters with highly efficient antennas," *IEEE Trans. Microw. Theory Techn.*, vol. 59, no. 4, pp. 857–865, Apr. 2011.

[69] G. Q. Luo, W. Hong, Z.-C. Hao, B. Liu, W. D. Li, J. X. Chen, H. X. Zhou, and K. Wu, "Theory and experiment of novel frequency selective surface based on substrate integrated waveguide technology," *IEEE Trans. Antennas Propag.*, vol. 53, no. 12, pp. 4035–4043, Dec. 2005.

[70] W. Hong, B. Liu, Y. Wang, Q. Lai, H. Tang, X. X. Yin, Y. D. Dong, Y. Zhang, and K. Wu, "Half mode substrate integrated waveguide: A new guided wave structure for microwave and millimeter wave application," in *Proc. Joint 31st Int. Conf Infra. MillimeterWaves/14th Int. Conf. Terahertz Electron., Shanghai*, Sep. 2006, p. 219.

[71] W. Wahab, D. Busuioc, and S. Safavi-Naeini, "Low cost planar waveguide technology-based dielectric resonator antenna (DRA) for millimeter-wave applications: Analysis, design, and fabrication," *IEEE Trans. Antennas Propag.*, vol. 58, no. 8, pp. 2499–2507, Aug. 2010.

[72] W. Abdel-Wahab, D. Busuioc, and S. Safavi-Naeini, "Millimeter-wave high radiation efficiency planar waveguide series-fed dielectric resonator antenna (DRA) array: Analysis, design, and measurements," *IEEE Trans. Antennas Propag.*, vol. 59, no. 8, pp. 2834–2843, Aug. 2011.

[73] L. K. Hady, D. Kajfez, and A. A. Kishk, "Triple mode use of a single dielectric resonator," *IEEE Trans. Antennas Propag.*, vol. 57, no. 5, pp. 1328–1335, May 2009.

[74] K. M. Luk, M. T. Lee, K. W. Leung, and E. K. N. Yung, "Technique for improving coupling between microstripline and dielectric resonator antenna," *Electron. Lett.*, vol. 35, no. 5, pp. 357–358, Mar. 1999.

[75] Q. Lai, C. Fumeaux, W. Hong, and R. Vahldieck, "60 GHz aperture-coupled dielectric resonator antennas fed by a half-mode substrate integrated waveguide," *IEEE Trans. Antennas Propag.*, vol. 58, no. 6, pp. 1856–1864, Jun. 2010.

[76] P. Guillon, Y. Garault, and J. Farenc, "Dielectric resonator dual modes filter," *Electron. Lett.*, vol. 16, no. 17, pp. 646–647, 14 1980.

[77] S.-S. Oh, S.-H. Chang, D.-C. Lim, and G. C. An, "FDTD modeling of cylindrical dielectric resonator filters," in *Proceedings of the IEEE Region 10 Conference TENCON 99*, vol. 1, 1999, pp. 15–18.

[78] M. Oliver, R. Mongia, and Y. Antar, "A new broadband circularly polarized dielectric resonator antenna," in *Antennas and Propagation Society International Symposium, 1995. AP-S. Digest*, vol. 1, Jun. 1995, pp. 738–741.

[79] C. Y. Huang, J. Y. Wu, and K. L. Wong, "Cross-slot-coupled microstrip antenna and dielectric resonator antenna for circular polarization," *IEEE Trans. Antennas Propag.*, vol. 47, no. 4, pp. 605–609, 1999.

[80] G. Drossos, Z. Wu, and L. Davis, "Circular polarised cylindrical dielectric resonator antenna," *Electron. Lett.*, vol. 32, no. 4, pp. 281–283, Feb. 1996.

[81] W. C. Wong and K. W. Leung, "Circularly polarized dielectric resonator antenna excited by dual conformal strips of unequal lengths," *Microwave Opt. Technol. Lett.*, vol. 29, no. 5, pp. 348–350, 2001.

[82] K. Lu, K. W. Leung, and Y. M. Pan, "Theory and experiment of the hollow rectangular dielectric resonator antenna," *IEEE Antennas Wireless Propag. Lett.*, vol. 10, pp. 631–634, 2011.

[83] Y. Pan and K. W. Leung, "Wideband circularly polarized trapezoidal dielectric resonator antenna," *IEEE Antennas Wireless Propag. Lett.*, vol. 9, pp. 588–591, 2010.

[84] R. Chair, S. Yang, A. Kishk, K. F. Lee, and K. M. Luk, "Aperture fed wideband circularly polarized rectangular stair shaped dielectric resonator antenna," *IEEE Trans. Antennas Propag.*, vol. 54, no. 4, pp. 1350–1352, Apr. 2006.

[85] M. Sulaiman and S. Khamas, "A singly fed rectangular dielectric resonator antenna with a wideband circular polarization," *IEEE Antennas Wireless Propag. Lett.*, vol. 9, pp. 615–618, 2010.

[86] K. W. Leung, W. C. Wong, K. M. Luk, and E. K. N. Yung, "Circular-polarised dielectric resonator antenna excited by dual conformal strips," *Electron. Lett.*, vol. 36, no. 6, pp. 484–486, Mar. 2000.

[87] E. H. Lim, K. W. Leung, and X. S. Fang, "The compact circularly polarized hollow rectangular dielectric resonator antenna with an underlaid quadrature coupler," *IEEE Trans. Antennas Propag.*, vol. 59, no. 1, pp. 288–293, Jan. 2011.

[88] R. Chair, A. Kishk, and K. Lee, "Wideband simple cylindrical dielectric resonator antennas," *IEEE Microw. Wireless Compon. Lett."*, vol. 15, no. 4, pp. 241–243, Apr. 2005.

[89] B. Li, C.-X. Hao, and X.-Q. Sheng, "A dual-mode quadrature-fed wideband circularly polarized dielectric resonator antenna," *IEEE Antennas Wireless Propag. Lett.*, vol. 8, pp. 1036–1038, 2009.

[90] Y. M. Pan, K. W. Leung, and K. Lu, "Omnidirectional linearly and circularly polarized rectangular dielectric resonator antennas," *IEEE Trans. Antennas Propag.*, vol. 60, no. 2, pp. 751–759, Feb. 2012.

[91] Y. M. Pan and K. W. Leung, "Wideband omnidirectional circularly polarized dielectric resonator antenna with parasitic strips," *IEEE Trans. Antennas Propag.*, vol. 60, no. 6, pp. 2992–2997, Jun. 2012.

[92] A. Petosa, A. Ittipiboon, and M. Cuhaci, "Array of circular-polarised cross dielectric resonator antennas," *Electron. Lett.*, vol. 32, no. 19, pp. 1742–1743, Sep. 1996.

[93] A. Ludwig, "The definition of cross polarization," *IEEE Trans. Antennas Propag.*, vol. 21, no. 1, pp. 116–119, Jan. 1973.

[94] C. Balanis, *Antenna Theory: Analysis and Design*, 3rd ed. Wiley, 2005.

[95] G. Almpanis, C. Fumeaux, and R. Vahldieck, "Dual-mode bridge-shaped dielectric resonator antennas," *IEEE Antennas Wireless Propag. Lett.*, vol. 9, pp. 103–106, 2010.

[96] A. Petosa, A. Ittipiboon, and M. Cuhaci, "Array of circular-polarised cross dielectric resonator antennas," *Electron. Lett.*, vol. 32, no. 19, pp. 1742–1743, Sep. 1996.

[97] S. Yang, R. Chair, A. A. Kishk, K. F. Lee, and K. M. Luk, "Circular polarized elliptical dielectric resonator antenna sub array fed by hybrid-ring feeding network," in *2006 IEEE Int. Symp. Antennas and Propag.*, Jul. 2006, pp. 2221–2224.

[98] T. Taga, "Analysis for mean effective gain of mobile antennas in land mobile radio environments," *IEEE Trans. Veh. Technol.*, vol. 39, no. 2, pp. 117–131, May 1990.

[99] J. Volakis, *Antenna Engineering Handbook*, 4th ed. McGraw-Hill, 2007.

[100] L. Thamae and Z. Wu, "Diversity performance of multiport dielectric resonator antennas," *Microwaves, Antennas Propagation, IET*, vol. 4, no. 11, pp. 1735–1745, Nov. 2010.

[101] R. Vaughan and J. Andersen, "Antenna diversity in mobile communications," *IEEE Trans. Veh. Technol.*, vol. 36, no. 4, pp. 149–172, Nov. 1987.

[102] S. Blanch, J. Romeu, and I. Corbella, "Exact representation of antenna system diversity performance from input parameter description," *Electron. Lett.*, vol. 39, no. 9, pp. 705–707, May 2003.

[103] S.-W. Su, C.-T. Lee, and F.-S. Chang, "Printed MIMO-antenna system using neutralization-line technique for wireless USB-dongle applications," *IEEE Trans. Antennas Propag.*, vol. 60, no. 2, pp. 456–463, Feb. 2012.

[104] C. Rowell and E. Lam, "Multiple frequency band and high isolation mobile device antennas using a capacitive slot," *IEEE Trans. Antennas Propag.*, vol. 60, no. 8, pp. 3576–3582, Aug. 2012.

[105] J.-F. Li, Q.-X. Chu, and T.-G. Huang, "A compact wideband MIMO antenna with two novel bent slits," *IEEE Trans. Antennas Propag.*, vol. 60, no. 2, pp. 482–489, Feb. 2012.

[106] B. Q. Wu and K. M. Luk, "A wideband, low-profile, conical-beam antenna with horizontal polarization for indoor wireless communications," *IEEE Antennas Wireless Propag. Lett.*, vol. 8, pp. 634–636, 2009.

[107] K. Wei, Z. Zhang, Z. Feng, and M. Iskander, "Periodic leaky-wave antenna array with horizontally polarized omnidirectional pattern," *IEEE Trans. Antennas Propag.*, vol. 60, no. 7, pp. 3165–3173, Jul. 2012.

[108] A. Ando, A. Kondo, and S. Kubota, "A study of radio zone length of dual-polarized omnidirectional antennas mounted on rooftop for personal handy-phone system," *IEEE Trans. Veh. Technol.*, vol. 57, no. 1, pp. 2–10, Jan. 2008.

[109] C. C. Lin, L. C. Kuo, and H. R. Chuang, "A horizontally polarized omnidirectional printed antenna for WLAN applications," *IEEE Trans. Antennas Propag.*, vol. 54, no. 11, pp. 3551–3556, Nov. 2006.

[110] C. Jiang, X. W. Dai, and Y. C. Jiao, "A novel compact horizontally polarized omnidirectional antenna," in *2010 International Symposium on Signals Systems and Electronics*, vol. 1, Sep. 2010, pp. 1–3.

[111] H. Nakano, R. Satake, and J. Yamauchi, "Horizontally polarized, omnidirectional antenna with a single feed," in *Wireless Information Technology and Systems (ICWITS), 2010 IEEE International Conference on*, Sep. 2010, pp. 1–4.

[112] A. Borja, P. Hall, Q. Liu, and H. Iizuka, "Omnidirectional loop antenna with left-handed loading," *IEEE Antennas Wireless Propag. Lett.*, vol. 6, pp. 495–498, 2007.

[113] H. Nakano, R. Satake, and J. Yamauchi, "Realization of a horizontally polarized, low-profile, omnidirectional antenna with an EBG reflector," in *Antennas and Propagation (EuCAP), 2010 Proceedings of the Fourth European Conference on*, Apr. 2010, pp. 1–5.

[114] K. Wei, Z. Zhang, and Z. Feng, "Design of a wideband horizontally polarized omnidirectional printed loop antenna," *IEEE Antennas Wireless Propag. Lett.*, vol. 11, pp. 49–52, 2012.

[115] A. Alford, "Localizer antenna system," U.S. Patent 2 682 050, Jun. 22, 1954.

[116] N. McEwan, R. Abd-Alhameed, E. Ibrahim, P. Excell, and J. Gardiner, "A new design of horizontally polarizedand dual-polarized uniplanar conical beam antennas for HIPERLAN," *IEEE Trans. Antennas Propag.*, vol. 51, no. 2, pp. 229–237, Feb. 2003.

[117] X. Qing, Z. N. Chen, and C. K. Goh, "A horizontally polarized omnidirectional slot antenna array," in *Antennas and Propagation Society International Symposium (APSURSI), 2012 IEEE*, Jul. 2012, pp. 1 –2.

[118] K. Wei, Z. Zhang, Z. Feng, and M. Iskander, "A MNG-TL loop antenna array with horizontally polarized omnidirectional patterns," *IEEE Trans. Antennas Propag.*, vol. 60, no. 6, pp. 2702–2710, Jun. 2012.

[119] U. M. Khan and M. Milutinovic, "Dual polarized dielectric resonator antennas," Master's thesis, Chalmers University of Technology, Goteborg, Sweden, 2010.

[120] T. Iveland, "Dielectric resonator filters for application in microwave integrated circuits," *IEEE Trans. Microw. Theory Tech.*, vol. 19, no. 7, pp. 643–652, Jul. 1971.

[121] G. Junker, A. Kishk, A. Glisson, and D. Kajifez, "Effect of air gap on cylindrical dielectric resonator antenna operating in TM_{01} mode," *Electron. Lett.*, vol. 30, no. 2, pp. 97–98, Jan. 1994.

[122] X. S. Fang and K. W. Leung, "Linear-/circular-polarization designs of dual-/wide-band cylindrical dielectric resonator antennas," *IEEE Trans. Antennas Propag.*, vol. 60, no. 6, pp. 2662–2671, Jun. 2012.

[123] N. Kuga, H. Arai, and N. Goto, "A notch-wire composite antenna for polarization diversity reception," *IEEE Trans. Antennas Propag.*, vol. 46, no. 6, pp. 902–906, jun 1998.

[124] E. Soliman, M. Ibrahim, and A. Abdelmageed, "Dual-polarized omnidirectional planar slot antenna for WLAN applications," *IEEE Trans. Antennas Propag.*, vol. 53, no. 9, pp. 3093–3097, Sep. 2005.

[125] C. Deng, P. Li, and W. Cao, "A high-isolation dual-polarization patch antenna with omnidirectional radiation patterns," *IEEE Antennas Wireless Propag. Lett.*, vol. 11, pp. 1273–1276, 2012.

[126] K.-C. Huang and Z. Wang, *Millimeter Wave Communication Systems*. Wiley-IEEE Press, 2011.

[127] F. Yang, P. Nayeri, A. Elsherbeni, J. Ginn, D. Shelton, G. Boreman, and Y. Rahmat-Samii, "Reflectarray design at infrared frequencies: Effects and models of material loss," *IEEE Trans. Antennas Propag.*, vol. 60, no. 9, pp. 4202–4209, Sep. 2012.

[128] A. Perron, T. Denidni, and A. Sebak, "Circularly polarized microstrip/elliptical dielectric ring resonator antenna for millimeter-wave applications," *IEEE Antennas Wireless Propag. Lett.*, vol. 9, pp. 783–786, 2010.

[129] A. Perron, T. Denidni, and A.-R. Sebak, "High-gain hybrid dielectric resonator antenna for millimeter-wave applications: Design and implementation," *IEEE Trans. Antennas Propag.*, vol. 57, no. 10, pp. 2882–2892, Oct. 2009.

[130] Y.-M. Pan, K. W. Leung, and K. M. Luk, "Design of the millimeter-wave rectangular dielectric resonator antenna using a higher-order mode," *IEEE Trans. Antennas Propag.*, vol. 59, no. 8, pp. 2780–2788, Aug. 2011.

[131] D. S. Filonov, A. E. Krasnok, A. P. Slobozhanyuk, P. V. Kapitanova, E. A. Nenasheva, Y. S. Kivshar, and P. A. Belov, "Experimental verification of the concept of all-dielectric nanoantennas," *Applied Physics Letters*, vol. 100, no. 20, p. 201113, 2012.

[132] A. E. Krasnok, A. E. Miroshnichenko, P. A. Belov, and Y. S. Kivshar, "All-dielectric optical nanoantennas," *Opt. Express*, vol. 20, no. 18, pp. 20 599–20 604, Aug. 2012.

[133] S. A. Maier, *Plasmonics: Fundamentals and Applications*. Springer Verlag, 2007.

[134] S. Lucyszyn, "Evaluating surface impedance models for Terahertz frequencies at room temperature," *Piers Online*, vol. 3, no. 4, pp. 554–559, 2007.

[135] M. P. Marder, *Condensed Matter Physics*. JohnWiley & Sons, Inc., New York, NY, 2000.

[136] D. T. Owens, C. Fuentes-Hernandez, J. M. Hales, J. W. Perry, and B. Kippelen, "A comprehensive analysis of the contributions to the nonlinear optical properties of thin Ag films," *Journal of Applied Physics*, vol. 107, no. 12, 2010.

[137] E. D. Palik, *Handbook of Optical Constants of Solids*. Academic Press, 1985.

[138] P. Bharadwaj, B. Deutsch, and L. Novotny, "Optical antennas," *Adv. Opt. Photon.*, vol. 1, no. 3, pp. 438–483, Nov. 2009.

[139] L. Novotny and N. van Hulst, "Antennas for light," *Nat. Photon.*, vol. 5, no. 2, pp. 83–90, Feb. 2011.

[140] L. Novotny, "Effective wavelength scaling for optical antennas," *Phys. Rev. Lett.*, vol. 98, no. 26, pp. 266 802–266 805, Jun. 2007.

[141] J. Aizpurua, G. W. Bryant, L. J. Richter, F. J. García de Abajo, B. K. Kelley, and T. Mallouk, "Optical properties of coupled metallic nanorods for field-enhanced spectroscopy," *Phys. Rev. B*, vol. 71, no. 23, Jun. 2005.

[142] T. H. Taminiau, R. J. Moerland, F. B. Segerink, L. Kuipers, and N. F. van Hulst, "$\lambda/4$ resonance of an optical monopole antenna probed by single molecule fluorescence," *Nano Lett.*, vol. 7, no. 1, pp. 28–33, 2007.

[143] T. H. Taminiau, F. D. Stefani, and N. F. van Hulst, "Enhanced directional excitation and emission of single emitters by a nano-optical Yagi-Uda antenna," *Opt. Express*, vol. 16, no. 14, pp. 10 858–10 866, Jul. 2008.

[144] J. Li, A. Salandrino, and N. Engheta, "Shaping light beams in the nanometer scale: A Yagi-Uda nanoantenna in the optical domain," *Phys. Rev. B*, vol. 76, no. 24, p. 245403, Dec. 2007.

[145] C. Fumeaux, G. D. Boreman, W. Herrmann, H. Rothuizen, and F. K. Kneubühl, "Polarization response of asymmetric-spiral infrared antennas," *Appl. Opt.*, vol. 36, no. 25, pp. 6485–6490, Sep. 1997.

[146] R. Esteban, T. V. Teperik, and J. J. Greffet, "Optical patch antennas for single photon emission using surface plasmon resonances," *Phys. Rev. Lett.*, vol. 104, no. 2, p. 26802, Jan. 2010.

[147] P. J. Schuck, D. P. Fromm, A. Sundaramurthy, G. S. Kino, and W. E. Moerner, "Improving the mismatch between light and nanoscale objects with gold bowtie nanoantennas," *Phys. Rev. Lett.*, vol. 94, no. 1, p. 17402, Jan. 2005.

[148] J. Huang and J. Encinar, *Refelctarray Antennas*. Wiley-IEEE Press, 2007.

[149] J. Ginn, B. Lail, J. Alda, and G. Boreman, "Planar infrared binary phase reflectarray," *Opt. Lett.*, vol. 33, no. 8, pp. 779–781, Apr. 2008.

[150] D. Dregely, R. Taubert, J. Dorfmller, R. Vogelgesang, K. Kern, and H. Giessen, "3D optical Yagi-Uda nanoantenna array," *Nat. Communications*, vol. 2, no. 267, pp. 1–7, 2011.

[151] N. Yu, P. Genevet, M. A. Kats, F. Aieta, J.-P. Tetienne, F. Capasso, and Z. Gaburro, "Light propagation with phase discontinuities: Generalized laws of reflection and refraction," *Science*, vol. 334, no. 6054, pp. 333–337, 2011.

[152] X. Ni, N. K. Emani, A. V. Kildishev, A. Boltasseva, and V. M. Shalaev, "Broadband light bending with plasmonic nanoantennas," *Science*, vol. 335, no. 6067, p. 427, Jan. 2012.

[153] M. Keller, J. Shaker, A. Petosa, A. Ittipiboon, M. Cuhaci, and Y. Antar, "A Ka-band dielectric resonator antenna reflectarray," in *30th European Microwave Conference*, Oct. 2000, pp. 1–4.

[154] S. Zainud-Deen, S. Gaber, A. Abd-Elhady, K. Awadalla, and A. Kishk, "Wideband perforated rectangular dielectric resonator antenna reflectarray," in *2011 IEEE International Symposium on Antennas and Propagation (APSURSI)*, Jul. 2011, pp. 113–116.

[155] M. G. N. Alsath, M. Kanagasabai, and S. Arunkumar, "Dual-band dielectric resonator reflectarray for C/X-bands," *IEEE Antennas Wireless Propag. Lett.*, vol. 11, pp. 1253–1256, 2012.

[156] M. Jamaluddin, R. Gillard, R. Sauleau, P. Dumon, and L. Le Coq, "Reflectarray element based on strip-loaded dielectric resonator antenna," *Electron. Lett.*, vol. 44, no. 11, pp. 664–665, May 2008.

[157] A. Abd-Elhady, S. Zainud-Deen, A. Mitkees, and A. Kishk, "X-band linear polarized aperture-coupled DRA reflectarray," in *2010 International Conference on Microwave and Millimeter Wave Technology (ICMMT)*, May 2010, pp. 1042–1044.

[158] S. Zainud-Deen, A. Abd-Elhady, A. Mitkees, and A. Kishk, "Dielectric resonator reflectarray with two DRA sizes and varying slot loading," in *2010 IEEE Antennas and Propagation Society International Symposium (APSURSI)*, Jul. 2010, pp. 1–4.

[159] A. Alù and N. Engheta, "Hertzian plasmonic nanodimer as an efficient optical nanoantenna," *Physical Review B*, vol. 78, no. 19, p. 195111, Nov. 2008.